T.C
İNÖNÜ UNIVERSITY
GRADUATE SCHOOL OF NATURAL AND APPLIED SCIENCE

Characterization of Electrodes Used in Rechargeable Batteries by Synchrotron Radiation.

Erdinç Öz

Ph.D. THESIS

PHYSICS DEPARTMENT

JULY 2019

T.C
İNÖNÜ ÜNİVERSİTESİ
FEN BİLİMLERİ ENSTİTÜSÜ

Şarjedilebilir Pillerde Kullanılan Elektrotların Synchrotron Radyasyonu ile Karakterize Edilmesi

Erdinç Öz

DOKTORA TEZİ

FİZİK BÖLÜMÜ

TEMMUZ 2019

Tezin Başlığı: Şarjedilebilir Pillerde Kullanilan Elektrotların Synchrotron Radyasyonu İle Karakterize Edilmesi

Tezi Hazırlayan: Erdinç Öz

Sınav Tarihi: 01.07.2019

Yukarıda adı geçen tez jürimizce değerlendirilerek Fizik Ana Bilim Dalında Doktora Tezi olarak kabul edilmiştir.

Sınav Jüri Üyeleri:

Tez Danışmanı: **Prof. Dr. Serdar ALTIN** .....
İnönü Üniversitesi

Eş Danışman: **Doç. Dr. Sevda AVCI** .....
İstanbul Medeniyet Üniversitesi

Prof. Dr. H. İbrahim ADIGÜZEL .....
İnönü Üniversitesi

Prof. Dr. Ali BAYRİ .....
İnönü Üniversitesi

Prof. Dr. Ertan EVİN .....
Fırat Üniversitesi

Doç. Dr. Ömer GÜLER .....
Mersin Üniversitesi

Prof. Dr. H. İbrahim ADIGÜZEL
Enstitü Müdürü

ONUR SÖZÜ

Doktora Tezi olarak sunduğum "Şarjedilebilir Pillerde Kullanılan elektrotların Synchrotron Radyasyonu ile Karakterize Edilmesi" başlıklı bu çalışmanın bilimsel ahlak ve geleneklere aykırı düşecek bir yardıma başvurmaksızın tarafımdan yazıldığını ve yararlandığım bütün kaynakların, hem metin içinde hem de kaynakçada yöntemine uygun biçimde gösterilenlerden oluştuğunu belirtir, bunu onurumla doğrularım.

Erdinç ÖZ

ÖZET

Doktora Tezi

ŞARJEDİLEBİLİR PİLLERDE KULLANILAN ELEKTROTLARIN SYNCHROTRON RADYASYONU İLE KARAKTERİZE EDİLMESİ

Erdinç Öz

İnönü Üniversitesi
Fen Bilimleri Enstitüsü
Fizik Anabilim Dalı

114+ xii sayfa

2019

Danışman: Prof. Dr. Serdar ALTIN

İkinci Danışman : Doç. Dr. Sevda AVCI

Bu doktora tezinde, Mn bölgelerine Co ve Ni katkılamasının $Na_{0.44}MnO_2$ nanorodunun elektrokimyasal performansına etkisi araştırıldı.

Son yıllarda, nanomalzemeler sodium-iyon pil teknolojisinde öne çıkmıştır ve sodium-iyon pillerin ticarileştirilmesinde önemli bir rol almaktadır. $Na_{0.44}MnO_2$ kısa difüzyon mesafesi ve geniş reaksiyon alanı gibi benzersiz avantajlar sağlayan tünel tipi nanorod yapısına sahiptir. Diğer taraftan bu kompleks yapının avantajları olduğu kadar dezavantajları da mevcuttur: uzun döngülerde ortaya çıkan yapısal stress ve Mn bölgelerinde Jahn-Teller etkisi ile ortaya çıkan kristal yapı deformasyonu. Bu çalışmada, $Na_{0.44}MnO_2$ nanorod içerisindeki Mn bölgelerine Co ve Ni ikamesi yapılarak yapısal deformasyonun engellenmesi ve pil performansının arttırılması hedeflenmiştir. Araştırma sırasında fiziksel ve elektrokimyasal analizler detaylı şekilde yapılmıştır, özellikle kristal yapıdaki değişimleri detaylı şekilde incelemek için synchrotron radyasyonunun benzersiz özelliklerinden faydanalınılmıştır.

Çalışmada yürütülen analizler sonucunda, $Na_{0.44}MnO_2$ bileşiğinde Mn bölgelerine %0.1 ve %0.5 Ni ve %0.1 Co ikame edilen örneklerinin $Na_{0.44}MnO_2$ bileşiğine göre daha yüksek kapasite tutma oranına sahip olduğu belirlenmiştir.

ANAHTAR KELİMELER: Sodyum-iyon pil, nanorod, pil performansı, synchrotron ışınımı.

ABSTRACT

Ph.D. Thesis

CHARACTERIZATION OF ELECTRODES USED IN RECHARGEABLE BATTERIES WITH SYNCHROTRON RADIATION

Erdinç Öz

İnönü University
Graduate School of Natural and Applied Science
Department of Physics

114+ xii pages

2019

Supervisor: Prof. Dr. Serdar ALTIN

Co-supervisor: Assoc. Prof. Dr. Sevda AVCI

In this Ph.D. thesis, the effects of Co and Ni substitution on Mn sites on the electrochemical performance of $Na_{0.44}MnO_2$ nanorod were investigated.

In recent years, nanomaterials have been at the forefront of rechargeable sodium-ion battery technology and currently have a significant role in the commercialization of Na-ion batteries. The $Na_{0.44}MnO_2$ has a tunnel type nanorod structure which provides unique advantages such as short diffusion distance and large reaction surfaces. On the other hand, there are disadvantages besides the advantages of this crystal structure: crystal structure degradation due to structural stress and Jahn-Teller effect on Mn sites in long charge/discharge cycles. In this study, it is aimed to prevent structural degradation and increase battery performance by making Co and Ni substitution to the Mn regions of $Na_{0.44}MnO_2$ nanorods. During the research, physical and electrochemical analysis of all samples were carried out in detail. Especially, unique advantages of synchrotron radiation have been used to better understand the changes in the crystal structures.

As a result of this study, it was found that the 0.1% and 0.5% nickel and 0.1% cobalt substituted samples had nanorod form and higher capacity retention than $Na_{0.44}MnO_2$.

KEYWORDS: Na-ion battery, nanorod, battery performance, synchrotron radiation.

ACKNOWLEDGEMENT

This study supported by Inonu University Scientific Research Project Unit (IUBAP) project no: FDK-2017/678, Ankara University Institute of Accelerator Technologies TARLA project (2006K-12047), Deutsches Elektronen-Synchrotron (DESY) research institute and NFFA.EU project (project ID-568).

I first would like to thank my supervisor Prof. Serdar Altın for providing me his invaluable guidance, his patience, knowledge and expertise during my dissertation. His guidance helped me in all the time of research and writing of this thesis. I hope to continue our collaboration in the future.

I would like to thank my co-supervisor Assoc. Prof. Sevda Avcı for providing me unique support and guidance during my dissertation.

Beside my supervisors, I would like to thank the rest of my thesis committee: Prof. Ali Bayri, Prof. H. İbrahim Adıgüzel, Prof. Ertan Evin, Assoc. Prof. Ömer Güler for their insightful comments and encouragement.

I would like to thank Dr. Hasan Yavaş and Assoc. Prof. Avni Aksoy, who provide me to study at DESY research institute and supported me throughout my dissertation. My sincere thanks also goes to Dr. Hans-Christian Wille, Frank-Uwe Dill, Conrad Hagemeister, Simon Mayer, Dr. Hlynur Gretarsson and all other P01 staff who provided me an opportunity to join their team as a staff. I would also like to thank Dr. Wolfgang Caliebe, Dr. Edmund Welter and Dr. Vadim Murzin for supporting me in performing XAFS experiments at P64 and P65 beamlines. I would like to thank Dr. Michael Wharmby, Dr. Jo-Chi Tseng, Dr. Martin Etter, Mario Wendt and all other P02.1 beamline staff for their patience and providing me with valuable information about synchrotron x-ray diffraction and the opportunity to perform my experiments. Additionally, I would like to thank Milena Lippman and Anca Ciobanu for helping me with technical matters during my work at DESY.

Last but not the least, I would to thank my very precious parents, Beser Öz and Hasan Öz, and my brothers for the invaluable support they gave me throughout my life.

Erdinç ÖZ

OUTLINE

FIGURES LIST

TABLE LIST

SYMBOLS AND ABBREVIATIONS

$\mathbf{Q_T}$	Theoretical Capacity
$\mathbf{Q_P}$	Practical Capacity
A	Area
t	Time
$\boldsymbol{i}$	Current density
CE	Coulombic Efficiency
$\Delta \boldsymbol{G_r^0}$	Gibbs Free Energy
$\mathbf{E_{cell}}$	Electrochemical cell voltage
$\boldsymbol{\mu_B}$	Bohr Magnetron
$\boldsymbol{\mu_{eff}}$	Effective Magnetic Moment
T	Temperature
LIBs	Lithium-ion Batteries
SIBs	Sodium-ion Batteries
F	Faraday Constant
M	Molecular Weight

1. **INTRODUCTION**

The demand for energy has increased since the beginning of industrialization. From the 1850s to 2000s, the period that marks the beginning of the industrial revolution, the energy consumption of the world increased by 20 times [1]. This immense increase in consumption is not solely related to the amount of energy required for production but is also a result of the energy demands of the human population increasing along with technological developments such as transportation, communication, etc. This increase in energy demand has led people to seek alternative energy sources over the past decades. Fossil fuels (particularly coal and petroleum products), which can meet the majority of energy production needs, have recently been found to fulfill this requirement. However, researchers have recently stated that a consensus has been reached on two issues related to fossil fuels. First, the source of fossil fuels is decreasing at such a dramatic rate that it will soon turn unable to meet the energy demand. Second, and more importantly, fossil fuels are not as clean as they are considered to be; CO_2 emissions resulting from the consumption of fossil fuels cause global warming by creating a greenhouse effect. The average temperature of the earth increased by 0.6°C in the past century, and some estimations show that this average temperature will further increase by 1.8°C in the next century [2]. Accordingly, it can be concluded that the increase in temperature will have many negative effects. One of these effects is the rise of sea levels, and this rise might threaten major cities such as New York, London, Mumbai and many small coastal cities. Such immense impact has brought about the need for a rapid search for alternative energy sources and provided significant amounts of research on energy sources such as solar and wind energy that are completely clean, renewable and sustainable.

The major problems that emerge in the use of resources, whether it is a fossil or a renewable energy source, are the storing and efficient use of the energy obtained from these sources. Researchers recommend the use of a new generation of rechargeable lithium-ion batteries (LIBs) and sodium-ion batteries (SIBs) as an alternative to this problem. LIBs and SIBs show high efficiency in the storage and reuse of energy. On the other hand, rechargeable batteries are already in use as efficient energy sources for many electronic devices, such as mobile phones, notebooks and cameras. Moreover,

using these batteries as a source of energy for plug-in hybrid electric vehicles (PHEVs) and electric vehicles (EVs) is an additional motivation for researchers. Many studies have been carried out on battery efficiency with the development of cathode and anode materials. In these studies, different element substitution [3,4], surface coatings [5,6] and different production techniques [7,8] were applied to the electrodes and their efficiency was also investigated.

Characterization techniques play a significant role in all production research. These techniques determine whether a synthesized sample is in the desired form and how its structure changes after any process. The synchrotron x-ray technique, one of the spectroscopic characterization techniques, is significantly more advantageous compared to other spectroscopic techniques (UV, IR, XRD, etc.) with its wide energy range, more brilliant radiation, and element-specific operation. These facilities are, moreover, rare and their limited usage time makes the technique more valuable.

It is obvious that fossil fuels will continue to be used in the following years. However, studies on renewable energy sources and the storage of this energy will be the key to how people will live in a clean and livable environment in the future.

This PhD Study aims to synthesis new cathode materials for use in new generation energy storage systems and rechargeable batteries for environmentally friendly, economical and long-life SIBs, and to characterize their structures with unique synchrotron radiation techniques.

In the Introduction section, the short history of the rechargeable batteries, the operating mechanism of Na-ion batteries, the basic components and the basic terms related to the batteries are defined. Subsequently, in the last part of the section, information is given about the cathode materials used in Na-ion batteries according to their structure. In the Methodology section, detailed information is given about the production of the materials which are the subject of thesis and the physical and electrochemical characterization techniques used. In the Result and Discussion section, the results of the characterization analyze were informed and the physical and electrochemical meanings of the results were discussed. In the Conclusion section, it is discussed whether the results are compatible with the hypothesis of the thesis. In addition, the data obtained from the analyzes were compared with the literature, and recommendations were made for future studies.

1.1. Short History of Rechargeable Batteries

In 1799 Alessandro Volta produced the first modern battery by using lead sheets, cardboard and silver soaked in salt-water [9]. Although this is not the first battery to generate electricity, it is the first battery to produce stable electricity. Unfortunately, due to the rapid corrosion of metals, the electricity production time was significantly short. This design was named as "Volta battery," and the potential difference unit was named as "Volt" in honor of Alessandro Volta. The English chemist John Frederic Daniell improved the Volta battery in 1836. He placed a copper plate on the bottom of a glass jar and filled half of it with copper sulfate solution. Subsequently, he placed a zinc plate on top of the open glass jar and filled the remainder of the jar with a zinc sulfate solution. Due to density difference between zinc sulfate and copper sulfate, they do not mix. The zinc plate was used as the negative side (anode) and the copper plate was used as the positive side (cathode) in this battery. In the years following its invention, the Daniell battery was ideal for fixed devices (such as phones). In 1866, French engineer Georges Leclanché invented the Leclanché battery, which became a pioneer of modern zinc-carbon batteries [10]. The Leclanché battery consists of a zinc anode and a manganese oxide cathode that is wrapped in a porous material and mixed with some carbon to increase conductivity. This system is placed in a jar filled with ammonium chloride solution. Approximately 1.4 volts of voltage can be generated from this battery. Chemical reactions start with the oxidation of the zinc anode surface. Zn ions and free electrons formed in the reaction, and thus the anode is more negatively charged than the cathode. Free electrons move through the anode through an external circuit and generate current. When the electrons reach the cathode, they react with manganese dioxide and water to form manganese oxide and negatively charged hydroxide ions. In the secondary acid-base reaction, negatively charged hydroxyl (OH^-) ions accept a hydrogen (a proton) particle from ammonium chloride to form water (H_2O), and thus the ammonium chloride is transformed to ammonia.

Gaston Plante introduced the first rechargeable battery in 1859 with the discovery of lead-acid batteries [11]. The battery was formed by separating the two-layer pure lead spiral roll with a linen cloth and immersing it in a glass jar of sulfuric acid solution. The main starting point of the batteries used in cars today is based on the battery developed by Plante. In 1899, the Swedish engineer Waldemar Jungner invented

rechargeable nickel cadmium batteries [12]. This battery contains nickel (III) oxide-hydroxide (NiOOH) positive electrode, cadmium (Cd) negative electrode, potassium hydroxide electrolyte and a separator. Due to their low internal resistance, they can produce high current and rapidly recharge. Despite these positive characteristics, it has a very significant disadvantage; memory effect. When these batteries are quickly discharged to approximately 20% of capacity and re-charged again, and if this is regularly repeated, the battery remembers this limit and partly loses its capacity. Although these batteries were quickly replaced by primary batteries since they are commercially available, in the 1990s, they quickly lost popularity with the discovery of NiMH and Li-ion batteries.

NiMH batteries use NiOOH cathodes in a manner similar to NiCd batteries. However, these batteries use AB_5 or AB_2 form alloys instead of cadmium as an anode. Where A is titanium, vanadium (in AB_2 form) or lanthanum, cerium, neodymium, praseodymium (in AB_5 form), B is zirconium, nickel (in AB_2 form) or manganese, aluminum, cobalt (in AB_5 form) [13]. NiMH batteries have been used as high-power sources in hybrid commercial vehicles such as the Toyota Prius. However, rechargeable batteries produced in AA size are used in many portable electronic devices, due to their long cycle life and high-current-drain features. Although NiMH batteries are quite popular for use in portable devices because of their high energy density and safety, they have low voltage output (1.2 V for AA type battery) compared to Li-ion batteries (3.7 V for coin type battery) and high self-discharge rate.

The development of rechargeable Li-ion batteries in 1980 by American physicist J. B. Goodenough served a turning point in the field [14]. The working principle of Li-ion batteries is similar to NiMH batteries, but they have unique advantages. First, Li is the lightest and most electronegative element (3.04 V) in the periodic table. These features provide the advantage of a much higher voltage to Li-ion batteries and also make them lighter and more portable. Second, Li-ion batteries are suitable for long-term use because of no memory effect.

Lithium-ion batteries are widely used in various industrial applications including electrical appliances, telecommunications, healthcare, energy storage systems, automobiles and consumer electronics products. Growing demand for consumer electronics and renewable energy use has caused a boost in the lithium-ion battery market. For example, the batteries of almost all mobile phones used today are Li-ion

or Li-polymer batteries. Furthermore, these batteries also attract the attention of electric car manufacturers, such as Toyota that uses Li-ion batteries in its vehicles and provides funding for research into the development of these batteries [15,16].

1.2. General Concepts of Rechargeable Batteries

1.2.1. Working Principle

Rechargeable batteries function on a system that converts chemical energy (redox reaction) into electrical energy. The primary idea is the use of the energy from redox energy as a result of the insertion/extraction of positive ions into/from an electrode (cathode or anode) during the charge/discharge process. During the charging process, the oxidation reaction occurs on the cathode surface and positive ions flow from the cathode to the anode through the electrolyte. Furthermore, the electrons flow from the cathode to the anode through the external circuit and vice versa at discharge (Figure 1).

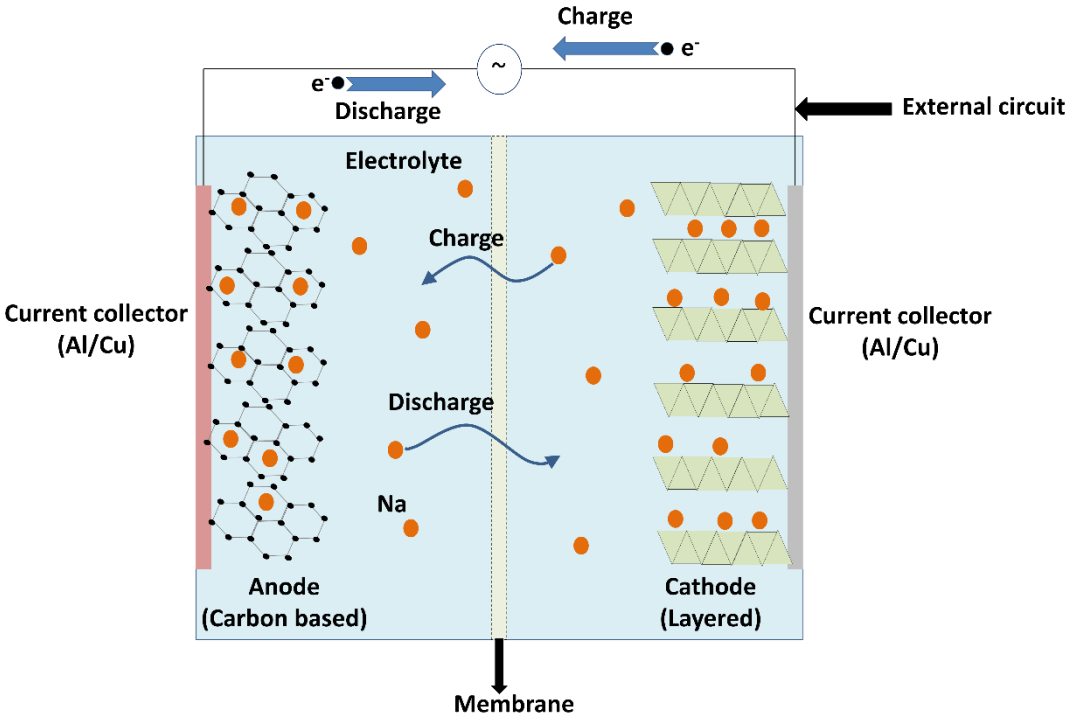

Figure 1. A schematic of the rechargeable Na-ion battery components and working process.

1.2.2. Basic Components

A typical rechargeable battery consists of electrodes, electrolyte and a separator (Figure 1). While the anode is selected from carbon-based materials, the cathode is formed by the mixing of an active material (synthesized compound), a conductive material (to increase the electrical conductivity) and a binder (for binding the entire mixture to the current collector surface).

The electrolyte is used in transferring the ions between the electrodes for the functioning of the battery and usually consists of an organic salt ($NaPF_4$, $LiPF_4$, $NaClO_4$, etc.) and a mixture of solvents (EC, PC, DMC, etc.). Chemical stability and good interfacial contact between the electrolyte and the electrodes are fundamental requirements for an efficient ion transfer. Although electrolyte research has focused on these two basic features, other features that the electrolyte must have are—low electronic conductivity to prevent short cuts, high ionic conductivity to ensure efficient ionic transfer, being chemically inert to the electrodes, membrane and other components, high wettability of electrode surface and environmental friendliness. Some research shows that these properties may be kept at the optimum level with the change in the molarity of the salts or a change in the ratio of solvents in the electrolyte [17–19].

The electrolyte-wetted membrane placed between the anode and cathode prevents the short-circuiting of electrodes by physically contacting each other. Chemically inert and electrochemically stable membranes have a porous structure that prevents the passage of electrons while allowing ions to pass through between the anode and cathode. Wettability, another important feature, helps to carry out the ionic conductivity in the battery efficiently and to reduce the internal resistance [20].

The movement of the electrons between the cathode and anode is carried out by an external connection (Figure 1). As a current collector, the SIBs use the Al for both positive and negative electrodes. On the other hand, since Li reacts with Al at low potentials and forms an impurity alloy, LIBs use Cu at the anode electrodes. This situation, as expected, gives SIBs a cost and lightness advantage.

1.2.3. Nomenclature

Electrochemical energy storage systems are available in a wide variety that can be used in different areas. Rechargeable batteries have an important part of this variety, while the definitions of the term may differ from other energy storage systems. Some of the key terms that will be used frequently in the following sections of this study are explained next to avoid confusion.

1.2.3.1. Capacity and Specific Capacity

The capacity of a battery is defined as the amount of charge that the battery can store in it, and this is usually determined by the amount of active material the battery has (typically in Ah). However, this is not sufficient to define the capacity alone because other factors that affect the capacity (such as the charge/discharge zone and temperature) should be considered when defining this. However, in order to make a comparison between the capacities of the materials, it is more useful to use the specific capacity obtained by dividing the capacity by the mass of the active material.
Specific capacity is the normalized amount of total capacity in the positive or negative electrode over the mass of the electrochemically active material and is measured in mAh/g. This value can be calculated in two different ways; theoretically and practically. Theoretically, the specific capacity of a compound can be calculated with the following formula:

$$Q_T = \frac{n*F}{3600*M} * 1000\ (mAh/g) \qquad (1)$$

where n is the number of charge carrier, F is the Faraday constant, and M is the molecular weight of the active material.
Practically we can calculate the specific capacity of a compound as follows: first, the compound must be subjected to galvanostatic cycle testing. Subsequently, the data obtained from the voltage-time graph as a result of this test is used in the following formula:

$$Q_P = \frac{i*A*t_c}{3600*M} * 1000\ (mAh/g) \qquad (2)$$

where i is the current density, A is the area of the electrode, t_c, is the time to reach to cut off voltage in seconds, and M is the molecular weight of the active material.

In reality, the Q_P is lower than the Q_T. Although there are multiple reasons for this, the most important reason is the inaccessible ion mobility in the compound because the cut off voltage value is not enough to remove the charge carriers remaining in the compound. Some other reasons are, undesirable side reactions (for example reactions between electrolyte and electrodes) in the battery cell and the formation of various side products on the electrode surface, etc.

Another term related to capacity is C-rate. C-rate is defined as the current that an electrode has to charge or discharge until reaching the theoretical specific capacity value in a specific amount of time. The *n*C rate indicates a charge or discharge rate corresponding to a sufficiently high current to charge/discharge the entire mass of the active material in the electrode within *n* hours. For example, for a 1 Ah battery, the 1C rate corresponds to fully charge/discharged with 1 A current in one hour, while 0.5C rate corresponds to fully charged/discharged with 0.5A current in two hours for the same battery.

In practice, when measuring the capacities of the batteries, some loss of capacity can be observed caused by parasitic reactions occurring between the electrolyte and electrodes or by surface distortions occurring on the electrodes in each charge/discharge cycle. These capacity losses are related to the reversibility properties of the electrode materials and we can define the reversibility rate with the term "columbic efficiency*"* (CE):

$$CE = \frac{Q_d}{Q_c} * 100 \qquad (3)$$

where Q_d is discharge capacity, and Q_c is charge capacity. For example, a 100% CE value indicates that all charge carriers can make fully reversible reactions on the cathode and anode, and there is not any capacity fade during charge/discharge. A battery under these conditions is called an ideal battery. In experimental works, CE is also useful for comparing the efficiency of different electrode materials in practice.

1.2.3.2. Voltage

The voltage of an electrochemical cell is defined as the potential difference between the positive and negative electrodes of the battery. The potentials of the positive and negative electrodes are due to the chemical potential, i.e., the tendency of these electrodes to lose electrons. When two systems with different chemical potentials (in this case these systems are positive and negative electrodes) are combined, electron and charged particle transferring occurs due to the chemical potential differences between the two systems. The driving force for this reaction between the two systems is the Gibbs free energy (ΔG_r^0), and is expressed as below:

$$\Delta G_r^0 = \sum \Delta G_f^0\,(product) - \sum \Delta G_f^0\,(reactant) \qquad (4)$$

After the reaction has started in the cell, an electrical force is generated by the charged particles in the opposite direction to the Gibbs driving force. After a while, these two forces are balanced, and the electron and ion transfer in the cell will stop (open circuit conditions [OCV]). This balancing condition can be expressed as follows:

$$\Delta G_r^0 = -zFE_{cell} \qquad (5)$$

where z is the charge number, F is the Faraday constant, E_{cell} is the voltage of the electrochemical cell (the difference between the positive and negative electrodes). At this point, it can easily be assumed that positive and negative materials also have an important role: for a high voltage battery, the anode material selected should be of the lowest voltage possible. The reason for requesting a high-voltage battery is that the voltage value is proportional to the energy value of the battery. One particular feature to be considered when selecting batteries for use in applications is their specific energies (measured in Wh/kg), and its can be calculated as follows:

$$spesific\ energy = (\int E_{cell} dq)/m \qquad (6)$$

The energy ranges of the batteries according to their voltage values are as follows: 0.5–1.5 V is low quality, 1.5–3.5 V is medium quality, and 3.5–5.5 V is high quality

energy [21]. The use of batteries with high quality energy, especially in hybrid and fully electric vehicles, provides the desired energy with the use of a considerably a smaller number of batteries.

1.3. Sodium-Ion Batteries (SIBs)

The commercialization of rechargeable batteries began in the 1990's when Goodenough et al. developed Li-ion batteries. Li-ion batteries have since dominated several fields, from portable electronic devices to electric cars.

In Li-ion batteries, materials with layered structure are used as cathodes, and carbon-based materials are preferred as anodes. As the current collector, Al is preferred for the cathode, while Cu is preferred as the anode (under low potential, Li and Al transform to ternary alloy). The toxic elements (such as Co) are used in the cathode and a copper current collector is used for the anode (it is more expensive than aluminum), Li is the lightest alkaline metal (6.94 g/mol) and has the lowest redox potential (-3.04 V, against standard hydrogen electrode). These are compelling reasons to use Li-ion batteries in portable devices. However, these batteries are not cost effective. There are several reasons:

- The extreme conditions (natural and political) in the regions where Li reserves are located increase its cost of mining and transfer [22].
- Li occurs in nature as a mixture of mineral and salt-water. During the separation of the minerals and salts, many by products (such as magnesium, phosphate and sodium) are also obtained [23].
- Cobalt, widely used in Li-ion battery cathodes, contributes significantly to the stability of the crystal structure and efficient energy storage. On the other hand, it negatively impacts the cost of Li-ion battery production due to its toxicity, high cost and limited resources [24].

The above-mentioned disadvantages defend the need for an element that can function as an effective alternative to lithium; sodium. Although LIBs and SIBs were developed in the 1970s and 1980s [14,25], the rapid commercialization of LIBs and the technical problems related to the production of sodium batteries (such as material quality and glove box problems) led to postponing sodium battery research [26,27]. In

the 1990s, however, research on LIBs and SIBs progressed in parallel [28]. Since the capacity of the batteries is related to the chemical capacity and operating potential of the positive and negative electrodes, there is no major obstacle to a competition between SIBs and LIBs.

The components of LIBs and SIBs and the energy production mechanism are in essence the same. Thus, this provides an opportunity to use the basic materials used in lithium batteries in sodium batteries. Additionally, sodium has unique advantages of its own; it has the lowest redox potential after lithium (-2.7 V) and minerals and salts of sodium (such as Na_2CO_3, NaCl) can be obtained in high amounts (sodium is the fourth most abundant element on earth) [29]. Therefore, the use of Al instead of Cu (Al and Cu do not react with sodium at low potential) for sodium anodes reduce the weight and, by extension the cost of sodium batteries. On the other hand, sodium has disadvantages too; the mass of sodium (23 g / mole) is much heavier than that of lithium and this causes a lower theoretical capacity [29]. Additionally, different carbon types (such as hard carbon, graphite etc.) used in lithium batteries as anodes do not have similar capacity values in sodium batteries [30,31]. Thus, the anode materials in sodium batteries should be developed in a way to support carbon-based materials.

Considering the above-mentioned statements, it can be argued that sodium batteries are an alternative to lithium batteries. Nevertheless, several improvements must be made in order to observe an increase in the electrochemical performance of electrode materials. The meet these requirements, many studies have been undertaken in recent years to develop electrode and electrolyte materials to be used in sodium batteries (Figure 2) [17,32,33].

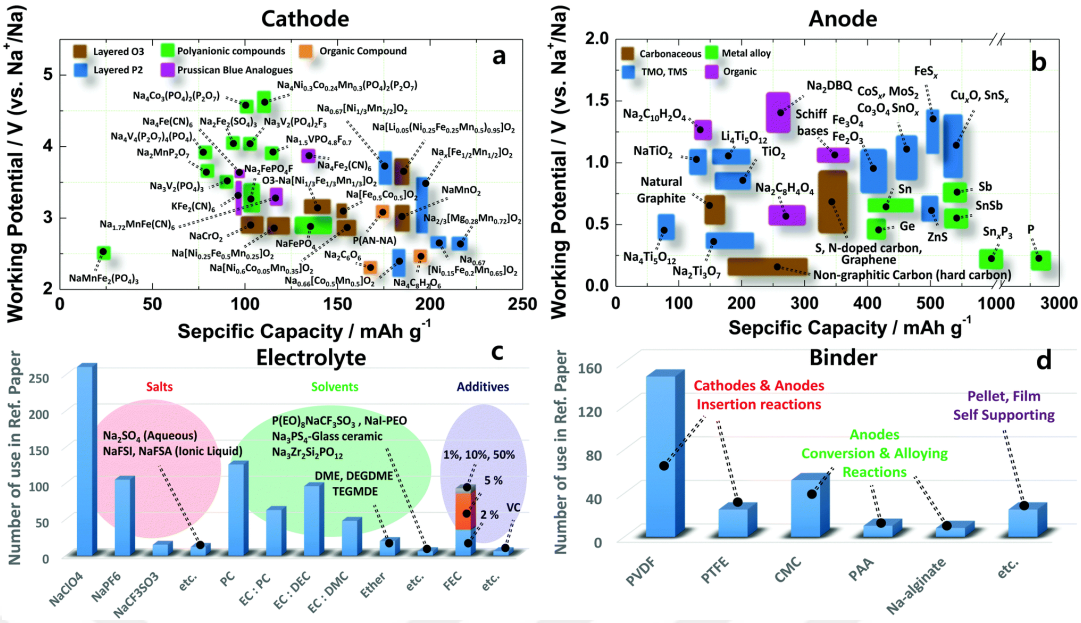

Figure 2. Cathode (a), anode (b), electrolyte (c), and binder (d) materials used in sodium ion batteries studied in the literature. Source: Hwang et al [34].

1.3.1. SIBs Cathode Materials

The cathode materials used in SIBs must have good host properties similar to LIB cathode materials to ensure high capacity and long cycle life. This can be achieved by maintaining the crystalline stability of the cathode material during the insertion of Na ions. Similarly, the Na^+ ion has a larger radius when compared to the Li^+ ion, which means that the change in the crystal structure is greater during the operation of the battery. Therefore, a detailed study of the crystal structure properties of the cathode materials used is instrumental.

In the early studies of sodium ion batteries, TiS_2 and Na_xCoO_2 materials were used as a cathode, as well as anode sodium-lead alloy [35,36]. After undertaking these fundamental studies, it was concluded that the primary concerns can be overcome and many different variations of the cathode material (tunnel or layered transition metal oxide [37–39], sulfides [40], polyanionic [41], and organic carboxylates and polymers [42–44] were produced.

1.3.1.1. Monoanion Cathodes

1.3.1.1.1. Metal Oxides (MO_x)

Monoanions are categorized as metal oxides (MO_x) and sodium metal oxides ($NaMO_x$) based on their composition. Here, M is a transition metal such as Mn [45,46], V [47,48], Ni [49], Fe [50], etc.

Metal oxides (MO_x), as will be elaborated in the next section, have been used in several different areas of the industry due to their unique properties. On the other hand, they are attractive materials for sodium-ion batteries due to their easy synthesis [48], long cycle life [51], and relatively high specific capacity [52].

MnO_2 is a widely used nanocomposite in the industry with use in water cleaning [53], and as a catalyst [54] and artificial oxidase [55], etc. However, the high theoretical capacity (308 mAh / g), low cost and low toxicity defend the use of this material in the battery industry. Another interesting feature is that it can be synthesized in many different forms of nano-structures, such as nanorods [56], nanospheres [57], nanotubes [58] and nano-disks [59], according to the production conditions. Some different tunnel structures of MnO_2 can be observed in Figure 3.

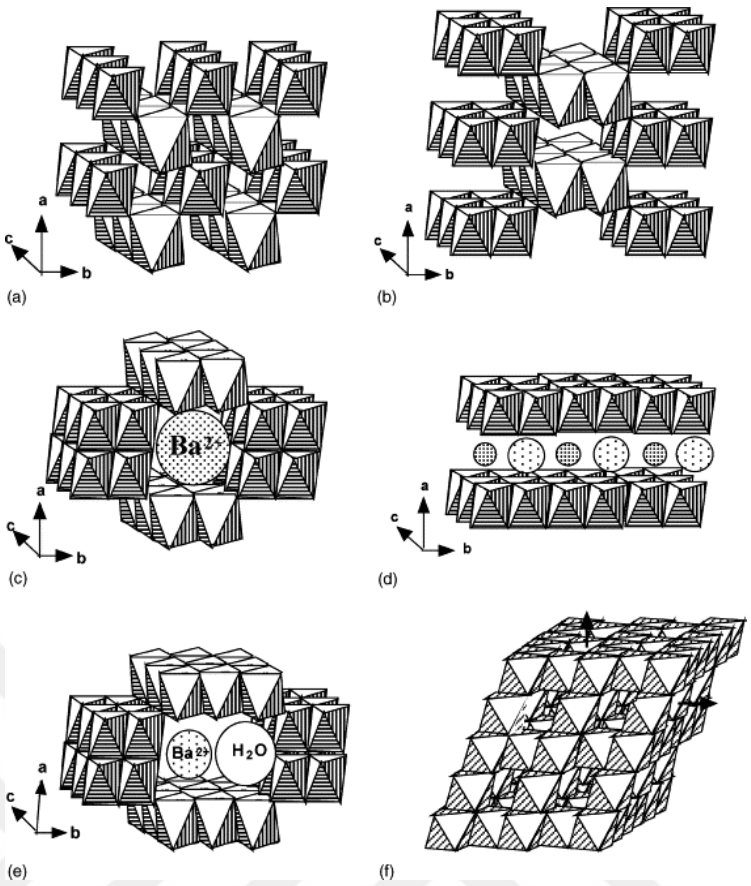

Figure 3. Different manganese dioxide schematics: (a) pyrolusite, (b) ramsdellite, (c) hollandite, (d) birnessite, (e) romanechite, and (f) spinel [60].

Although MnO_2 is a composite that was originally intended for Li-ion batteries [61], SIBs were also used in a short time due to the above-mentioned characteristics. For example, Su et al. used the hydrothermal synthesis technique to produce α-MnO_2 and β-MnO_2 and obtained 278 mAh / g and 298 mAh / g specific capacity, respectively, from these materials which they used as cathode material for SIBs [46].

Vanadium oxide (VO_2) is another monoanion with a wide range of applications such as in the form of catalysts [62], and in chemical sensor [63], memory device [64], and lithium ion batteries [65] due to its chemical and physical properties similar to MnO_2.

So far, VO_2 material has been synthesized in different form, such as rutile (VO_2 [R]) [66], monoclinic (VO_2 [M_1]) (VO_2 [M_2]) [67], (VO_2 [B]) [68], tetragonal (VO_2 [A]) [69] and paramontroseite [70]. Within these phases, VO2 (B) is nano-size and has different structures (such as nanorods [71], nanowires [72], nanospheres [73]) and thus it can be produced with large areas and short reduction distances [74]. Thereby, they have the ideal structure for energy storage systems. In the crystal structure of this phase, the VO_6 shares both the corners and edges of the octahedral structures and thereby forms shorter diffusion channels [75]. These short diffusion channels and

large surface area support high capacity access. For example, Baudrin et al. have reached a specific capacity of 500 mAh / g in their study using the VO_2 (B) phase (Figure 4) [76].

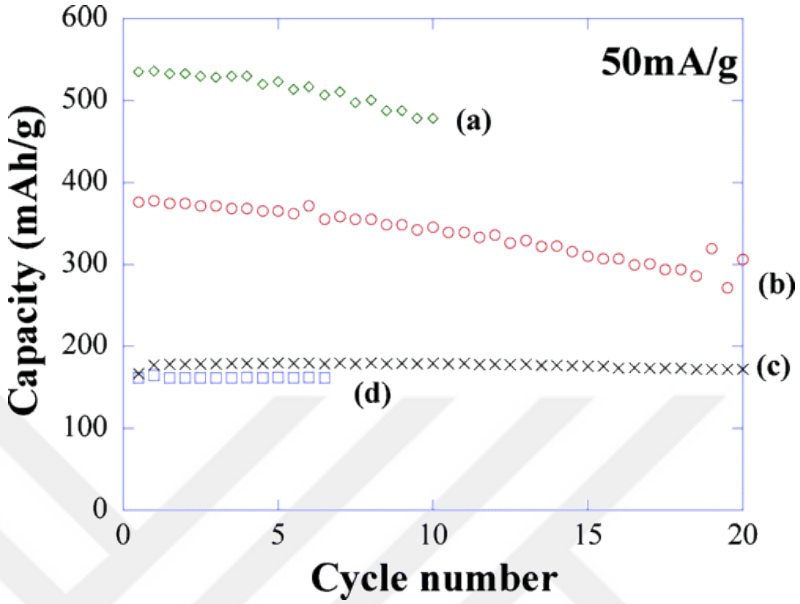

Figure 4. Cyclic performance of VO_2[B] materials in different temperature and different voltage range. (a) and (c) vacuum-heated to 280 °C, and (b) and (d) to 400 °C. The voltage range for (a) and (b) is 4 to 1.5 V and the voltage range for (c) and (d) is 4 to 2.4 V [76].

Wang et al. used VO_2 in sodium-ion batteries (Figure 5) and observed a stable 70 mAh /g specific capacity over 50 cycles although they increased to a current density of 1000 mA /g [77].

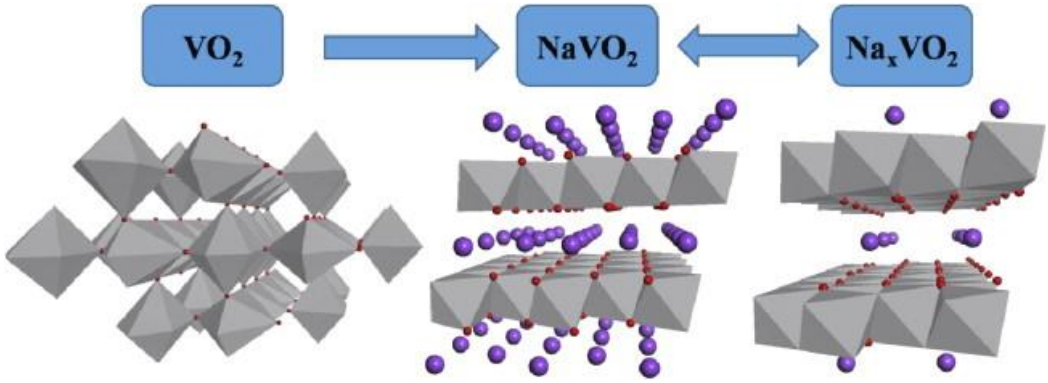

Figure 5. The crystal structure changing and position of Na ions positions in the VO_2 during the insertion and extraction process [77].

Vanadium pentoxide (V_2O_5) has been reported in early studies to possess higher chemical stability. V_2O_5 has two different crystal structures, orthorhombic and layered. Moreover, it has been reported that the layered V_2O_5 has better

electrochemical performance than the orthorhombic V_2O_5 due to the larger d-spacing [78,79]. Combinations with various conductive carbons and different synthesis methods, such as sol-gel [80], hydrothermal [81], electrospinning [82], were investigated for higher capacity V_2O_5. Recently, Wei et al. reported that high specific capacity $V_2O_5.nH_2O$ is synthesized by a facile freeze-drying process [83]. The water molecules intercalated into the layer structure during the synthesis, thus the new structure has larger d-spacing than the orthorhombic V_2O_5 (Figure 6). Due to the larger d-spacing, the diffusion channels are larger and shorter, and as a result of all of these effects, $V_2O_5.nH_2O$ exhibited an excellent electrochemical performance (338 mAh/g at 0.05 A/g).

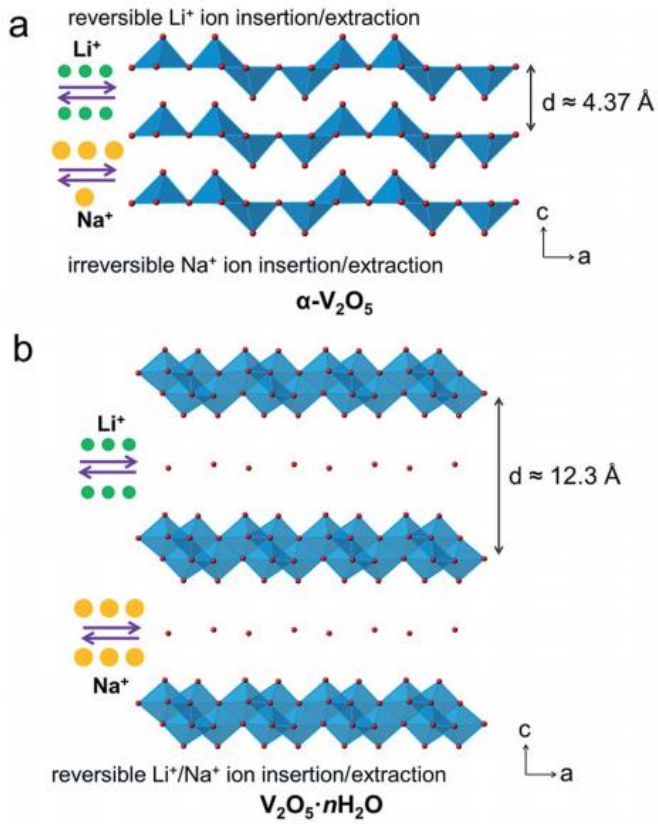

Figure 6. The crystal structure of (a) alpha-V_2O_5 and (b) $V_2O_5.nH_2O$ [83].

Raju et al. reported that they increased the specific capacity of orthorhombic V_2O_5 to 276 mAh / g, which is higher than the unmodified V_2O_5 (170 mAh / g), by nanoporous carbon encapsulation. Thus, they solved the problem of low Na diffusion rate of orthorhombic V_2O_5 [84].

1.3.1.1.2. Sodium Metal Oxides ($NaMO_x$)

The $NaMO_x$s are another group of sodium ion cathode material, the major ones are $NaNiO_2$, $NaCoO_2$, $NaMnO_2$, and these sodium metal oxide cathode materials have been reviewed in detail in this section.

The $NaNiO_2$ crystal structure was first investigated by Dyer et al. [85]. According to this study, this structure has a transformation temperature about 220 ^{0}C. The low-temperature crystal structure is a distorted monoclinic, while the high temperature referred to a hexagonal form.

Molenda and Stoklosa have demonstrated the connection between the electrochemical properties of $NaNiO_2$ and its thermoelectric and electrical conductivity properties [86]. In their study, they observed that the activation energy of 0.24 eV to 0.36 eV in the semiconductor metallic transition observed at 600K is related to the voltage jump between 3V and 2.5V, which can be observed in the discharge curve. The common point between these two situations is the transformation of the crystal structure and the subsequent change of the electron structure. This is, in other words, the change of the Fermi energy. The results obtained from the electrochemical tests showed that sodium ions could be deintercalated from the cathode only 0.2Na per mole due to the increase of activation energy.

Vassilaras et al. re-investigated the $NaNiO_2$ capacity values by changing the operating voltage range [87]. With $NaNiO_2$ produced by solid state reaction method, 147 mAh / g charge and 123 mAh / g discharge capacity were obtained in 1.25-3.75 V operating voltage. In 2.0-4.5 V operating voltage, 199 mAh / g charge and 147 mAh / g discharge capacity were obtained. However, the reason behind the extra capacity in the high working range being not reversible, that implies low Coulombic efficiency is explained by the decomposition of the electrolyte and the passivation of the electrode surface by impurity phases.

The $NaCoO_2$ compound, which is particularly popular for its thermoelectric properties and has been investigated for many different properties [88–90], has been observed to have a capacity of 90 mAh/g as a result of electrochemical tests [91]. In order to increase the capacity values, changes in the crystal form were made and the general form was determined as Na_xCoO_2. The Na_xCoO_2 crystal structure was first examined by Jansen and Hoppe [92], and the high temperature phase diagram is detailed by

Fouassier et al. [93]. Kim et al. reported that Na_xCoO_2 material was primarily divided into two main phases: P2 and O3. While O and P respectively define the octahedral and prismatic structures, the numerical definitions define the number of periods of Co_x layers stacked perpendicularly to the Na layers (Figure 7).

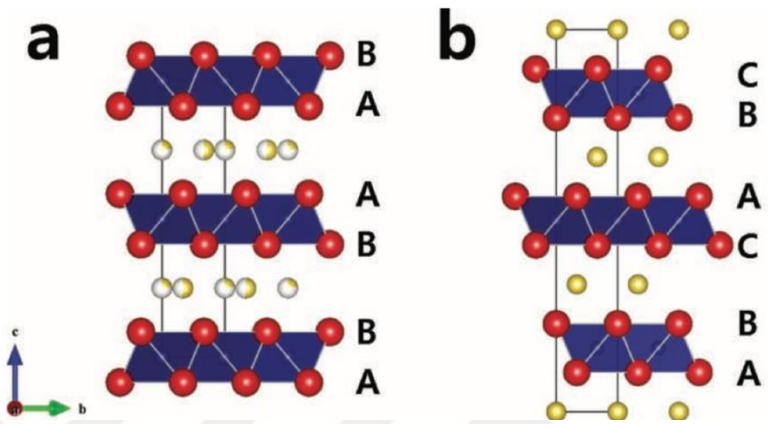

Figure 7. The crystal structure of (a) P2-Na_xCoO_2 and (b) O3-Na_xCoO_2 (Na: yellow, Co: blue, O: red). Reprinted from [94].

In the detailed studies conducted for the phase diagram, a temperature-dependent phase map of the phases that may occur according to the Na: Co ratio was established and showed that the phases P'3 and O'3 could occur in addition to the main phases P2 and O3 (Figure 8) [95].

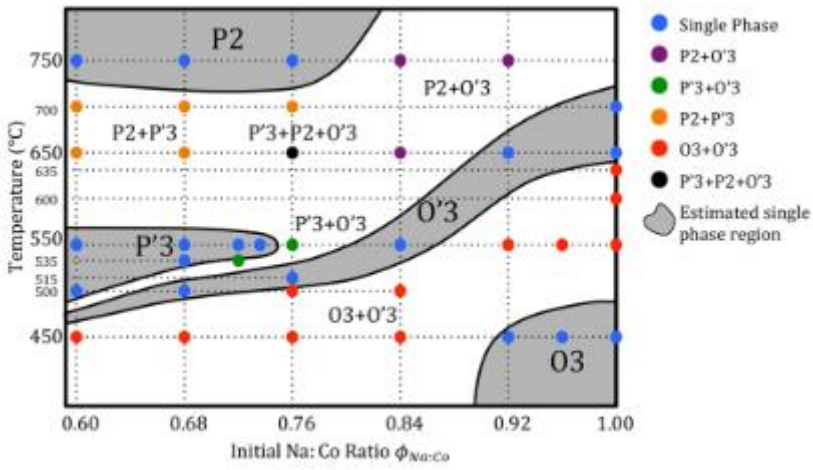

Figure 8. Synthesis phase diagram of Na_xCoO_2 as a function of theprecursor Na:Co ratio φ Na:Co(X-axis) and the sintering temperature (Y axis) [95].

The Na_xCoO_2 material was used as a positive electrode by Braconnier et al. [25] and Shaklette et al. [96] in SIBs, and the crystal structures of O3 (x=1), O'3 (x=0.77), P2 ($0.64 \leq x \leq 0.77$), and P'3 ($0.55 \leq x \leq 0.60$) are reported based on the amount of sodium. Changes in the crystal structure during battery operation were investigated by Berthelot et al. In the study, the relation of electrochemical properties with crystal structure changes was investigated in the potential range of 2.1 V to 3.1 V using in-situe XRD technique (Figure 9). As a result of the study, three new phases with x = 0.72, 0.76 and 0.79 and creating a total of nine phases in the range of $0.5 \leq x < 1$ for Na_xCoO_2 material were reported.

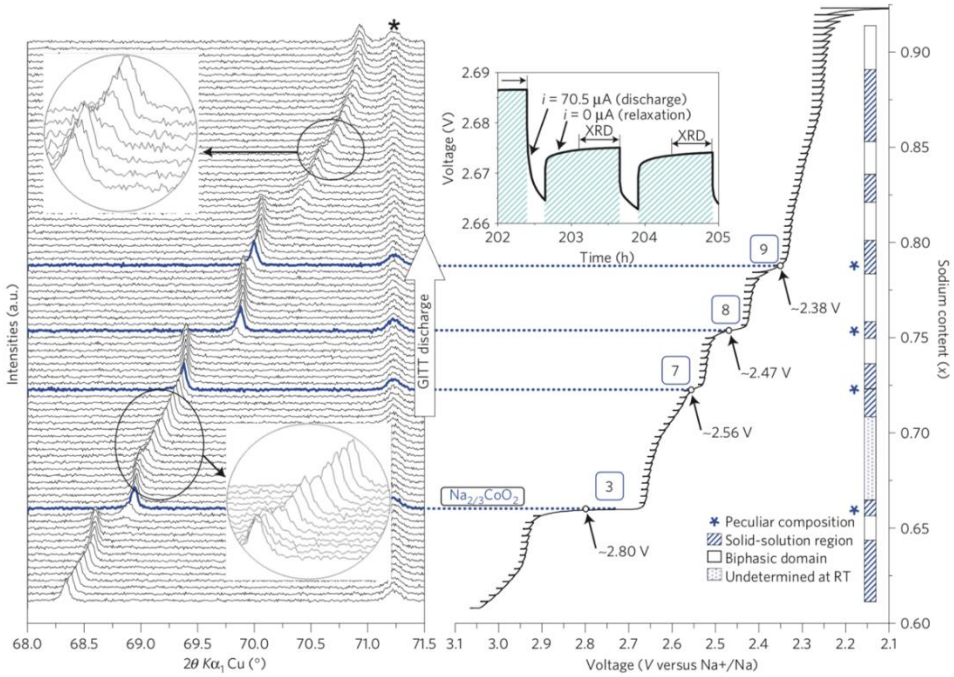

Figure 9. In-situ XRD test for Na_xCoO_2. In the measurement, the battery was discharged with GITT method and the potential values corresponding to the crystal transition were observed [36].

One of the favored Na_xCoO_2 compounds is $Na_{0.7}CoO_2$. In studies on electrochemical properties, a sample of $Na_{0.7}CoO_2$ material synthesized by solid-state reaction reached a capacity value of 107 mAh/g with a potential range 2.0 to 3.8 V at 0.1C [97]. Furthermore, D'Arienzo et al. investigated the effect of starting components on electrochemical properties [39]. In this study, $Na_{0.71}CoO_2$ material was synthesized by hydrothermal synthesis using two different Na source Na_2CO_3 and NaOH with Co_3O_4 and the effects of crystal morphology on battery capacity was investigated. The researchers concluded that the compound produced with Na_2CO_3 sodium source has a shorter crystal size than that of the compound produced with NaOH. A shorter crystal

size results in faster diffusion which further implies superior kinetic properties. As can be observed from Figure 10, the specific capacity values of the compound produced with Na_2CO_3 were significantly higher.

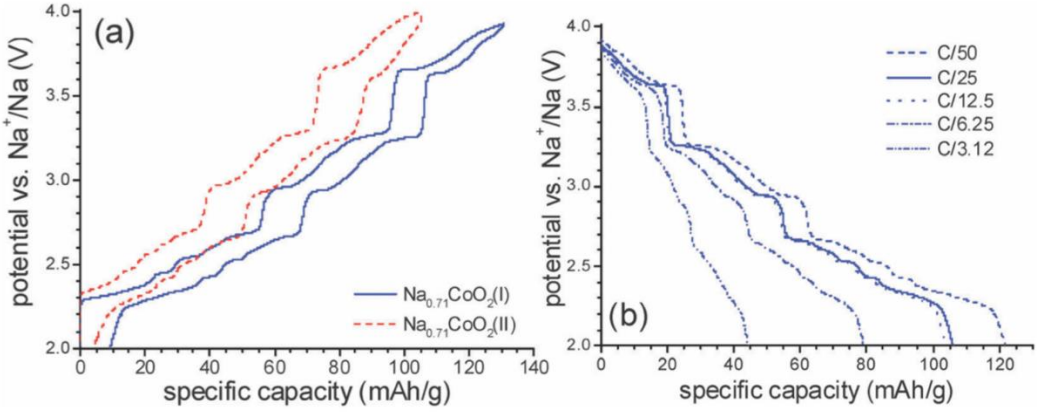

Figure 10. (a) The charge/discharge curve of N_2CO_3(I) and NOH(II) at C/50 rate and (b) specific capacity measurements of NOH (II) samples in different C rates [39].

Recent research shows the effects of the synthesis techniques on the material morphology. In one of these studies, the production of $Na_{0.7}CoO_2$ material was performed using solid state reaction, high energy ball milling and sol-gel methods and their morphologies were investigated. Among these methods, it was reported that the material produced by the sol-gel method had higher stoichiometry compared to other methods and showed higher electrochemical performance than other production methods [98].

Na_xMnO_2 is one of the extensively investigated material among manganese-based oxide cathode materials. There are two main phases for Na_xMnO_2; tunnel type for $x<0.44$ (mentioned in the next section) and P2 type for $x>0.7$ [99].

P2 type layered $Na_{0.7}MnO_2$ is an extremely attractive cathode material because of easy synthesis, low cost, and high theoretical capacity (200 mAh/g). On the other hand, P2 to O2 phase transformation at high voltage is the cause of capacity fade. Additionally, because of the orthorhombic distortion and Jahn-Teller (JT) effect, Mn^{+3} distribution become irregular, and, the amount of active material decreases resultantly and the battery impedance increases [100,101]. The JT effect, which is usually observed in transition metals in octahedral environment, explains the geometric deterioration of molecules and ions resulting from electron configurations [102]. In order to overcome these problems, researchers tried different methods, such as element substitution or surface coating. For example, Clement et al. [103] recommended Mg substitution for

Mn in a $Na_{0.7}MnO_2$ compound to solve the inhibit phase transformation. They reported that 5% Mg doping suppress the JT transition and contributes to high capacity retention after 50 cycles (Figure 11).

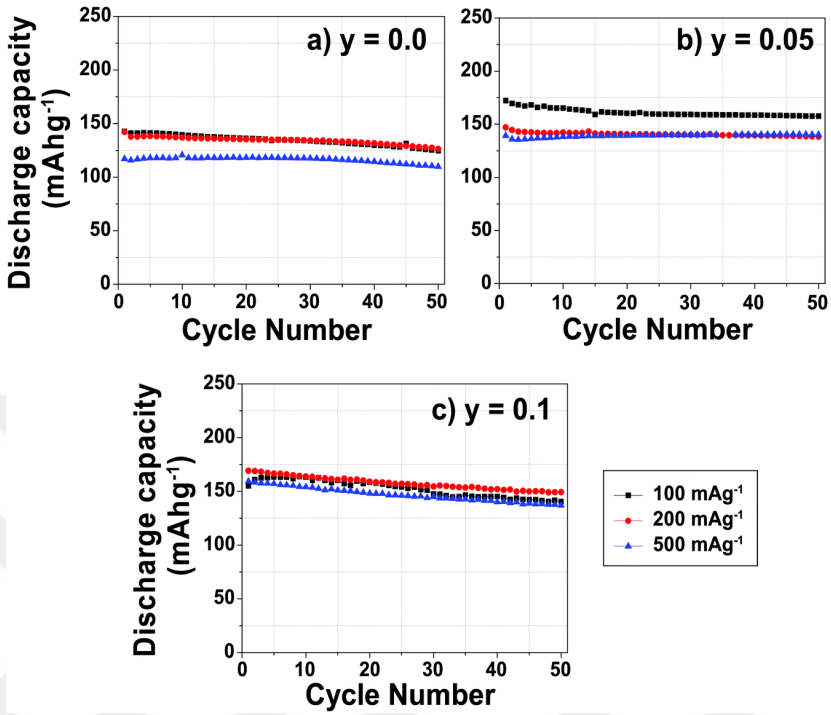

Figure 11. Cycling performance for $Na_{2/3}Mn_{1-y}Mg_yO_2$: (a) y = 0.0; (b) y = 0.05; and (c) y = 0.1 [103].

In another study with surface modification, P2- $Na_{2/3}Ni_{1/3}Mn_{2/3}O_2$ was coated with Al_2O_3 and battery performance was investigated [104]. At this point, the contribution of Al_2O_3 is to suppress the side reaction on the surface during the charge / discharge of the battery and to prevent the deformation of the crystal structure. However, at the end of 300 cycles between 2.5 V and 4.3V, the non-coating compound and the Al_2O_3 coated compound showed 28% and 78% capacity retention, respectively (Figure 12).

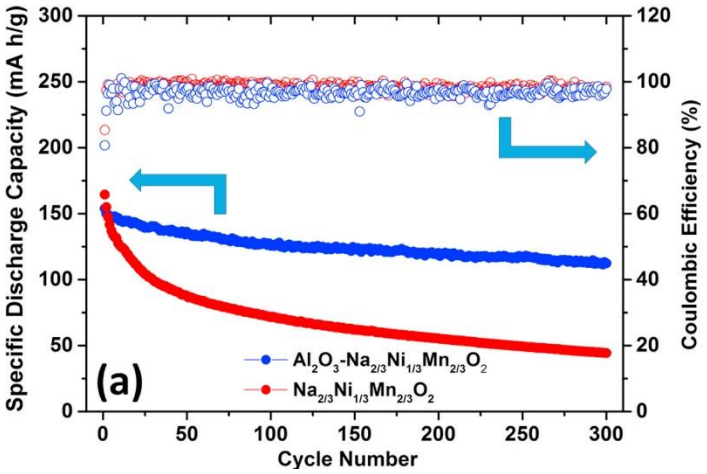

Figure 12. Electrochemical behavior of the as-prepared $Na_{2/3}[Ni_{1/3}Mn_{2/3}]O_2$ and Al_2O_3-$Na_{2/3}[Ni_{1/3}Mn_{2/3}]O_2$ for 300 cycle [104].

When the $NaMnO_2$ compound is examined, two different phases are observed: α-$NaMnO_2$ and β-$NaMnO_2$. The first one is a low temperature phase and has an O3 layered structure. On the other hand, because of the JT effect on Mn^{+3} ions, monoclinic distortion is observed [99]. The latter is a high temperature and orthorhombic phase, and it has different layered structure (MnO_2 and MnO_6) [105]. Billaud et al. [106] investigated the electrochemical behavior of β-$NaMnO_2$ and they reported that 190 mAh/g capacity at C/20 and good reversibility at a 2C rate (Figure 13).

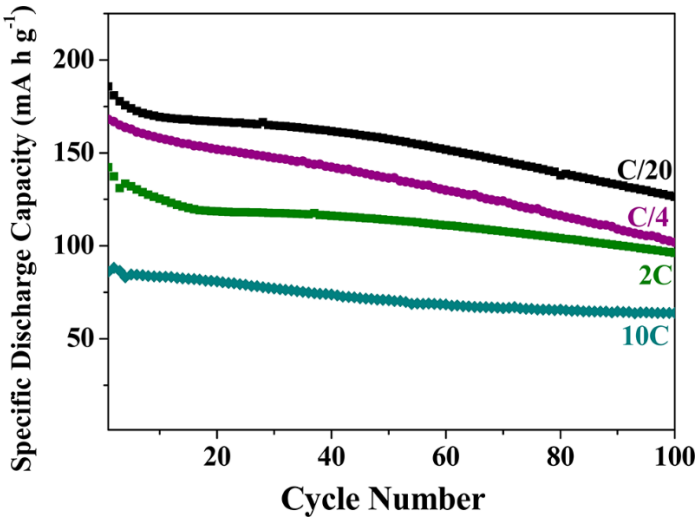

Figure 13. Specific discharge capacities as a function of cycle numbers for β-$NaMnO_2$ cycled between 2 and 4.2 V [106].

In addition to the above-mentioned oxides, alternative cathode materials, such as $NaCrO_2$ [107], $NaNbO_2$ [108], and $NaFeO_2$ [109] were also examined to obtain high performance in SIB batteries. Among them, $NaFeO_2$ is especially notable for its high

theoretical capacity value (242 mAh / g) and low-cost advantage. Unfortunately, despite these important advantages, the crystal structure deteriorates due to the JT effect on Fe^{+3} ions and its capacity cannot be fully utilized. However, Takeda et al. reported possible Fe^{+3}/Fe^{+4} redox reaction in half cell with a lithium counter electrode by Mössbauer spectroscopy [110]. The first study of $NaFeO_2$ with Na counter electrode cell was performed by Okada et al. [50]. The cell that used Na as the counter electrode was tested between 1.5 V and 3.6 V and a discharge capacity of 85 mAh/g was observed. All of these studies show that the $NaFeO_2$ compound is a promising electrode material and that various modifications may affect the capacity increase.

1.3.1.2. Mixed Cation Oxide Cathodes

The primary purpose of mixed anion cathode materials is not only to increase the electrochemical yield but also to increase the structural stability. Additionally, another goal is to reduce the cost of production by using other elements that are low in cost.
Hwang et al. [111] produced a compound with different layered hierarchical spherical structure (Na $[Ni_{0.75}Co_{0.02}MnO_{0.23}]$ 02 in the interior and Na $[Ni_{0.58}C_{0.06}Mn_{0.36}]$ 0_2 in the outer part) by the co-production method. In the mentioned study where $Ni^{+2,+3,+4}$ transitions were provided during charge / discharge, 157 mAh / g discharge capacity (15 mA / g) and 80% capacity retention in 300 cycles were obtained. Additionally, it has been reported that efficient electrochemical results are obtained from the material at ambient temperatures (25 ^{0}C) other than room temperature (Figure 14).

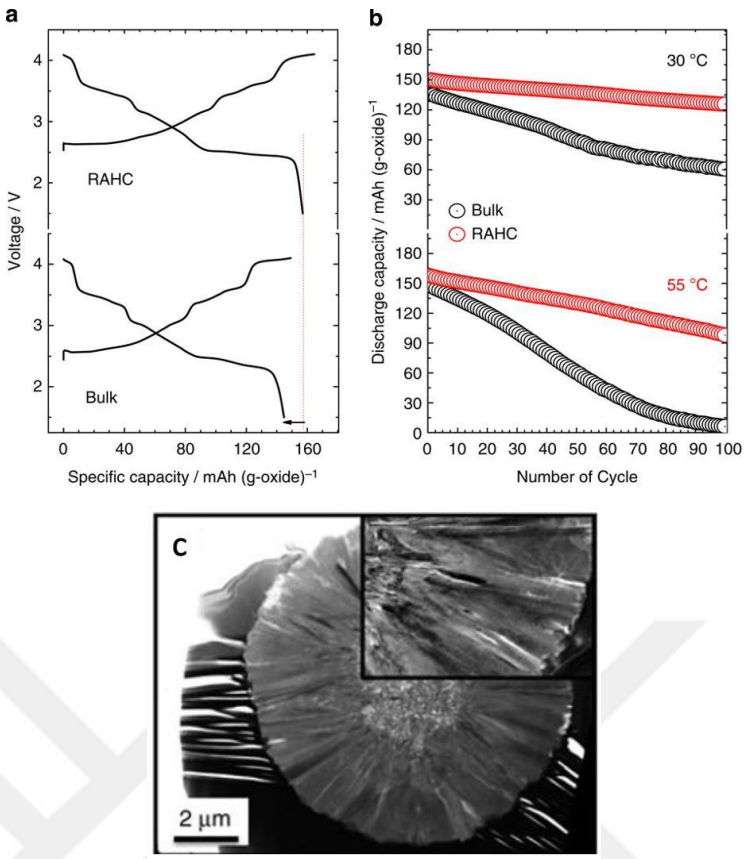

Figure 14. a) First charge–discharge curves and (b) cycle retention of the Radially Aligned Hierarchical Columnar (RAHC) and bulk electrodes using Na metal anode, (c) cross-sectional TEM image of RAHC $[Ni_{0.60}Co_{0.05}Mn_{0.35}](OH)_2$ [111].

In the study of Na batteries that can work safely and efficiently in high cycles, Gou and colleagues [112] successfully synthesized $Na_{0.66}Ni_{0.17}Co_{0.17}Ti_{0.66}O_2$ compound and an average working capacity of 92 mAh / g was obtained as a result of 1000 cycles. Furthermore, during high current density tests, 65 mAh / g capacity was observed in batteries at 2C rate. Similarly, Han et al. [113] produced the Ti doped $Na_{2/3}Mn_{0.8}Fe_{0.1}Ti_{0.1}O_2$ compound by the ceramic method and investigated the structural stabilization and electrochemical behavior. The compound maintained 87.7% of the initial capacity of 144 mAh / g at the end of 300 cycles between the 2.0-4.0 V range at 1C (Figure 15).

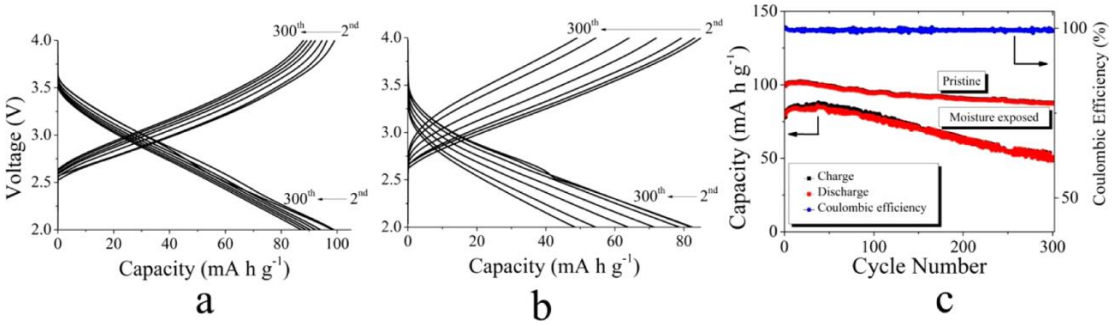

Figure 15. Charge/discharge curve of (a) pristine P2-phase $Na_{2/3}Mn_{0.8}Fe_{0.1}Ti_{0.1}O_2$ and (b) moisture-exposed $Na_{2/3}Mn_{0.8}Fe_{0.1}Ti_{0.1}O_2$. (c) cyclic performance and Coulombic efficiency within the voltage range 4.0−2.0 V at 1C for 300 cycles [113].

The effect of the synthesis techniques on the compound morphology and thus the capacity yield is quite high. An example of this is the work of Kalluri et al. that produces the mixed oxide compound $Na_{2/3}(Fe_{1/2}Mn_{1/2})O_2$ by electrospinning [114]. One advantage of this method is that self-aggregation, which is undesirable property for nanostructures since reducing reaction area, is avoided in nanofibers. Thus, the interactions between nano-fiber structures and the electrolyte become more efficient with this method. The data obtained by comparing the materials produced by electrospinning (NFMO NF) and sol-gel method (NFMO NP), furthermore, reports that nano-fiber structures are more efficient and the 195 mAh / g initial capacity has been reached (Figure 16).

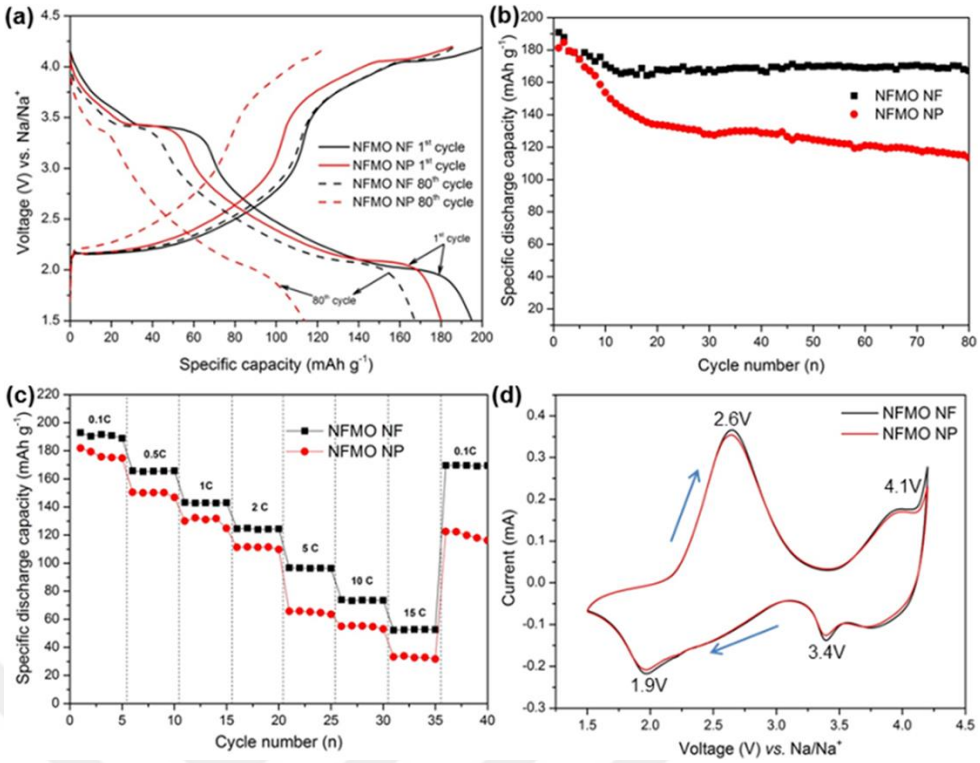

Figure 16. (a) Charge/discharge curves of NFMO NF and NFMO NP at the 1st and 80th cycles at the 0.1 C current rate, (b) cycling performance, (c) current rate performance, and (d) CV curve of NFMO NF and NFMO NP between 1.5−4.2 V voltage range at 0.1 mV/s scan rate [114].

In addition to these studies, crystal structure stabilization studies were performed by using electrochemically inactive elements (Sb, Mg etc.) in the substitution process [115,116]. For example, Billaud et al. aimed to prevent the deformations occurring during the insertion/extraction of Na by substituting Mn^{+3} ions with Mg^{+2} in the $Na_{0.67}Mn_{1-x}Mg_xO_2$ compound [117]. They observed that the $Na_{0.67}Mn_{0.95}Mg_{0.05}O_2$ compound has a smoother voltage curve structure instead of stepped one, which indicates the low number of phase transitions, in the charge/discharge curve.

Other than the above-mentioned compounds, a few P2-type cathode materials reported with multiple element doping, such as $Na_{0.67}Mn_{0.65}Co_{0.2}Ni_{0.15}O_2$ [118], $Na_{0.45}Co_{0.11}Mn_{0.66}O_2$ [119], $Na_{2/3}[Ni_{1/3}Mn_xTi_{2/3-x}]O_2$ [120], $Na_{2/3}Ni_{1/3}Mn_{2/3-x}Ti_xO_2$ [121] and $Na_xCo_{2/3}Mn_{2/9}Ni_{1/9}O_2$ [122]. All of these synthesized compounds have their unique morphologies and production techniques.

1.3.1.3. $Na_{0.44}MnO_2$ Cathode Material

Recently, the $Na_{0.44}MnO_2$ compound has been one of the most attractive electrode materials due to its 1D nano-crystal morphology (tends to grow in c-axes) [123–125] and high theoretical capacity (121 mAh/g) [126]. Moreover, it can tolerate stressing during the diffusion of sodium ions that have wide ionic radii with the tunnel structures; this is an instrumental behavior benefitting the use of a compound as an electrode in long-term battery use. On the other hand, one of the negative features of this compound is low capacity retention in long cycles and low capacity at high current rates [127]. In order to overcome this problem, alternative production techniques and surface morphology modifications have been attempted. These will be specified in a later section. Another negative feature is the JT distortion observed on Mn^{+3} ions during charge / discharge. In the long term, this situation leads to a degradation in the crystal structure and causes capacity fade. A solution to prevent the JT effect is to partially replace the Mn atom with an element of a similar electronic structure [128,129].

$Na_{0.44}MnO_2$ was first studied in 1971 by Hegenmüller et al. According to the amount of sodium in the compound, there are three different composition types: a tunnel crystal structure at a concentration of $0.22 \leq x \leq 0.44$, a layered crystal structure at a concentration of $0.66 \leq x \leq 1$, and a mixture of layered and tunnel crystal structures between these two concentrations [130]. It has been reported that $Na_{0.44}MnO_2$ composition has an orthorhombic (Pbam space group) symmetry, and a large and small pentagon S-shaped tunnel structure that consists of combinations of MnO_5 square pyramid and MnO_6 octahedral structures (Figure 17) [131]. The large S-tunnel forms the diffusion path of the sodium ions, while the small S-tunnel maintains the stability of the crystal structure during the diffusion (without contributing to diffusion) [132]. Doeff and colleagues are the first team to use the material $Na_{0.44}MnO_2$ as a cathode with solid polymer electrolyte [133]. In this study, Doeff and colleagues tried the $Na_{0.44}MnO_2$ composition for both Na and Li batteries, and unexpectedly experienced a lower capacity loss in the Li batteries. Sauvage et al. performed in-situ XRD experiments to more comprehensively understand the insertion/extraction mechanism. With these experiments, they observed that there are six different phases that are significantly close and connected with each other between 2V and 3.8V [134].

As a result of the electrochemical test, $Na_{0.44}MnO_2$ showed an initial capacity of 80 mAh / g at 0.1 C rate. Due to the large ionic radius, however, Na ions defected the crystal structure during the insertion/extraction, and, could maintain only half of its initial capacity at the end of 50 cycles.

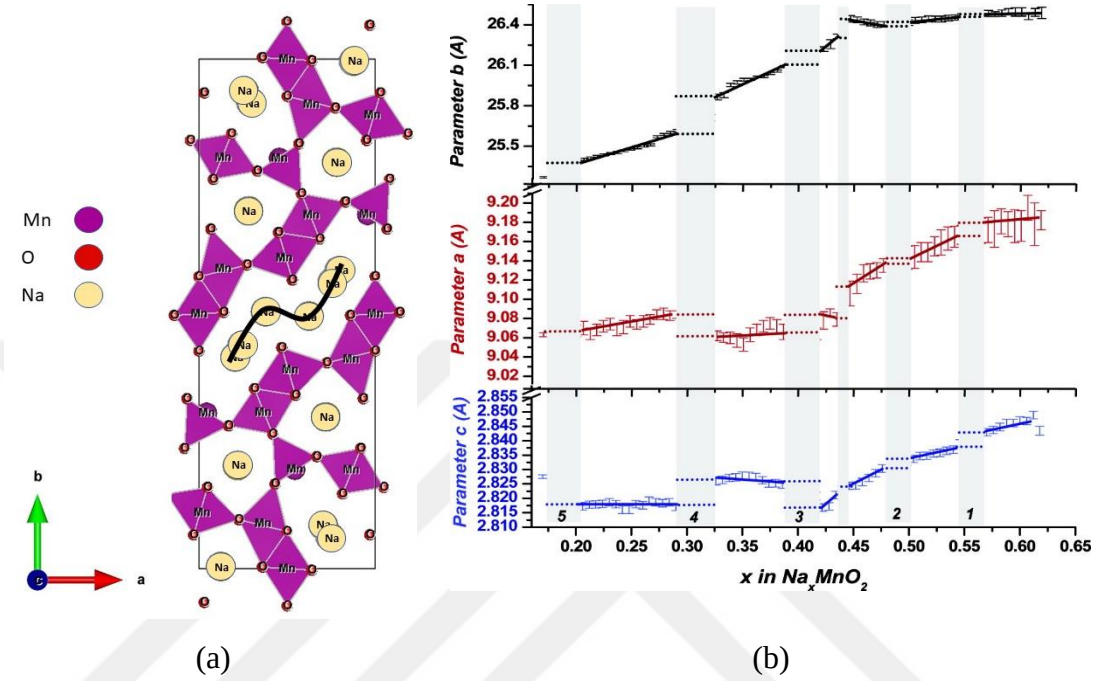

(a) (b)

Figure 17 (a) The crystal structure of $Na_{0.44}MnO_2$. The S-shape tunnel structure in the middle section is highlighted with a black line [135]. (b) The change in the crystal parameters of Na_xMnO_2 compound in the $0.18 \leq x \leq 0.64$ sodium composition range according to the in-situ XRD results [134].

To enhance the electrochemical behavior, various synthesis methods have been attempted for $Na_{0.44}MnO_2$, such as the hydrothermal[136,137], electrospun [138], sol-gel [139], molten salt [140], spray pyrolysis [141], and modified-Pechini method [142,143].

Cao et al. were synthesized single-crystalline, homogenous $Na_{0.44}MnO_2$ nanowire with polymer pyrolysis method. The nanowires have shown 128 mAh/g reversible capacity at 0.1 C rate and 77% capacity retention during the 1000 cycle at 0.5 C (Figure 18) [144]. Xu et al. were created ultra-long (10-40 μm length) $Na_{0.44}MnO_2$ nanowires by the sol-gel method. They reported that after the electrochemical characterization, the material showed more than 120 mAh/g stable capacity, that is an actual theorical capacity of $Na_{0.44}MnO_2$, over 100 cycles [142].

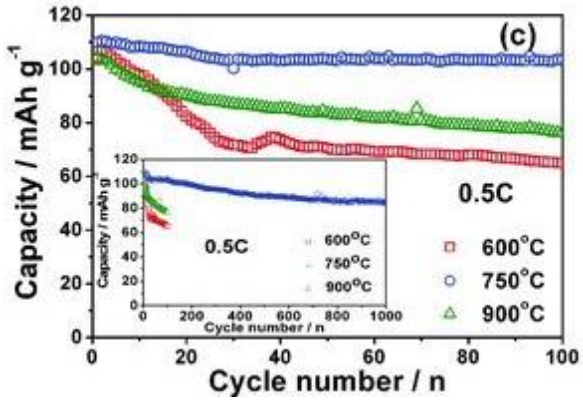

Figure 18. Cyclic performance of $N_4Mn_9O_{18}$ samples calcined at different temperatures. Represented from Cao et al. [144].

In order to increase battery performance, some researchers have tried the atomic substitution method in the composition. For example, Chen et al. [145] synthesized the cobalt-substituted $Na_{0.44}Mn_{1-x}Co_xO_2$ phase by thermopolymerization method to ensure high Na-ion battery performance. As a result of the structural analysis, they observed that P-2 (layered) and P-3 (granular) type new phases were formed by the increasing amount of substitution. On the other hand, it has been reported that in the electrochemical tests of up to x = 0.11 Co substitution, the capacity values increased with the contribution of P-2 type phase (Figure 19).

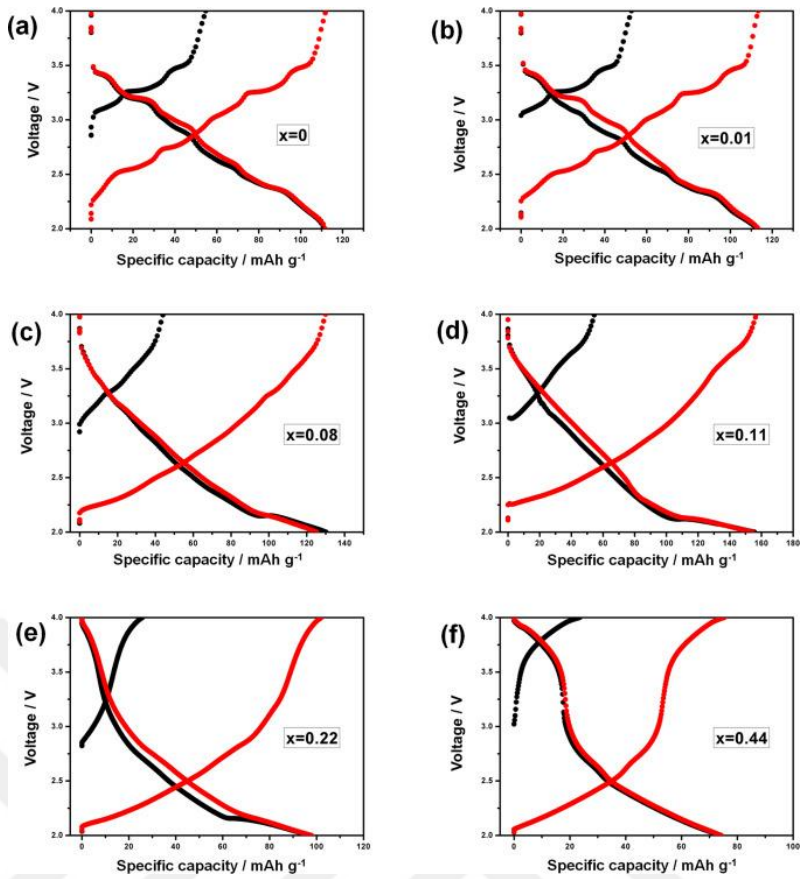

Figure 19. The first (black line) and second (red line) charge–discharge curves of $Na_{0.44}Mn_{1-x}Co_xO_2$, where x = 0 (a), 0.01 (b), 0.08 (c), 0.11 (d), 0.22 (e) and 0.44 (f). represented from Chen et al. [145].

Wang and his colleagues are another team who tried the substitution method to enhance battery performance [129]. They synthesized the tunnel type $Na_{0.44}Mn_{1-x}Ti_xO_2$ ($0 \leq x \leq 0.56$) compound via the solid-state route. As a result of the analyses, Ti substitution process was observed to create a smoother profile instead of the transitional regions in the charge/discharge voltage profile and reduce the storage voltage. Both $Na_{0.44}MnO_2$ and $Na_{0.44}Mn_{0.44}Ti_{0.56}O_2$ showed strong structural stability and more than 96% capacity retentions after 1100 cycle.

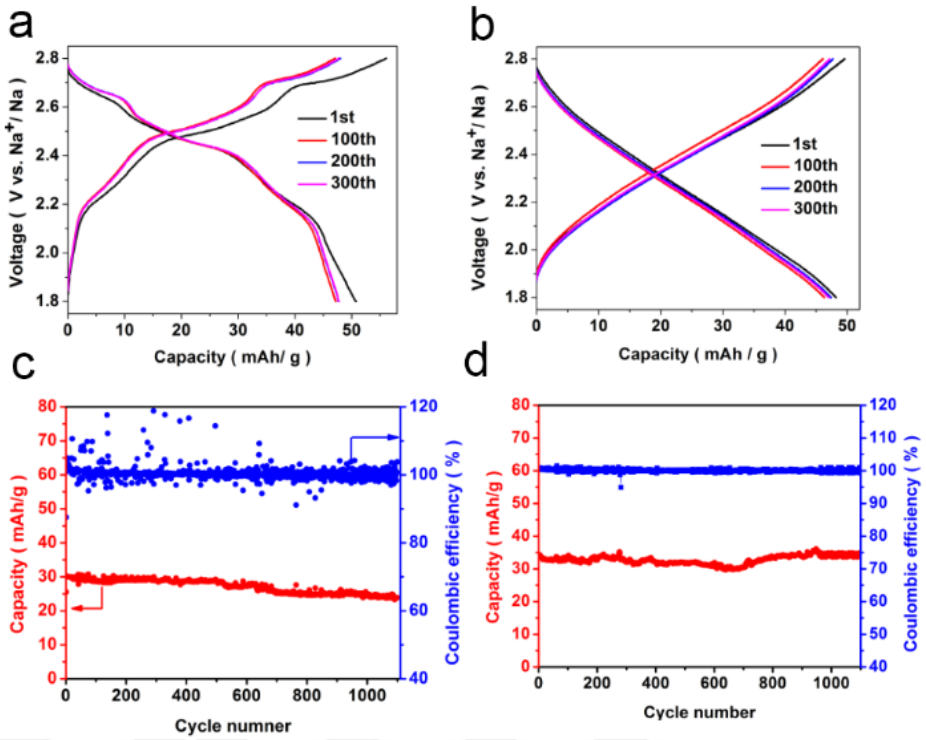

Figure 20. The charge/discharge profiles of (a) $Na_{0.44}MnO_2$ and (b) $Na_{0.44}[Mn_{0.44}Ti_{0.56}]O_2$ at a current rate at 0.1C. Long-term cycling performance at a current rate of 1C (c) $Na_{0.44}MnO_2$ and (d) $Na_{0.44}[Mn_{0.44}Ti_{0.56}]O_2$. Represented from Wang et al. [129].

In this study, Mn ions have been substituted with Ni and Co ions, that have electronic structures similar to Mn, in order to overcome the JT effect and increase the stabilization of the crystal structure of $Na_{0.44}MnO_2$ and thus to reduce the capacity fade in long cycles.

2. METHODOLOGY

2.1. Sample Synthesis

Two different series, $Na_{0.44}Mn_{1-x}Ni_xO_2$ and $Na_{0.44}Mn_{1-x}Co_xO_2$ (x=0.01, 0.05, 0.08, 0.11, 0.16) were synthesized via the solid-state reaction method. The chemical quantities to be used for each sample were calculated using the chemical stoichiometry of the samples. Na_2CO_3 (Sigma Aldrich, > 99%), $MnCO_3$ (Sigma Aldrich, > 99%), NiO (Sigma Aldrich, > 99%), Co_3O_4 (Sigma Aldrich, > 99%) were used to synthesize all the samples. The precursors weighed with a precision balance and mixed with ball milling for one hour for homogenization. The samples were placed in the alumina crucible and calcined for eight hours at 300 °C. After calcination, the mixture, that turned black was again mixed with the ball mill for one hour. To obtain the final phase, a heat treatment was applied for nine hours at 800 °C [125,134]. All the thermal processes were performed at 5 ^{0}C/min heating rate.

2.2. Electrolyte Preparation

For the electrolyte, 1 M $NaClO_4$ in a mixture of ethylene carbonate (EC) and propylene carbonate (PC) (1:1 wt./wt.) were prepared. Due to the moisture sensitivity, all the electrolytic materials were used in an argon-filled glove-box (H_2O and O_2 <1ppm). EC was heated to 80 ° C for three hours on the hot-plate (EC has crystal form in an aluminum bottle at room temperature), and subsequently transferred to the glove-box (Figure 21). Micropipette and precision balance were used in the glove-box to determine the amount of liquid from chemicals and salt, respectively.

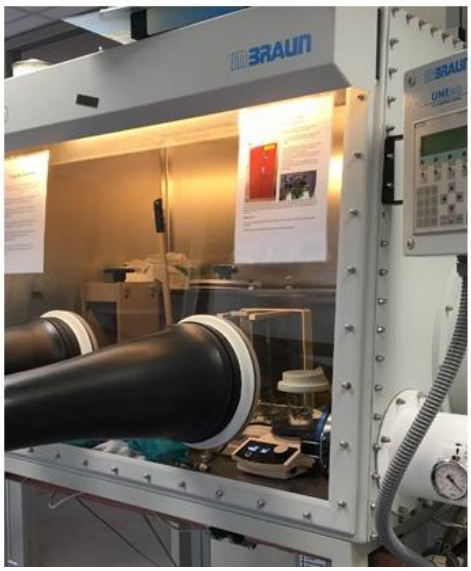

Figure 21. Electrolyte preparation in glove box.

First, the PC and EC were stirred for one hour at 400 rpm on a magnetic stirrer. Subsequently, $NaClO_4$ was added to this mixture and the stirring continued for two hours at 400 rpm to obtain the final form of the electrolyte.

2.3. Electrode Preparation

The working electrodes were prepared by spreading the slurry of the active materials (80 wt.%), carbon black (10 wt.%) and the polyvinylidene fluoride (PVDF) (10 wt.%) binder on the Al foil. The working electrodes were dried at 120 °C under vacuum over-night to remove the solvent (NMP) which is used to make slurry. Subsequently, the disks were cut at 10 mm in diameter from the working electrodes and transferred to an argon- filled glove box.

The CR2032 type coin cells were assembled using the sodium metal as anode, and the Whatman GF / D filter paper is used as membrane. The electrolyte is 1 M $NaClO_4$ salt dissolved in ethylene carbonate (EC)/ propylene carbonate (PC) (1: 1 w / w), and 300 µL electrolyte is used in each battery cell. All the assembling works were performed in an argon-filled glove box below 1 ppm H_2O and O_2 level.

2.4. Physical Characterization

2.4.1. XRD

X-ray diffraction is used to describe the formation of crystallization and phase formations in the materials. The diffraction pattern that occurs as a result of the interaction of X-rays with the atoms in the material provides information regarding the crystal structures of the materials.

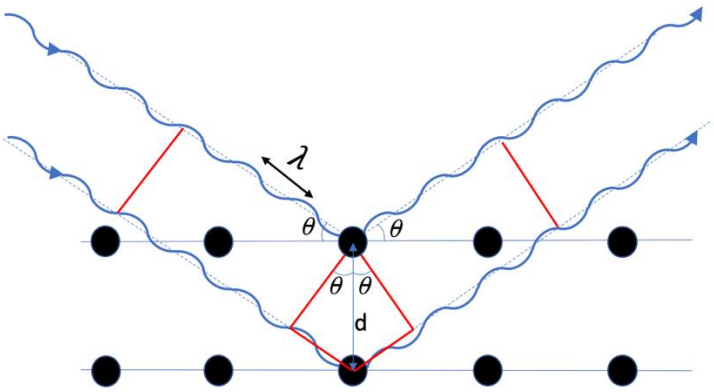

Figure 22. A schematic of Bragg diffraction.

As a result of the constructive interference of the x-rays that interact at the atoms, the Bragg law (eq. 7) is fulfilled and the diffraction pattern is obtained (Figure 22).

$$n\lambda = 2dsin\theta \quad (7)$$

where, λ is the wavelength, d, is the distance between the atomic planes, n is the order of the reflection (an integer) and the θ value is the angle between the incoming or reflected x-ray and the atomic plane. Since all the crystalline structures have their own specific d values, diffraction patterns can be used in the crystal structure determination.

2.4.1.1. Cu K-alpha XRD

The X-ray diffraction (XRD) experiments were carried out using the GNR brand EUROPE TT XRD model device at the DESY research center. (Figure 23). The data were collected using Cu K-alpha radiation from 10 to 80-degree 2θ values at 0.2-degree intervals for 15 seconds at each sampling point. The sample holder was rotated

at 30 rpm to increase the data count. The samples were ground in an agate mortar prior to the measurement to procure a fine powder.

Figure 23. Desktop XRD device at P61 beamline, DESY, Hamburg.

The crystal structure parameters were calculated by using the Rietveld method [146] with the FullProf software [147].

2.4.1.2. Synchrotron XRD

A synchrotron radiation source is the source of electromagnetic radiation generated by a storage ring. The electrons are usually accelerated to obtain radiation in these storage rings. Once the electron accelerated, they transmitted from the storage rings to the auxiliary components (such as the undulatory or wigglers). These auxiliary compounds allow the accelerated electrons to emit x-rays through their specially sorted magnets. The resulting x-rays are transmitted to the beamlines where the end-users can arrange the x-rays properties, such as energy and size, for specific experiments.

The most important difference between synchrotron radiation and laboratory radiation sources is brilliance. Brilliance is an important term used to describe the quality of x-ray and is defined as the number of photons per second per square millimeter of area per square milliradian of solid angle within a bandwidth of 0.1% of any given energy [148]. A synchrotron has a brilliance that is more than a billion times higher than a laboratory XRD (10^{19} for DESY). Other advantages of Synchrotron resources include; it has high energy that can penetrate deeper into the material (60 KeV for DESY).

Since the x-ray has a smaller wavelength, the bond length in the molecules and nanomaterials can be examined.

The synchrotron X-ray diffraction (XRD) experiments were carried out at the DESY research center in P02.1 beamline. In the experiments, a Perkin Elmer brand XRD 1624 detector was used to detect the diffraction data. The samples were ground and placed into Kapton tubes with a length of 4 cm and at a diameter of 0.2 mm (Figure 24). The Kapton tubes were rotated with a sample holder attached to a stepper motor to increase the data count, and a 60 s sampling time was used for each sample. The energy level was fixed at 60 keV by using the Laue type double-crystal monochromator (DCM, C (111) and Si (111) crystals) in the beam line.

Figure 24. A sample in the Kapton tube placed on the sample holder for the powder diffraction test.

2.4.2. Scanning Electron Microscopy (SEM)

The electron microscope is based on the principle of obtaining an image as a result of the reflection of the accelerated electron beam from the sample surface under high voltage.

The general method used for SEM measurements is as follows: the high energy electron beam generated by an electron gun is sent to the sample. Secondary electrons are formed as a result of the electron beam interaction with the sample, and these electrons are emitted by a special detector (Figure 25). Thus, an image created from these data and this image provide information pertaining to the surface topography.

SEM measurements were undertaken by the LEO brand EVO 40 XVP model under 30 kV acceleration voltage. This device has a 0.2–30 kV acceleration voltage range and a magnification of 7–1000000. The samples were kept under high vacuum to prevent the scattering of electrons from the particles in the air.

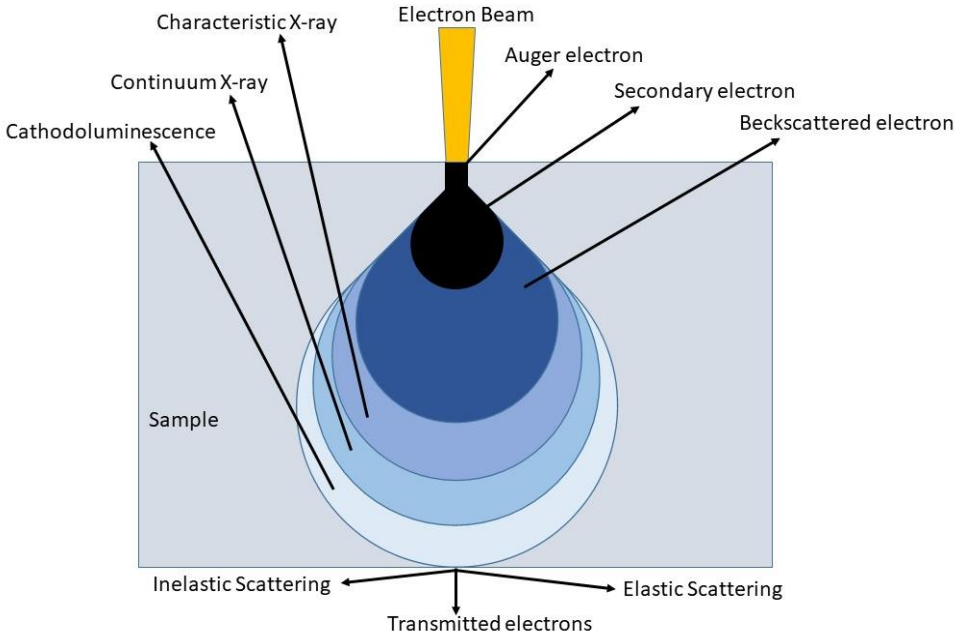

Figure 25. Signals emitted from interaction with electron beam sample [149].

2.4.3. Transmission Electron Microscopy (TEM)

In order to obtain TEM images, the electrons that pass through the sample instead of the electrons reflected from the sample are used unlike SEM measurement. The beam of electrons (typically 100–400 keV) from the electron gun is focused into a small, thin and coherent beam using the condenser lens. The beam strikes the sample and parts of it are transmitted depending upon the thickness and electron density of the sample. These transmitted electrons focus by the intermediate and objective lens as an image on a phosphor screen or charge coupled device (CCD) camera (Figure 26). The CCD camera usually transmits the image to a computer screen so that the image can be analyzed with various software. The image obtained in TEM is 2D and black and white in color. The sample color scale in the image is closer to black in thicker regions and closer to white in thin regions. Since TEM devices have a significantly higher resolution (usually used for samples smaller than 100-150 nm), they provide more accurate results in the analysis of samples in nano-size.

The energy of the electron beams used in the TEM measurements is 100-400 keV (approximately 1–0.3 nm) and these sizes are significantly smaller than the interatomic distance in the sample. The sample atoms thus act as a diffraction grating. In other words, some fraction of the beam will be scattered to specific angles, that are determined by the crystal structure of the sample, while others continue to pass through the sample without any deflection. Resultantly, the obtained diffraction patterns appear as a spot on the screen. Each spot is associated with the crystal structure of the sample that satisfies the diffraction conditions. This method is called selected area electron diffraction (SEAD). The nomenclature is prompted by the feature allowing the user to select any point on the sample by focusing. However, the diffraction patterns will also change as the sample will have different angles when tilted.

For TEM measurements, the powder samples produced in the study were dissolved in ethanol and placed on the copper grid sample holder. The diffraction patterns of the samples were also investigated by the SAED method. All TEM measurements were performed in the Microscopy department of Universitat Autonoma de Barcelona.

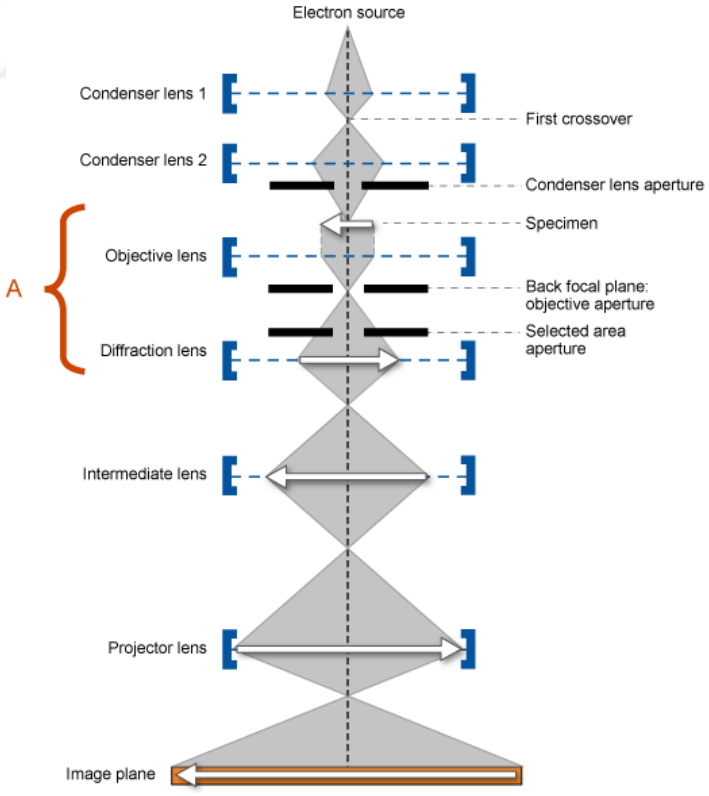

Figure 26. TEM device beam line [150].

2.4.4. Magnetization Analysis

Magnetic characterization can be measure with a PPMS system using VSM (vibrating sample magnetometer) attachment. The sample is placed in a magnetically homogeneous sample holder to minimize the residual magnetization that occurs from the holder. This magnetic homogeneous holder is mounted on a sample bar driven by a linear motor, which ensures vibration movement. A superconducting magnet is used to enclose the sample in homogeneous magnetic fields during measurement. Measurements are performed by the sinusoidal movement of the sample into a pickup coil. As a result of this movement, according to Faraday's law, samples induced a voltage whose value is detected by the system. The obtained data are converted to AC electrical signal to determine the magnetization curves of the sample. In order to gather an accurate signal, an oscillation amplitude with a peak of 1–3 mm and a frequency of 40 Hz is usually applied. A sensitivity to magnetization changes in the range of $<10^{-6}$ emu at a data rate of one Hz could be reached [151].

The magnetization-temperature (M-T) measurements of the samples were carried out by the VSM attachment of QUANTUM DESIGN PPMS device at the Inonu University Scientific and Technological Research Center (IBTAM). During the M-T measurements, 1000 Oe magnetic field was applied to the samples and the temperature was controlled between 5–300 K.

2.4.5. RAMAN

The Raman analysis is based on the measurement of the scattered beam from a certain angle by irradiating a sample with a strong laser source composed of monochromatic beams. As a result of this interaction, atoms either absorb the photons in the beam or scatter them. During the scattering, the frequency of a large part of the photons is equal to the frequency of the photons interacting with the substance and this is called elastic or Rayleigh scattering. However, the frequency of only a small portion of the scattered photons is different from the incident photons, and this is called inelastic or Raman scattering. Although Rayleigh scattering has a significantly higher intensity than Raman scattering, it creates a single peak in the spectrum and does not provide information about the bonding structures of the sample.

The link between Raman scattering and the characterization of molecules is as follows: the interaction molecules can rise to an upper energy level, in which case the frequency of the scattered photon decreases. Contrariwise, the molecules can go down to a lower energy level. In this case, the frequency of the scattered photons increases. The frequency decrease and increase in Raman scattering are called stokes and anti-stokes scattering, respectively (Figure 27). Since each energy transition is molecule-specific, data from the Raman spectroscopy provides important information regarding the atomic bonds within the sample.

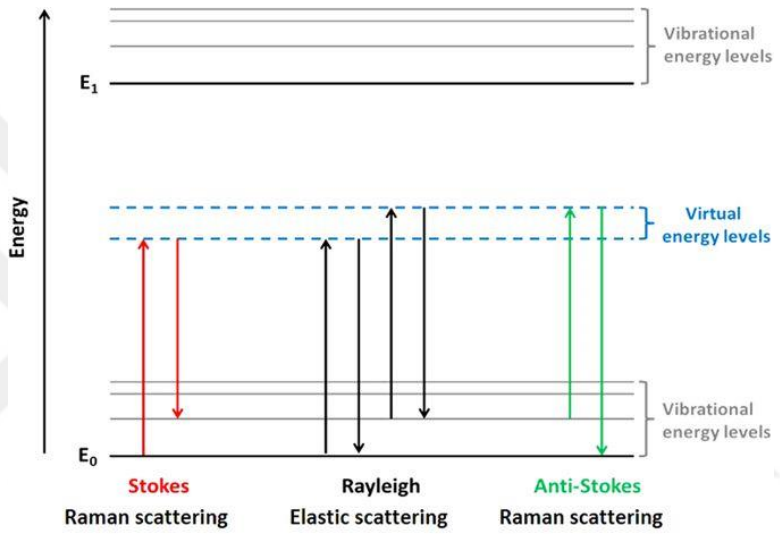

Figure 27. Energetic transitions involved in Raman scattering diagram [152].

In this work, Raman measurements were conducted with the RIGAKU brand Senterra model device using a 532 nm wavelength laser (20 mW laser power). All samples were examined with a 50 mm lens opening at 20x magnification and 3-6 cm^{-1} resolution at 60-2750 cm^{-1} wavelength. Experiments have been undertaken at the electrode form.

2.4.6. XAS

X-ray absorption spectroscopy (XAS) is a special measurement technique that can be used to obtain information regarding the environmental structure of an element in a crystal or molecule. In theory, when a sample is bombarded with precisely defined x-rays, some of these x-rays pass without affecting the sample (transmitted x-rays), some of these are scattered away from the core electrons (elastic/inelastic), while

some of the x-rays are absorbed by the atoms in the sample. If the core electrons absorb the x-rays, they either shift to higher-order orbitals (reaching an excited state) or are released from the atom by oscillation (continuum) (Figure 28); the first instance is known as x-ray absorption near-edge structure (XANES) and the second one as the extended x-ray absorption fine structure (EXAFS). The XANES spectra inform about the electronic structure and symmetry of the absorbing element while EXAFS spectra inform about the distance and numbers between the absorbing element and ligands [153].

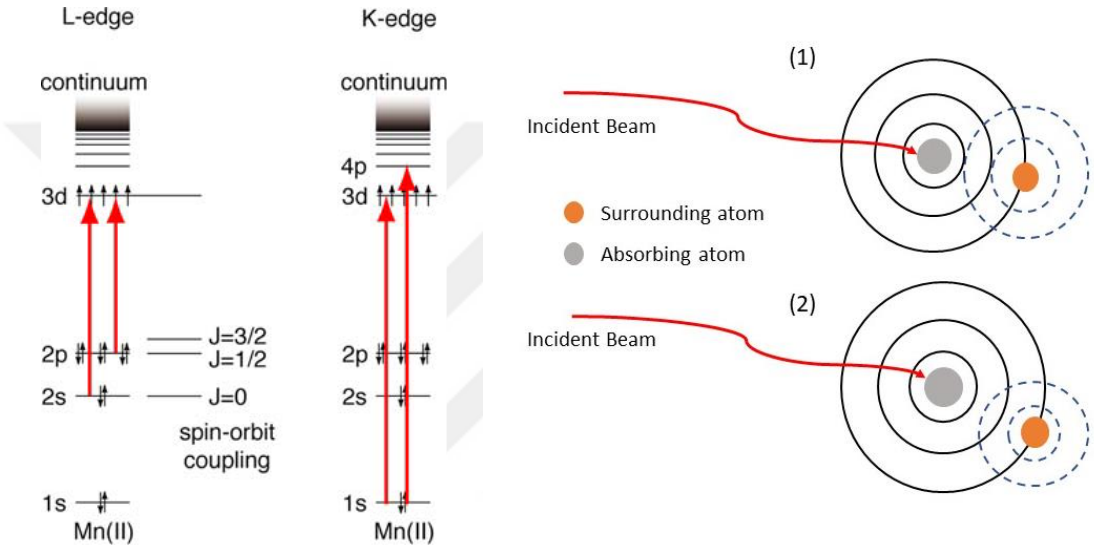

(a) (b)

Figure 28. (a) Energy level diagram for L-edge and K-edge for Mn (II) (energy levels are not in exact scale) [154]. (b) A schematic of the constructive and destructive interference in EXAFS. After interacting with the incident beam absorbing atom, photoelectrons emit in the waveform (black circles) and backscatter from the surrounding atoms (blue dashed circles). If the waves emitted from the surrounding atom and the waves emitted from the absorbing atom are in the same phase, a constructive interference occurs in the incident beam's energy value (1) and an increase in the XAS spectrum is observed. Conversely, if these two waves are in a different phase, destructive interference occurs (2) and the absorption in the spectrum decreases.

If the incident beam has enough energy to excite the electron a dramatic increase in the absorption coefficient is observed (Figure 29) due to emission the photons from the orbital electrons. This is called "EDGE". For example, in Figure 29, Mn K-edge peak can be observed at approximately 6530 eV. Currently, it is possible to access online K or L-edge energy values almost all of elements [155]. On the other hand, in the XAS spectrum, there is no sharp distinction between the XANES and EXAFS regions. It is generally accepted that energy value of 40–50 eV above the EDGE

energy is the boundary between the XANES and EXAFS regions. The lower and upper parts of this boundary are called XANES and EXAFS regions, respectively (Figure 29). The term, “Pre-edge” is used to define minor changes just before the sharp increase of the spectrum (Figure 29). Although these data do not seem useful, approaches have been made in some studies using the pre-edge data on ligand areas and spin states [156,157].

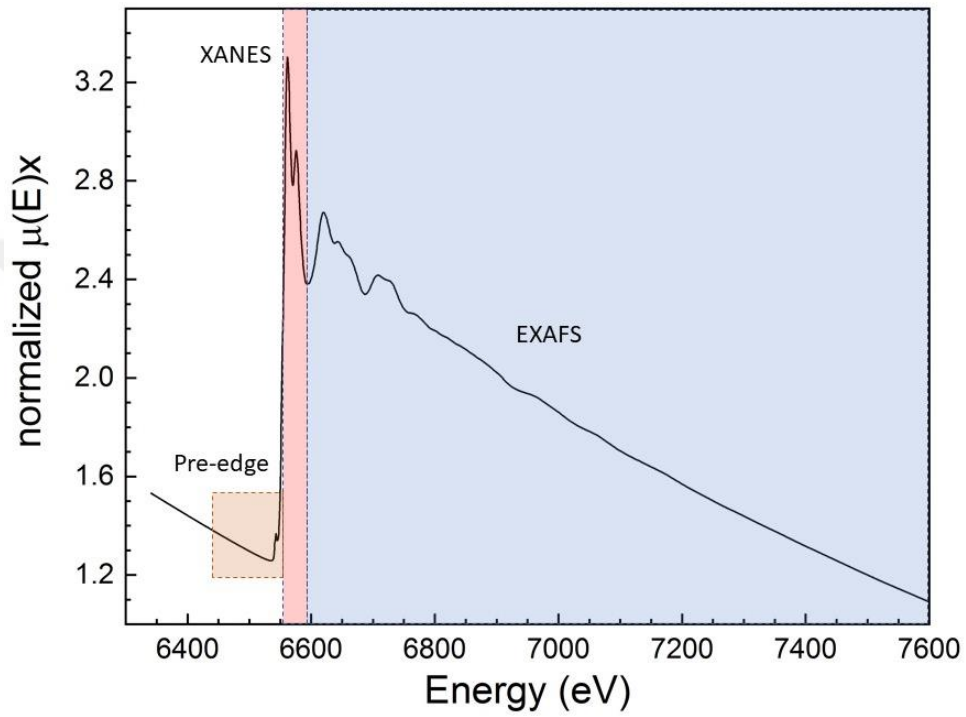

Figure 29 X-ray absorption spectrum of Mn K-edge from MnO_2. Redrawn from Kelly et al. [158].

The results of the sample and x-ray interaction can be seen in Figure 30.

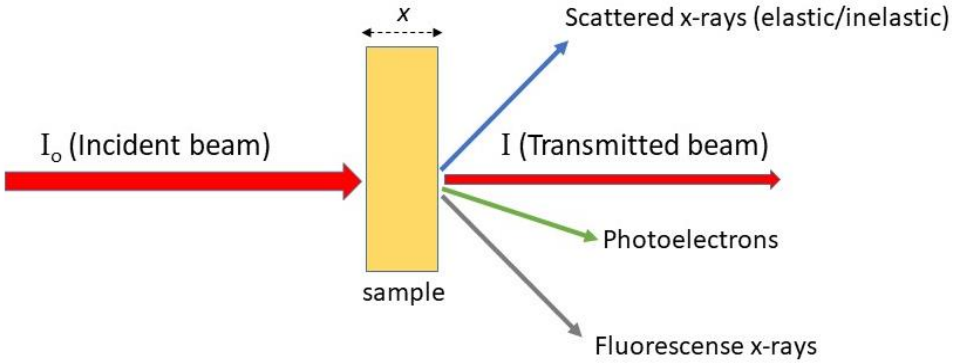

Figure 30. Interaction between x-ray and sample in XAS setup.

The relationship between the incident x-ray, I_0, and the transmitted x-ray, I, can be expressed as follows:

$$I = I_0 e^{-\mu x} \quad (8)$$

where μ is the linear absorption coefficient, and x, is the thickness of the sample. The incident and the transmitted x-ray can be measured with advanced devices and detectors in the synchrotron facilities. However, the key point to consider is the thickness of the sample.

There are different experimental techniques to measure the absorption coefficient. The x-ray intensity measured before interaction with the sample is compared with the intensity of the x-ray after interaction with the sample. The difference between these is due to the absorption, and this is called the Transmission mode. When x-ray is interacting with a sample, the core electron is excited and jumps to high-orbital and leaves a hole in its initial orbital. This hole can be filled by electrons from a higher orbital. When the electron passes to the lower level, it emits a photon. This photon intensity is compared with the x-ray intensity after interaction with the sample, and this is called the Fluorescence mode. The excited atom can emit a high-energy electron (Auger electron) to fall back to the ground state. In this case, all these emitted electrons can be counted and compared with the intensity of the transmitted x-ray, and this is called the Electron yield mode.

In this study, an XAS experiments were conducted at P-64 beam line of the DESY PETRA III, Germany. A fully tuned and cooled with liquid nitrogen double-crystal monochromator (DCM) equipped with a Si(111) crystal pair was used to select the energy of the incoming x-rays with an energy resolution ($\Delta E/E$) of approximately 1.4×10^{-4} (Figure 31). A total of four measurements were taken for each sample and their averages were used. Background subtraction and normalization of the XAFS data were performed by the ATHENA software [159].

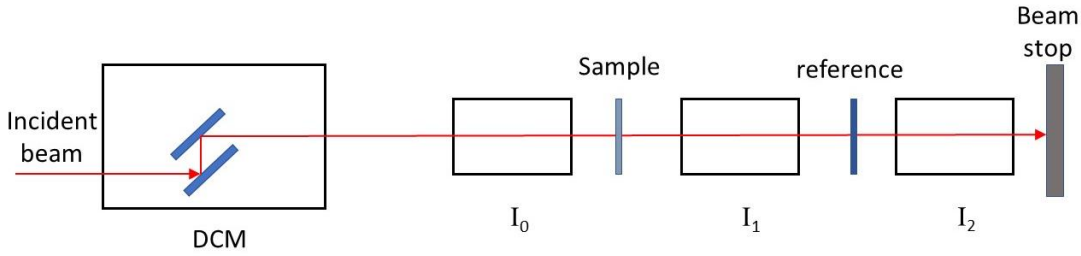

Figure 31. XAS experimental schematic at the P64 beam line. I_0, I_1 and I_2 are the ionization chambers that the measure the intensity of incident beam before and transmitted after the sample.

2.5. Electrochemical Characterization

2.5.1. Cyclic Voltammetry (CV)

CV is one of the most extensively used techniques to study the reduction and oxidation reactions in electrodes. The potential difference on the electrode is changed as a controlled variable and the resulting current values are measured as a result of the redox reactions. The potential difference starts from an initial potential (E_1) and is changed to a final potential at a specified scan rate (Figure 32 (a), "A" region). When the potential value reaches the point E_2, it returns to point E1 (Figure 32(a), "B" region) and this is called a cycle. While positive scanning is used to examine anodic (oxidation) reactions, negative scanning is used to study cathodic (reduction) reactions.

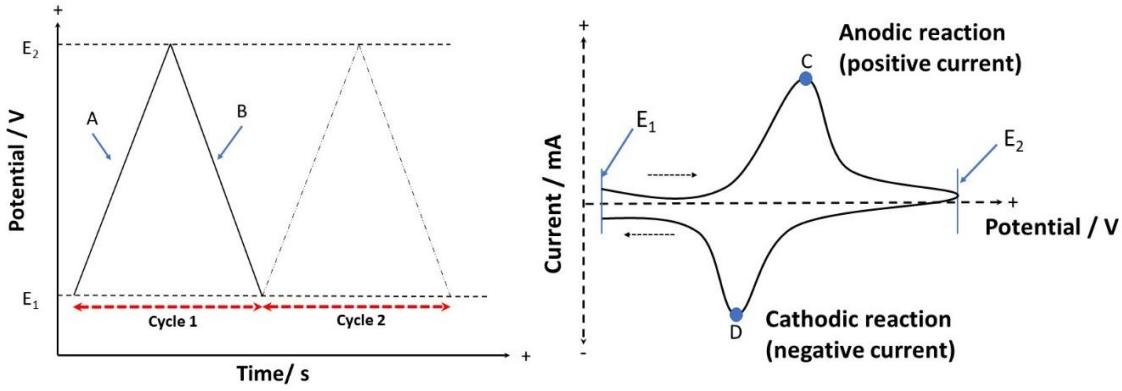

(a) (b)

Figure 32 (a) Voltage-time graph of potential used in CV measurements and (b) cathodic and anodic reaction (current) graph on electrodes at the specified voltage ranges.

In the graph shown in Figure 32 (b), CV measurement was initiated to measure anodic reactions. As the potential difference increases, an oxidation reaction occurs on the electrode surface. As a result of the ionic deposits on the surface, the diffusion at the electrode surface starts slowing down and reaches a peak at point "C." Since no diffusion occurs after this point, the oxidation reactions are terminated, and the measured current value starts to decrease. After the E_2 potential, the scan proceeds in the opposite direction; subsequently, oxidation reactions occur on the electrode and the current reaches the peak at "D." In reversible reactions shown in Fig. 32 (b), the number of reduction and oxidation reaction peaks is equal.

In this work, CV measurements were carried out at a 2–4 V potential range with 0.1 mV/s scan rate. BioLogic brand VMP3 model potentiostat was used for conducting the measurements.

2.5.2. Capacity Measurements

Capacity measurements were conducted with the constant current technique (Figure 33). While using this technique, the current values are denoted by the term "C-rate."

As shown in Figure 13, when the current C1 is applied to the battery cell, the battery is fully charged to the cut off voltage at the end of T1 time. When the negative C2 current is applied, similarly, the battery cell will be fully discharged to the cut off voltage when the time T2 is reached.

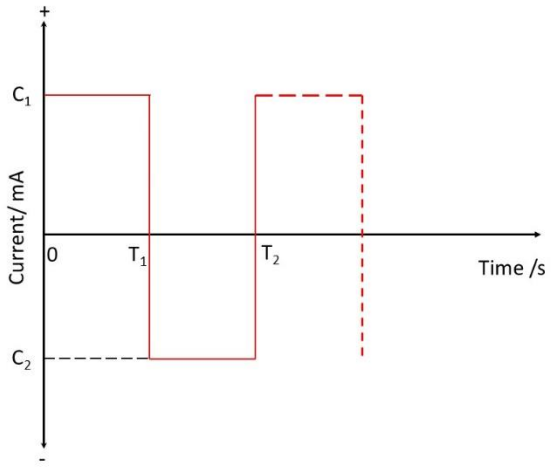

Figure 33. Constant current graph for charging (from 0 to T1) and discharging (from T1 to T2) a battery cell.

The charge and discharge measurements were carried out on an Iviumstat model Octostat brand potentiostat at 2.0–4.0 V voltage and C/3 current range (1C current rate corresponds to 121 mAh/g) under room temperature. The charge/discharge cycles were applied 100 times for all the samples and these measurements were undertaken twice.

3. RESULTS and DISCUSSION

3.1. X-ray Diffraction (XRD)

XRD analysis results were investigated to determine the crystal parameters after the phase comprising the production of $Na_{0.44}MnO_2$. Because Na loss occurred during the heat treatment, three different compounds were synthesized by adding 5% and 10% of the starting component of Na_2CO_3. The x-ray diffraction patterns of the three different compounds obtained as a result of the synthesis are shown in Figure 34. The results show that in the impurity phase, Mn_2O_3 was observed in the compounds with 0% and 5% Na_2CO_3 being added, whereas this impurity phase was not observed in the compound after the addition of 10% Na_2CO_3. All substitutions and analysis to be applied during this study were carried out on a 10% Na_2CO_3-supplemented sample that did not contain the impurity phase.

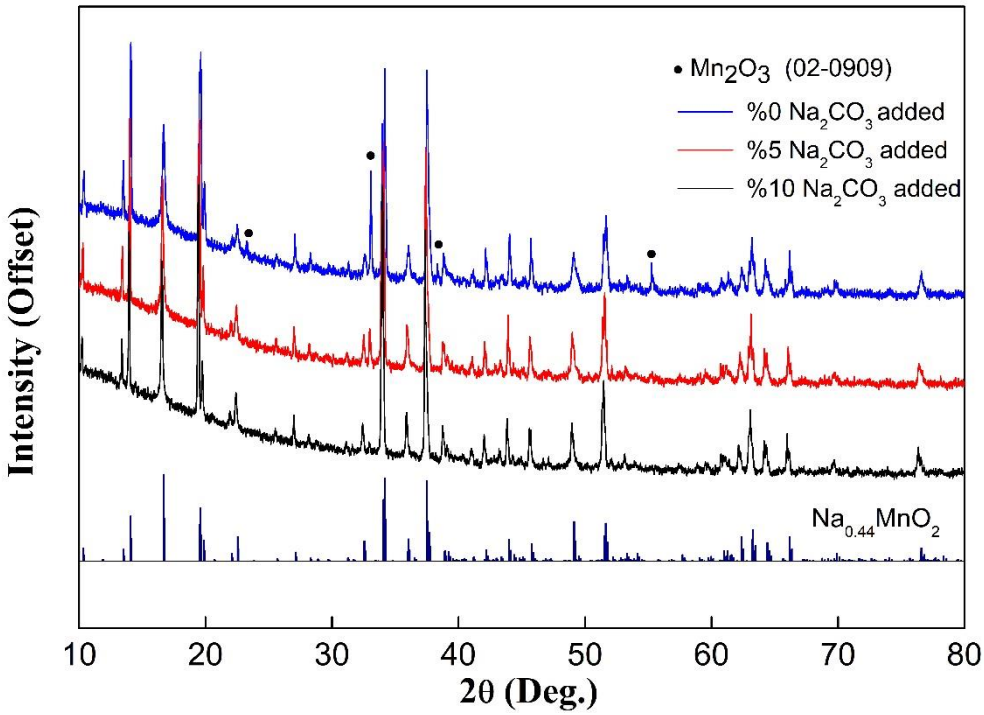

Figure 34. XRD patterns of the final compounds, obtained according to the amount of excess Na_2CO_3 that was added to prevent Na loss during the synthesis.

The Rietveld refinement method was used for the analysis of crystal parameters. The result of the calculation is shown in Figure 35.

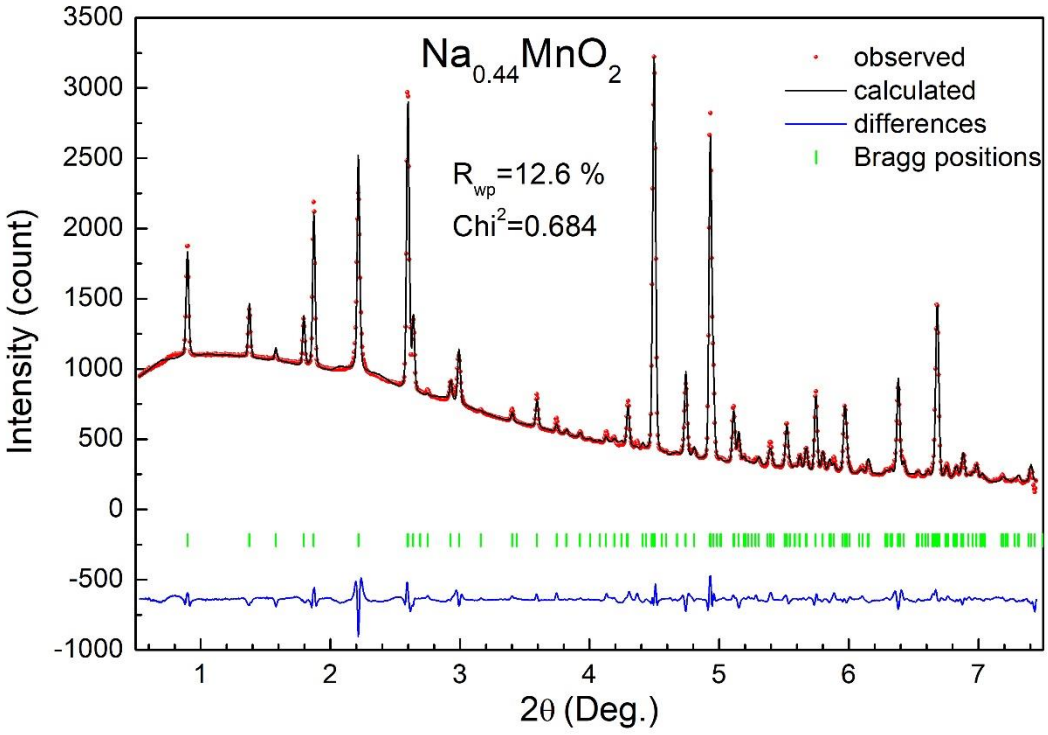

Figure 35. The Rietveld plot for refined $Na_{0.44}MnO_2$ synchrotron x-ray diffraction experimental data. The red dots, along with the black, the green and the blue lines correspond to the experimental data, calculated peaks by Rietveld method, the Bragg peak positions of $Na_{0.44}MnO_2$ and the differences between experimental and calculated data, respectively.

As a result of the calculation, it was determined that the crystal structure of the synthesized sample was suitable for the $Na_{0.44}MnO_2$ structure of the orthorhombic Pbam space group (PDF 02-0909), and the crystal parameters were determined as follows: a = 9.1072 Å (± 1.4E-4), b = 26.4003 Å (± 4.1E-4) and c = 2.8279 Å (± 4.1E-5) (Figure 36).

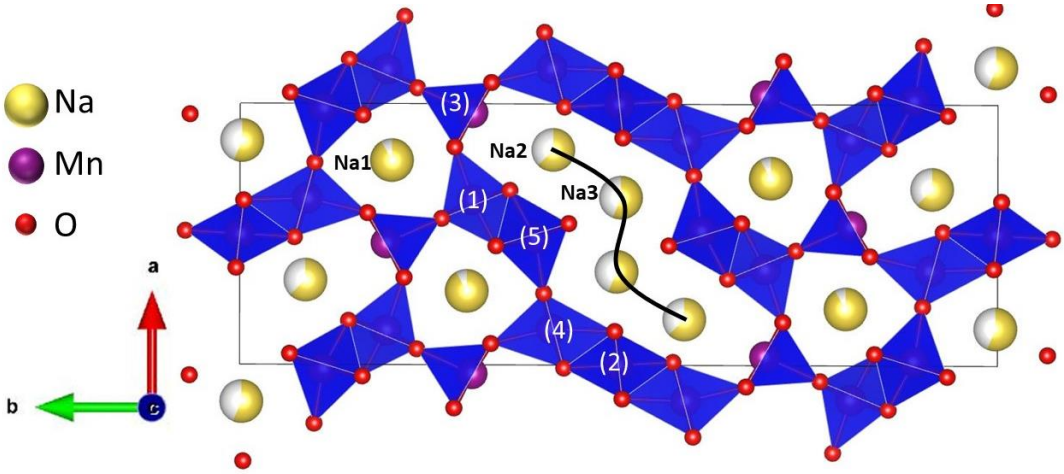

Figure 36. View of the $Na_{0.44}MnO_2$ crystal structure with five different Mn sites and three different Na sites along the C-axis. The structure was generated according to the Rietveld refinement calculation data.

As seen from Figure 36, there are five crystallographic sites for manganese, where the regions (1), (5), and (2) are occupied by Mn^{+4} while the (3) and (4) regions are occupied by Mn^{+3} [160]. The (1), (2), (4), and (5) sites follow the structure of the MnO_6 octahedral symmetry, while the (3) site has the square pyramid structure of MnO_5. During the insertion/extraction of Sodium, this MnO_5 square pyramid structure acts as a hinge and prevents the crystal structure's degradation due to stress [161]. On the other hand, there are three different sites for Sodium: Na2 and Na3 sites are located in large S-shaped tunnels, whereas the Na1 site is located in a smaller tunnel-like structure (Figure 36). The sodium in the Na1 region occupied this area completely, while the Na2 and Na3 regions occupied 2/3 and 1/3, respectively [162]. The Na2 and Na3 sites in the large S-shaped tunnel structure show reversible insertion/extraction, whereas for the Na1 site (especially in the range of 2–4 V) that is quite difficult [163].

The XRD patterns of the Co substituted samples are shown in Figure 37. It can be seen that there is an extra peak belonging to the P2-$Na_{0.7}MnO_{2.05}$ phase at about 16^0 (2θ) with x = 0.01 Co substitution. With the increase in the amount of cobalt substitution, the P2-$Na_{0.58}Mn_{0.5}Co_{0.5}O_2$ phase was formed and the structure completely transformed into $Na_{0.58}Mn_{0.5}Co_{0.5}O_2$ at x = 0.17 (Figure 38).

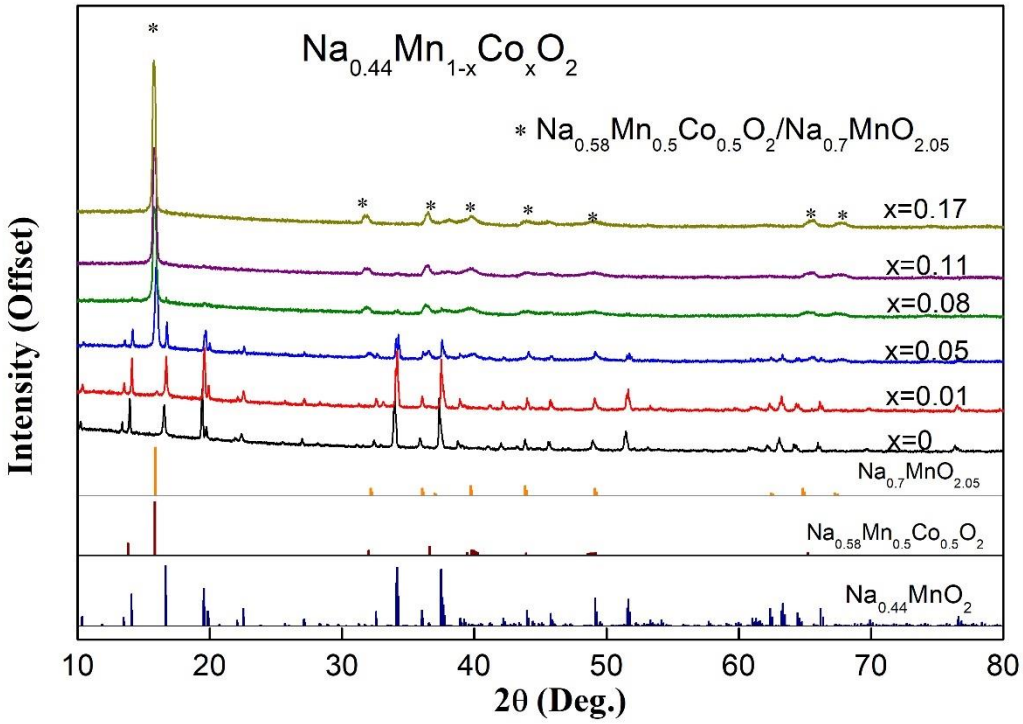

Figure 37. XRD pattern of $Na_{0.44}Mn_{1-x}Co_xO_2$ compounds arranged in the order of increasing cobalt content from bottom to top. The bottom standard patterns belong to the phases $Na_{0.44}MnO_2$ (ICSD-261314), $Na_{0.58}Mn_{0.5}Co_{0.5}O_2$ (ICSD 192730), and $Na_{0.7}MnO_{2.05}$ (PDF-27-0751).

The ratios of the phases in the structures and the crystal parameters calculated from the synchrotron XRD of $Na_{0.44}Mn_{1-x}Co_xO_2$ samples are shown in Table 1. In some compounds, low amount of Mn_2O_3 impurity phase has been detected, but this also was reported in previous works [125].

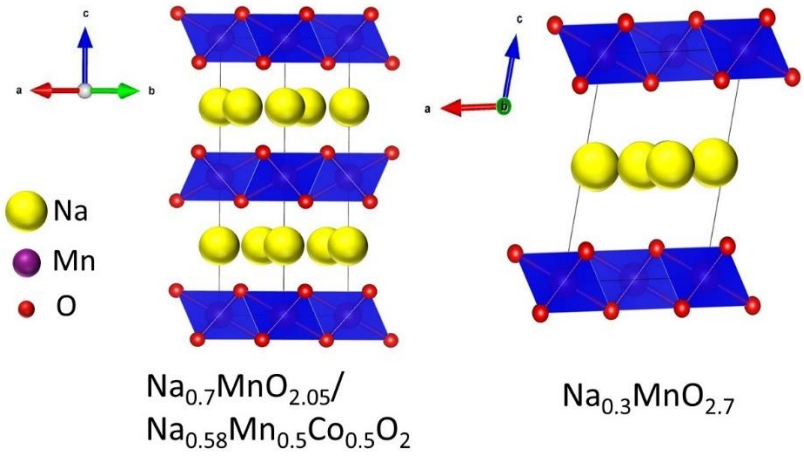

Figure 38. Crystal structure of $Na_{0.7}MnO_2$ (isostructural $Na_{0.58}Mn_{0.5}Co_{0.5}O_2$) and $Na_{0.3}MnO_{2.7}$.

According to the results, an x = 0 sample contains 100% $Na_{0.44}MnO_2$ phase, while an x = 0.01 sample contains 94% $Na_{0.44}MnO_2$ phase. On the other hand, with the increase of the Co substitution rate, the $Na_{0.7}MnO_{2.05}$ and $Na_{0.58}Mn_{0.5}Co_{0.5}O_2$ phases are found to become dominant in the sample x = 0.05. Moreover, a peak occurs at 17^0 (2θ), which belongs to $Na_{0.3}MnO_{2.7}$ (Figure 38).

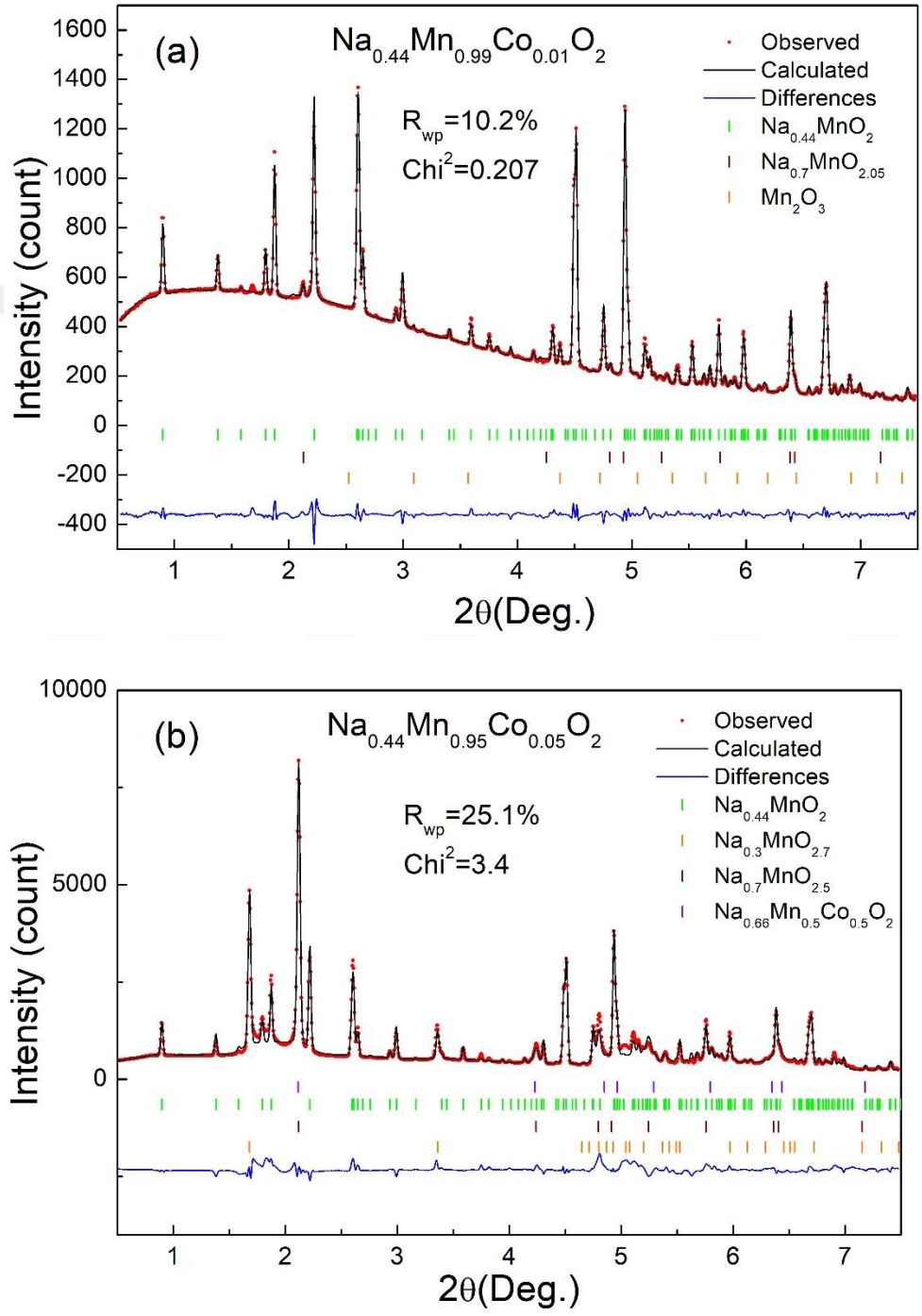

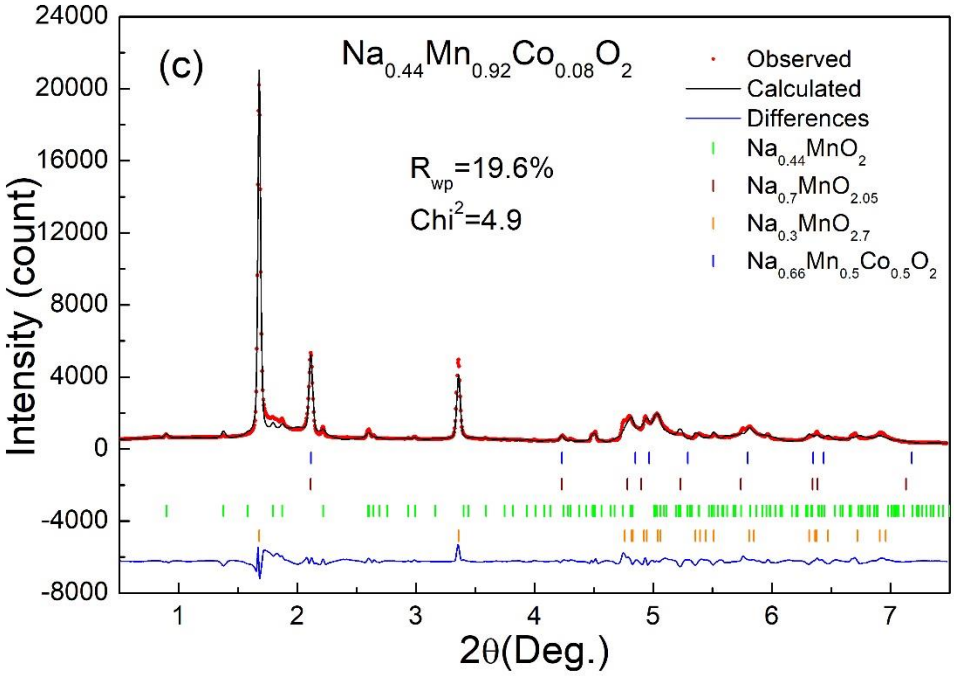
(c)
$Na_{0.44}Mn_{0.92}Co_{0.08}O_2$
R_{wp}=19.6%
Chi^2=4.9
Observed
Calculated
Differences
$Na_{0.44}MnO_2$
$Na_{0.7}MnO_{2.05}$
$Na_{0.3}MnO_{2.7}$
$Na_{0.66}Mn_{0.5}Co_{0.5}O_2$
Intensity (count)
2θ(Deg.)

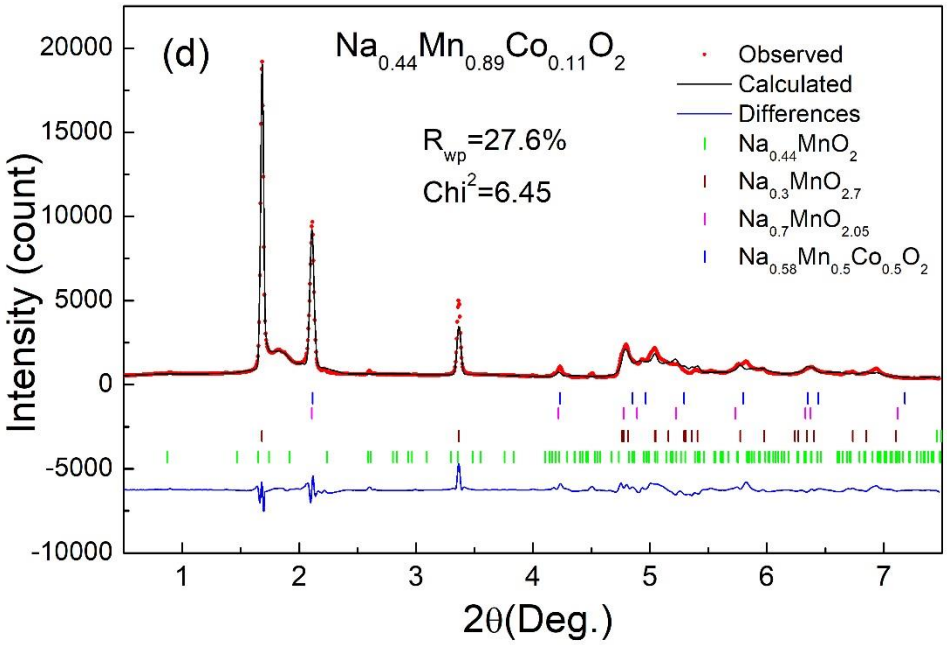
(d)
$Na_{0.44}Mn_{0.89}Co_{0.11}O_2$
R_{wp}=27.6%
Chi^2=6.45
Observed
Calculated
Differences
$Na_{0.44}MnO_2$
$Na_{0.3}MnO_{2.7}$
$Na_{0.7}MnO_{2.05}$
$Na_{0.58}Mn_{0.5}Co_{0.5}O_2$
Intensity (count)
2θ(Deg.)

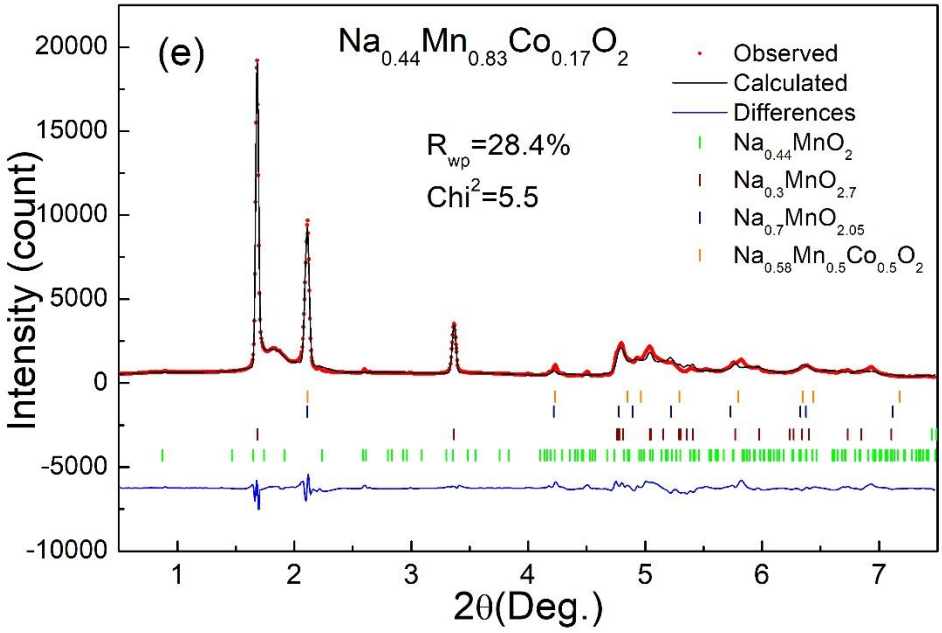

Figure 39. Synchrotron XRD Rietveld refinement plot of $Na_{0.44}Mn_{1-x}Co_xO_2$ samples. (a) x=0.01, (b) x=0.05, (c) x=0.08, (d) x=0.11, (e) x=0.17.

The unit cell volume of $Na_{0.44}MnO_2$ decreases with the increase of the Co substitution ratio, as observed in Table 1.

Table 1. Phase rates and crystal parameters of $Na_{0.44}Mn_{1-x}Co_xO_2$ compounds obtained from synchrotron XRD refinement results.

Sample	Phases	$Na_{0.44}MnO_2$	
		Lattice Parameters (Å)	**Volume (Å^3)**
x=0	%100 $Na_{0.44}MnO_2$	a=9.1321 (±5.4E-4) b=26.4474 (±1.6E-3) c=2.8339 (±1.1E-4)	684.47 (±0.064)
x=0.01	%97.84 $Na_{0.44}MnO_2$ %3.86 $Na_{0.7}MnO_{2.05}$ %1.3 Mn_2O_3	a=9.1017 (±3E-4) b=26.4417 (±8.3E-4) c=2.8286 (±4.4E-5)	680.736 (±0.064)
x=0.05	%68.8 $Na_{0.44}MnO_2$ %25.4 $Na_{0.7}MnO_{2.05}$ %1.1 $Na_{0.58}Mn_{0.5}Co_{0.5}O_2$ %4.7 $Na_{0.3}MnO_{2.7}$	a=9.0868 (±8.7E-4) b=26.3951 (±2.8E-3) c=2.8259 (±2.6E-4)	680.102 (±0.064)
x=0.08	%14.2 $Na_{0.44}MnO_2$ %34.9 $Na_{0.7}MnO_{2.05}$ %3.7 $Na_{0.58}Mn_{0.5}Co_{0.5}O_2$ %47.2 $Na_{0.3}MnO_{2.7}$	a=9.1194 (±4.8E-3) b=26.459 (±1.6E-2) c=2.7742 (±1.0E-3)	679.29 (±0.722)
x=0.11	%3.1 $Na_{0.44}MnO_2$ %25.4 $Na_{0.7}MnO_{2.05}$ %20.5 $Na_{0.58}Mn_{0.5}Co_{0.5}O_2$ %51 $Na_{0.3}MnO_{2.7}$	a=9.200(±5.9E-3) b=26.3658(±1.1E-2) c=2.6474(±2.8E-3)	675.44 (±0.722)
x=0.17	%1.2 $Na_{0.44}MnO_2$ %11.4 $Na_{0.7}MnO_{2.05}$ %19.2 $Na_{0.58}Mn_{0.5}Co_{0.5}O_2$ %68.2 $Na_{0.3}MnO_{2.7}$	a=9.1291 (±3.8E-3) b=26.9781 (±5.2E-3) c=2.6817 (±9.4E-4)	675.55 (±0.722)

The XRD diffraction patterns of the $Na_{0.44}Mn_{1-x}Ni_xO_2$ series are shown in Figure 40. In the x = 0.01 cobalt substitution diffraction pattern, the characteristic (002) peak of the P2 phase becomes visible at 16^0 (2θ). The phases, ratios, and crystal parameters

from synchrotron XRD refinement calculation (Figure 41) of all the samples are given in Table 2. According to Table 2, the samples of x = 0.01 and x = 0.05 had an almost identical phase reaction (about 73.5%) compared to the $Na_{0.44}MnO_2$ phase. On the other hand, the $Na_{0.7}MnO_2$ phase was observed as the dominant phase in all other high-substituted samples. In addition, Table 2 shows that the $Na_{0.44}MnO_2$ unit cell volume decreases with increasing Ni substitution.

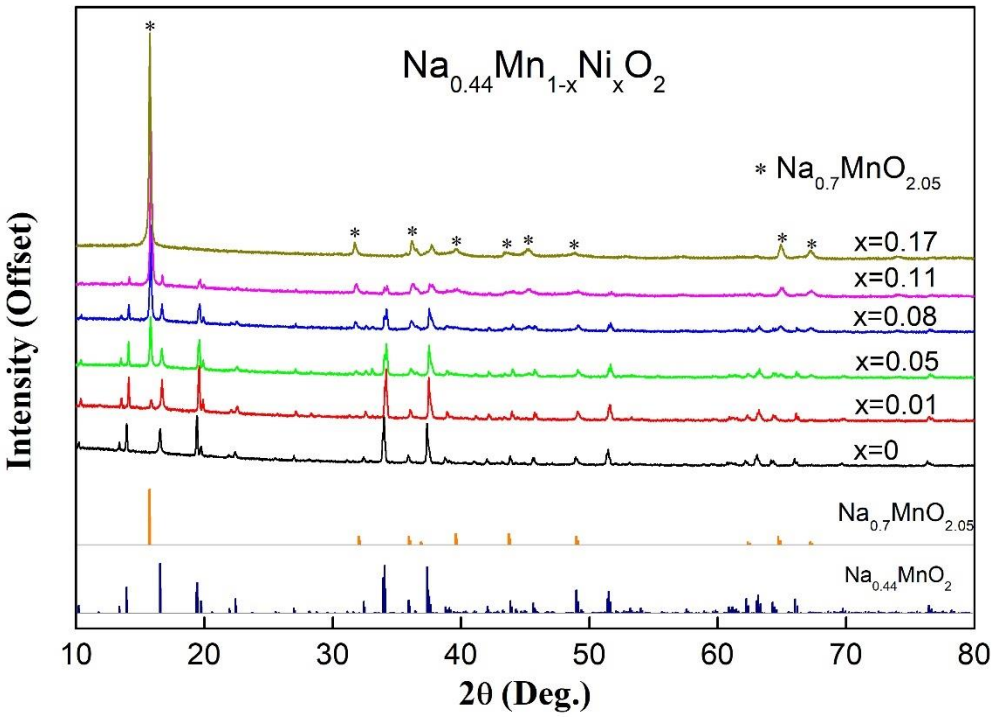

Figure 40. XRD pattern of $Na_{0.44}Mn_{1-x}Ni_xO_2$ compounds arranged in the order of increasing cobalt content from bottom to top. The bottom standard patterns belong to the phases of $Na_{0.44}MnO_2$ (ICSD-261314) and $Na_{0.7}MnO_{2.05}$ (PDF-27-0751).

Unlike the cobalt samples, the x = 0.05 and x = 0.08 nickel-substituted samples have a higher proportion of $Na_{0.44}MnO_2$. In this case, it can be said that Ni substitution causes less degradation of the sample structure.

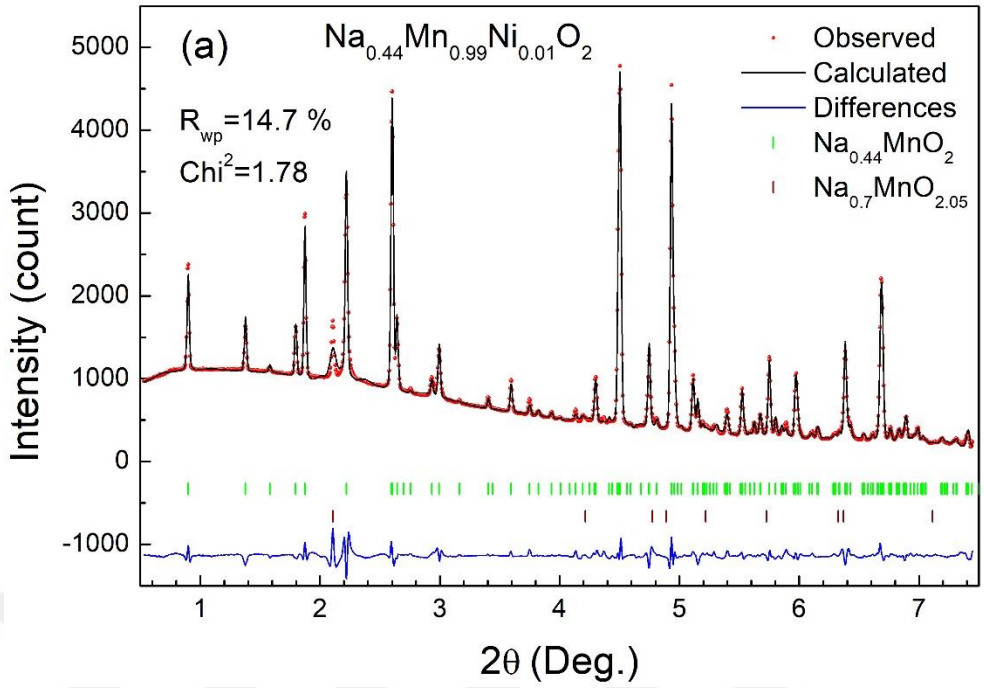
(a)
$Na_{0.44}Mn_{0.99}Ni_{0.01}O_2$
R_{wp}=14.7 %
Chi^2=1.78
Observed
Calculated
Differences
$Na_{0.44}MnO_2$
$Na_{0.7}MnO_{2.05}$
Intensity (count)
2θ (Deg.)

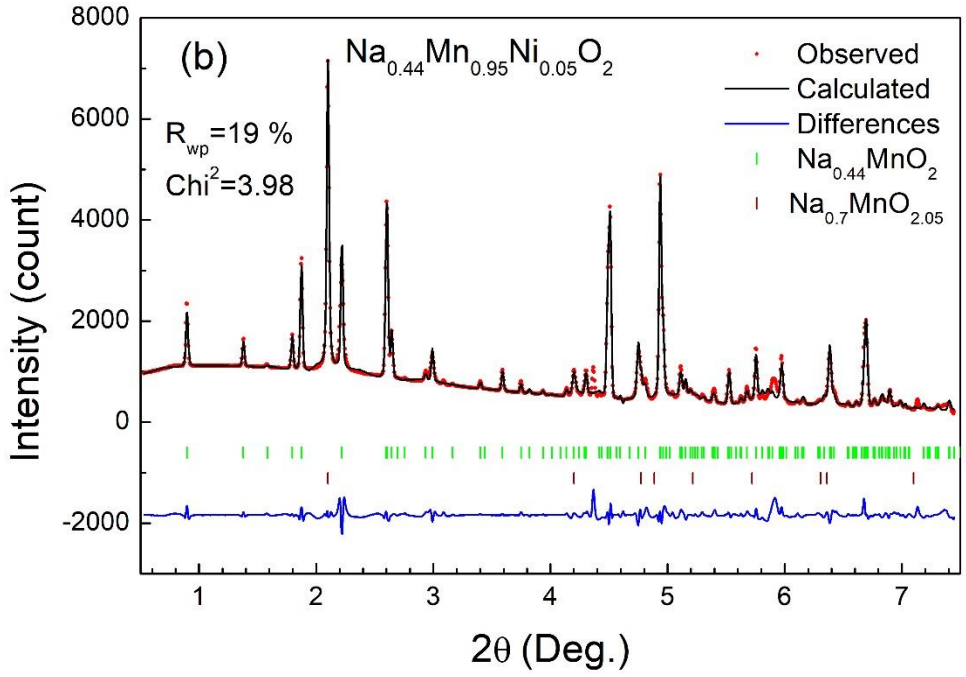
(b)
$Na_{0.44}Mn_{0.95}Ni_{0.05}O_2$
R_{wp}=19 %
Chi^2=3.98
Observed
Calculated
Differences
$Na_{0.44}MnO_2$
$Na_{0.7}MnO_{2.05}$
Intensity (count)
2θ (Deg.)

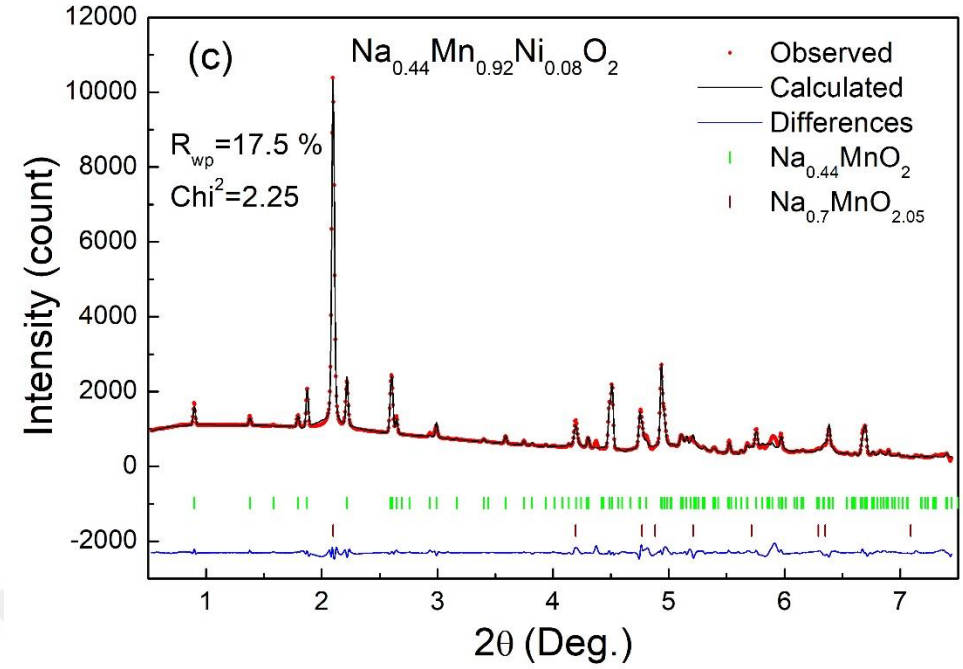
(c)
$Na_{0.44}Mn_{0.92}Ni_{0.08}O_2$
R_{wp}=17.5 %
Chi^2=2.25
Observed
Calculated
Differences
$Na_{0.44}MnO_2$
$Na_{0.7}MnO_{2.05}$
Intensity (count)
2θ (Deg.)

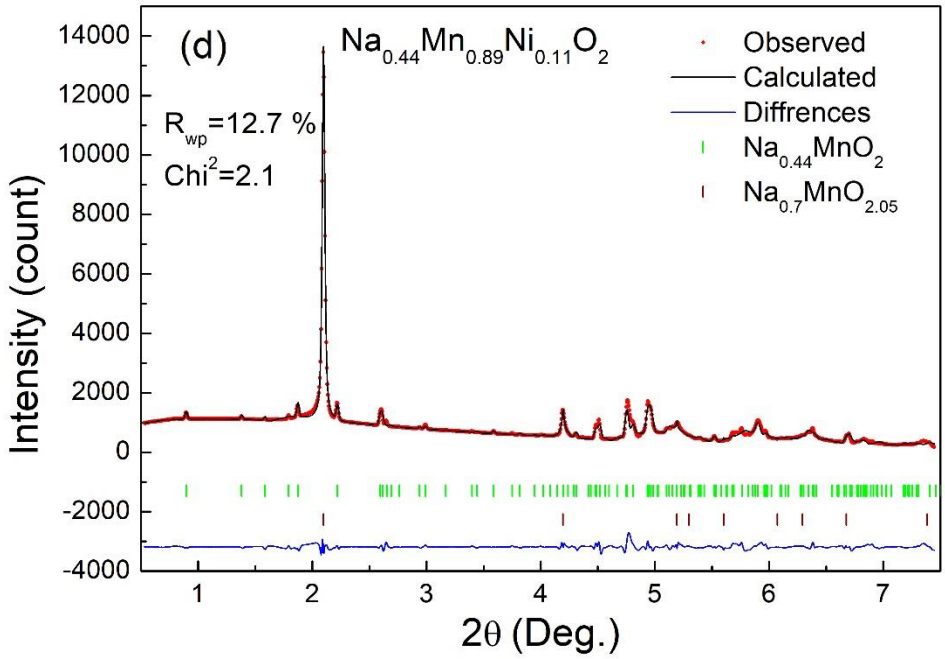
(d)
$Na_{0.44}Mn_{0.89}Ni_{0.11}O_2$
R_{wp}=12.7 %
Chi^2=2.1
Observed
Calculated
Diffrences
$Na_{0.44}MnO_2$
$Na_{0.7}MnO_{2.05}$
Intensity (count)
2θ (Deg.)

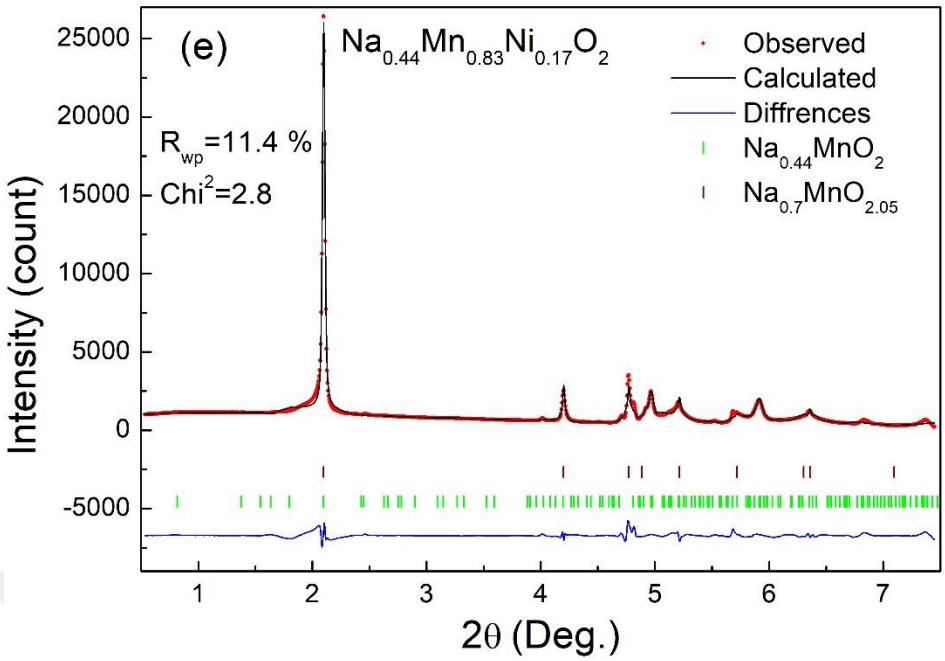

Figure 41. Synchrotron XRD Rietveld refinement plot of $Na_{0.44}Mn_{1-x}Ni_xO_2$ samples. (a) x=0.01, (b) x=0.05, (c) x=0.08, (d) x=0.11, (e) x=0.17.

Co and Ni substitution were mostly effective on Mn (4) sites occupied by Mn^{+3}. The most important reason behind this finding is that these sites have an octahedral symmetry, which is higher than the triangular square pyramid structure. Furthermore, Mn^{+3} and Mn^{+4} ions exist in $Na_{0.44}MnO_2$ to provide the charge balance, and the ionic radius of Mn^{+3} and Mn^{+4} is 0.58 Å and 0.53 Å, respectively. However, the ionic radius of Co^{+3} and Ni^{+3} is 0.54 Å and 0.56 Å, respectively, and thus when Co or Ni is substituted with Mn, these ions are likely to prefer Mn^{+3} sites as they have smaller ionic radius than Mn^{+3} [164]. This also explains the shrinkage in the unit cell seen in Tables 1 and 2. On the other hand, the substitution of Mn (3) sites prevents the JT effect on Mn^{+3} [161].

Table 2. Phase rates and crystal parameters of $Na_{0.44}Mn_{1-x}Ni_xO_2$ compounds obtained from refinement results.

Sample	Phases	$Na_{0.44}MnO_2$	
		Lattice Parameters (Å)	**Volume (Å³)**
x=0	%100 $Na_{0.44}MnO_2$	a=9.1321 (±5.4E-4) b=26.4474 (±1.6E-3) c=2.8339 (±1.1E-4)	684.47 (±0.064)
x=0.01	%73.57 $Na_{0.44}MnO_2$ %26.43 $Na_{0.7}MnO_{2.05}$	a=9.1234 (±4.3E-4) b=26.4356(±1.3E-3) c=2.8332 (±9.8E-4)	683.326 (±0.052)
x=0.05	%73.54 $Na_{0.44}MnO_2$ %26.46 $Na_{0.7}MnO_{2.05}$	a=9.1136 (±2.5E-4) b=26.4606 (±7.5E-4) c=2.8309 (±8.8E-5)	682.687 (±0.096)
x=0.08	%35.83 $Na_{0.44}MnO_2$ %64.17 $Na_{0.7}MnO_{2.05}$	a=9.1112 (±8.4E-4) b=26.4814 (±2.8E-3) c=2.8304 (±2.1E-4)	682.931 (±0.109)
x=0.11	%14.1 $Na_{0.44}MnO_2$ %85.9 $Na_{0.7}MnO_{2.05}$	a=9.0874 (±1.9E-3) b=26.5010 (±6.7E-3) c=2.8295 (±5.2E-4)	681.42 (±0.258)
x=0.17	%23.17 $Na_{0.44}MnO_2$ %76.83 $Na_{0.7}MnO_{2.05}$	a=9.039 (±2.3E-3) b=25.7768 (±5.8E-3) c=2.825 (±5.6E-4)	672.153 (±0.522)

3.2. RAMAN Analysis

The structural characterization of $Na_{0.44}Mn_{1-x}Co_xO_2$ and $Na_{0.44}Mn_{1-x}Ni_xO_2$ samples was continued using Raman spectroscopy. The samples were analyzed in electrode form, and thus, peaks of carbon bonds are seen in the Raman spectra (Figures 42 and 43).

The Raman spectrum of $Na_{0.44}Mn_{1-x}Co_xO_2$ samples ($0 \leq x \leq 0.17$) can be seen in Figure 42. The band at 638 cm^{-1} in the spectrum indicate Mn-O, the symmetric

stretching of MnO_6 octahedra (A1g mode), while the band at 342 cm^{-1} represents O-Mn-O and Na-O bending [165]. With the substitution of Co, the bands at 275 cm^{-1} and 537 cm^{-1} were observed from the x = 0.01 sample. The band at 537 cm^{-1} belongs to Mn-O stretching in the MnO_6 octahedra; this band comes from both the starting sample $Na_{0.44}MnO_2$ and the $Na_{0.7}MnO_2$, $Na_{0.58}Mn_{0.5}Co_{0.5}O_2$, and $Na_{0.3}MnO_{2.7}$ samples formed using Co substitution [166]. The observation that the band at 537 cm^{-1} increases with Co substitution is consistent with the result where the $Na_{0.7}MnO_2$, $Na_{0.58}Mn_{0.5}Co_{0.5}O_2$, and $Na_{0.3}MnO_{2.7}$ phases becomes dominant with Co substitution, as mentioned in the XRD analysis. On the other hand, the Co-O bands have been reported between 537 cm^{-1} and 638 cm^{-1} in previous studies [167], and one reason for the peak broadening observed in this range (Figure 42) might be the effect of overlapping Co-O and Mn-O bands. The bands observed at the wavelengths of 1352 cm^{-1} and 1593 cm^{-1} in the spectrum are D and G bands, respectively, formed by the carbon used in the electrode [168].

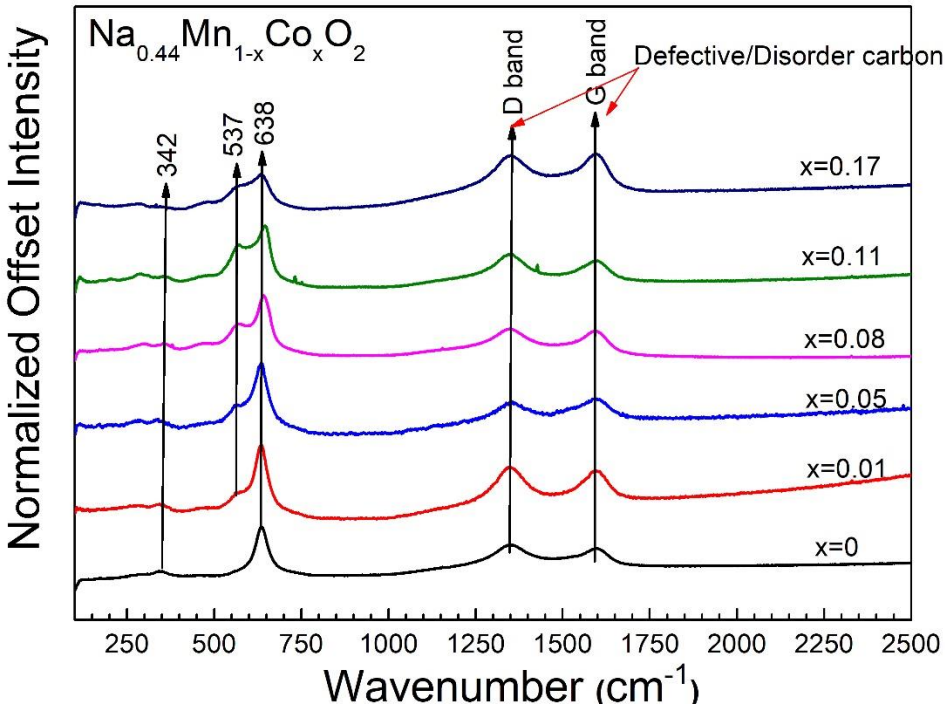

Figure 42. Raman spectrum of $Na_{0.44}Mn_{1-x}Co_xO_2$ samples as cathode form.

Figure 43 shows the Raman spectrum of $Na_{0.44}Mn_{1-x}Ni_xO_2$ ($0 \leq x \leq 0.17$) samples. The band at 632 cm^{-1} in the spectrum indicates Mn-O, the symmetric stretching of MnO_6 octahedra (A1g mode), while the band at 340 cm^{-1} represents O-Mn-O and Na-O bending [165]. With the nickel substitution, starting from x = 0.01 sample, 480 cm^{-1}

and 571 cm^{-1} bands were observed. The band at 480 cm^{-1} is reported as the point that consist of the first-order transverse optical (TO) and longitudinal optical (LO) phonon modes of Ni-O, respectively [169]. The band at 571 cm^{-1} belongs to Mn-O stretching in MnO_6 octahedra, and this band comes from both the starting sample $Na_{0.44}MnO2$ and the $Na_{0.7}MnO_2$ samples that were formed with Ni substitution [166]. The bands observed at the wavelengths of 1352 cm^{-1} and 1593 cm^{-1} in the spectrum are the D and G bands, respectively, formed by the carbon used in the electrode, similar to the $Na_{0.44}Mn_{1-x}Co_xO_2$ samples [170].

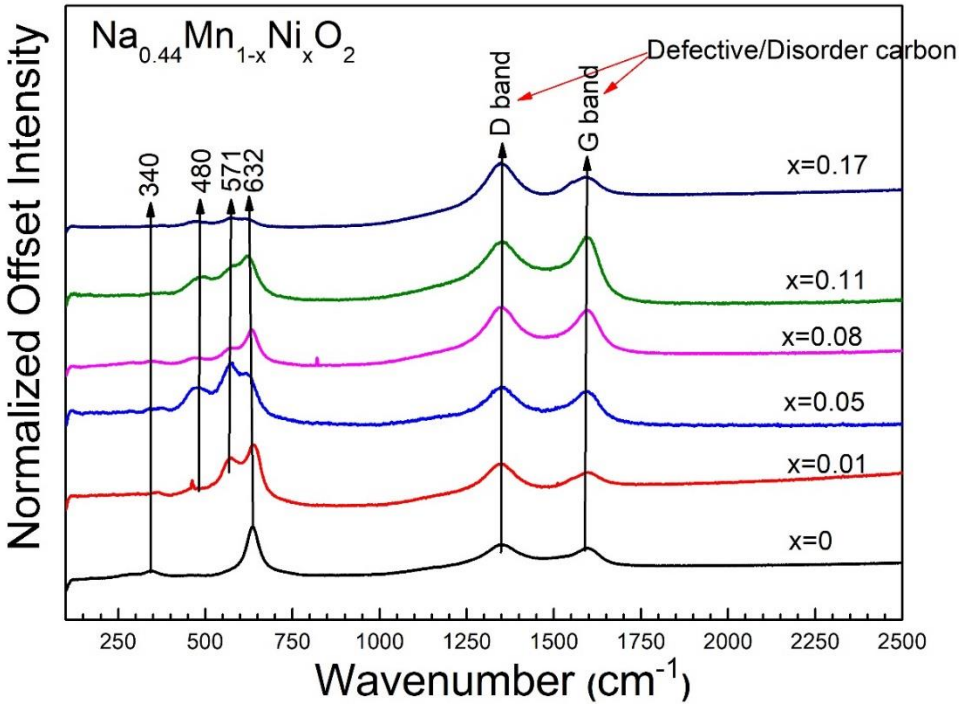

Figure 43. Raman spectrum of $Na_{0.44}Mn_{1-x}Ni_xO_2$ samples as the cathode form.

3.3. Surface Morphologies

3.3.1. SEM Analysis

The surface morphology of the synthesized $Na_{0.44}Mn_{1-x}Ni_xO_2$ powder samples prepared by the solid-phase reaction are shown in Figure 44 with various magnifications. In Figure 44 (a)-(d), it can be seen that x = 0 and x = 0.01 samples are in nanorod form. The average widths of the nanorods are 540 nm and 702 nm for samples x = 0 and x = 0.01, respectively. With the increasing rate of cobalt

substitution, $Na_{0.7}MnO_2$ phase with a granular structure is formed in the samples (Figure 44 (e)-(m)). The average width of the nanorods is 944 nm, 1056 nm, and 2166 nm for samples x = 0.05, x = 0.08, and x=0.11, respectively. According to the results of the observed surface morphology, the nanorods were thickened by Co substitution in the Mn sites. Additionally, the granular structure increased with Co substitution, and consequently the nanorod form was not observed in the x = 0.17 sample. This observation is consistent with the assertion that $Na_{0.44}MnO_2$ peaks are not observed in the XRD analysis of the x = 0.17 sample.

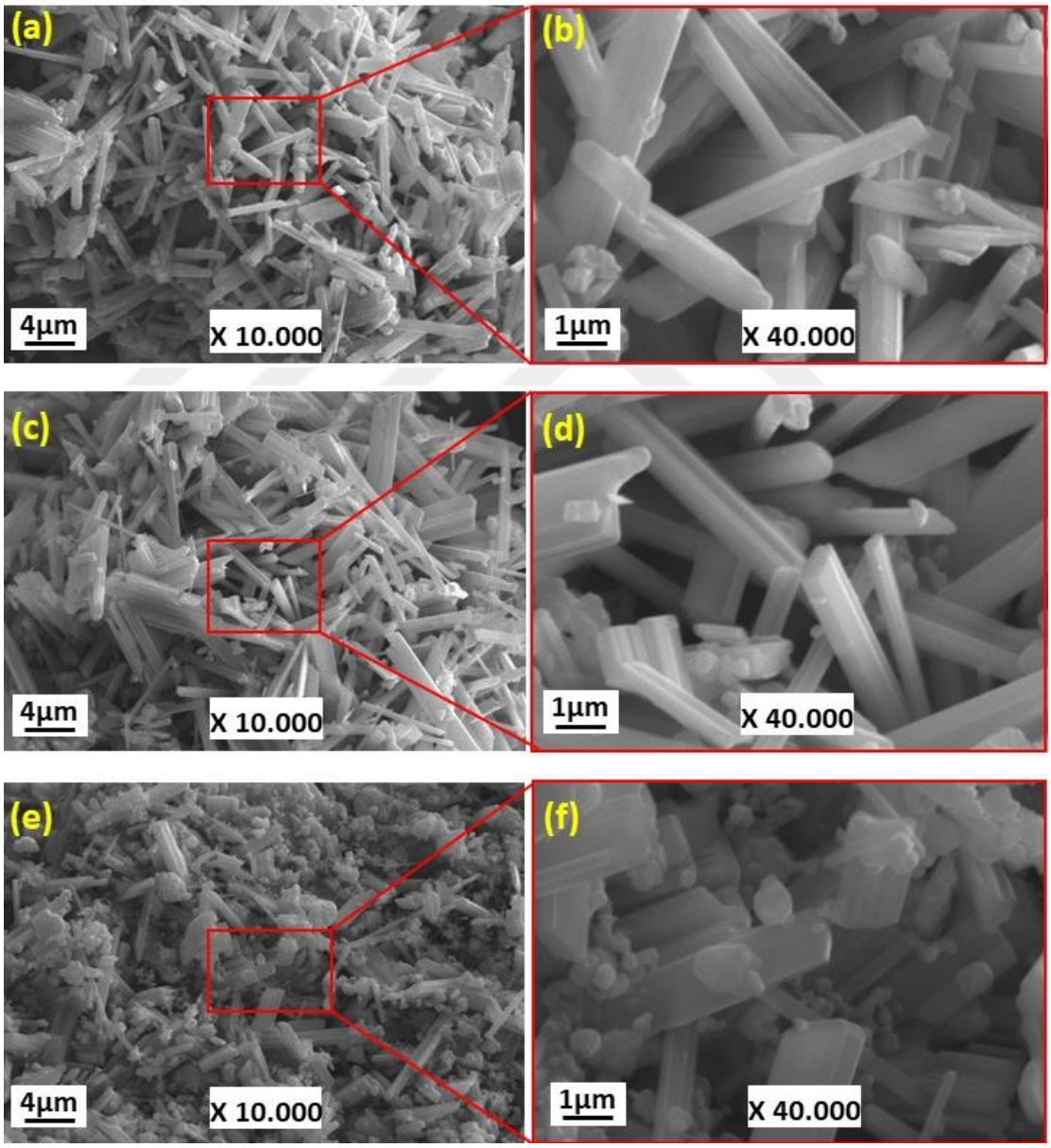

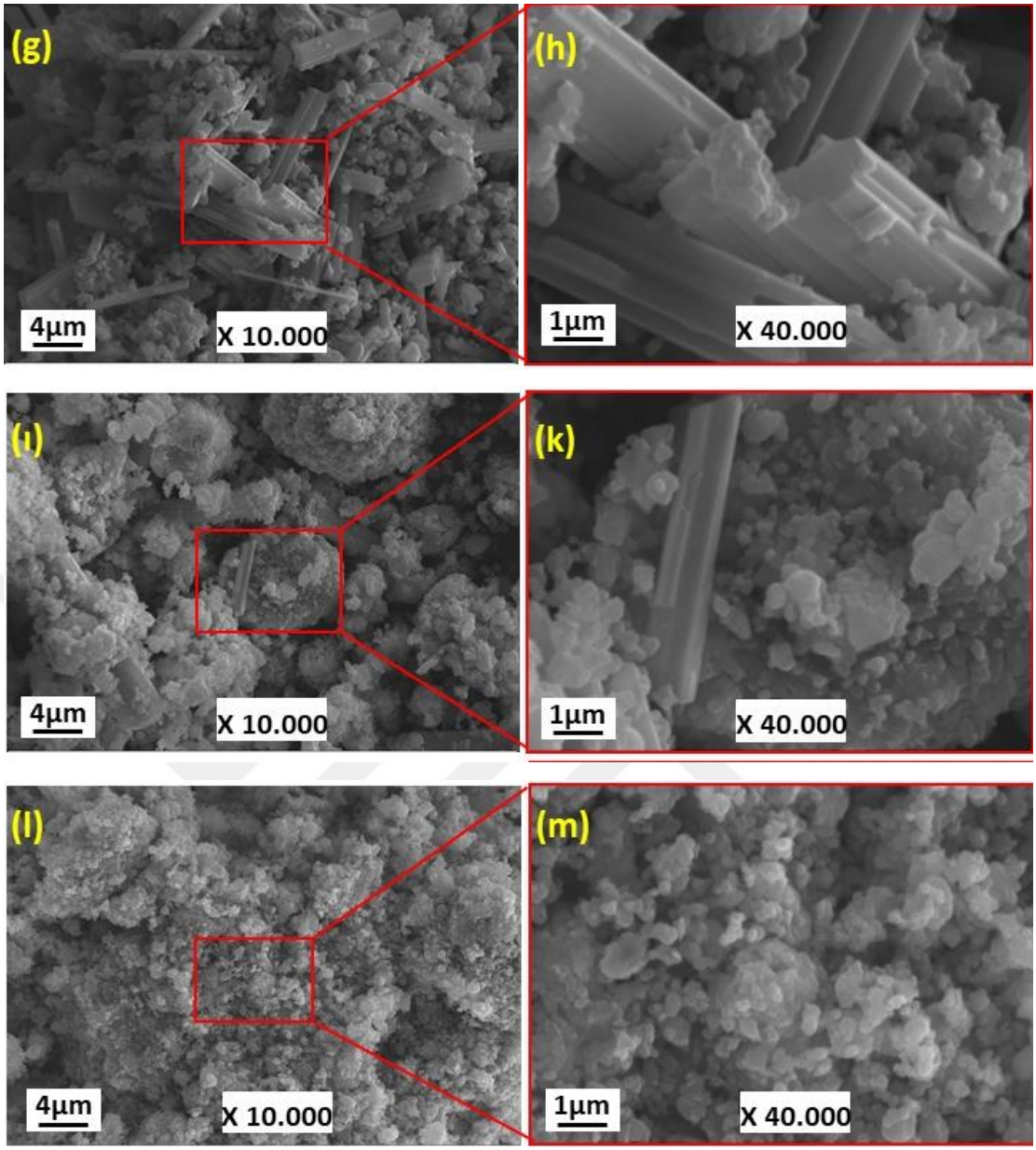

Figure 44. SEM image of $Na_{0.44}Mn_{1-x}Ni_xO_2$ samples: (a)(b) x = 0, (c)(d) x = 0.01, (e)(f) x = 0.05, (g)(h) x = 0.08, (ı)(k) x = 0.11 and (l)(m) x = 0.17.

Figure 45 shows the surface morphologies of $Na_{0.44}Mn_{1-x}Co_xO_2$ samples synthesized with solid state reaction, in different magnifications. As easily be seen from Figure 42 (a)-(d), samples x = 0 and x = 0.01 have similar nanorod forms. In addition, it was observed that these samples had an average width of 540 nm and 943 nm, respectively. Figure 45 (e)(f) shows the SEM images of the x = 0.05 sample. In these pictures, the granular structures of $Na_{0.7}MnO_2$, $Na_{0.58}Mn_{0.5}Co_{0.5}O_2$ and $Na_{0.3}MnO_{2.7}$ appear clearly. Furthermore, the number of these granular structures increase with the increase in cobalt substitution rates in all SEM images of Figure 45, (e) to (m). The

measured widths of the $Na_{0.44}MnO_2$ nanorods for x = 0.05, x = 0.08, x = 0.11, and x = 0.17 are 943 nm, 1828 nm, 1257 nm, and 1103 nm, respectively.

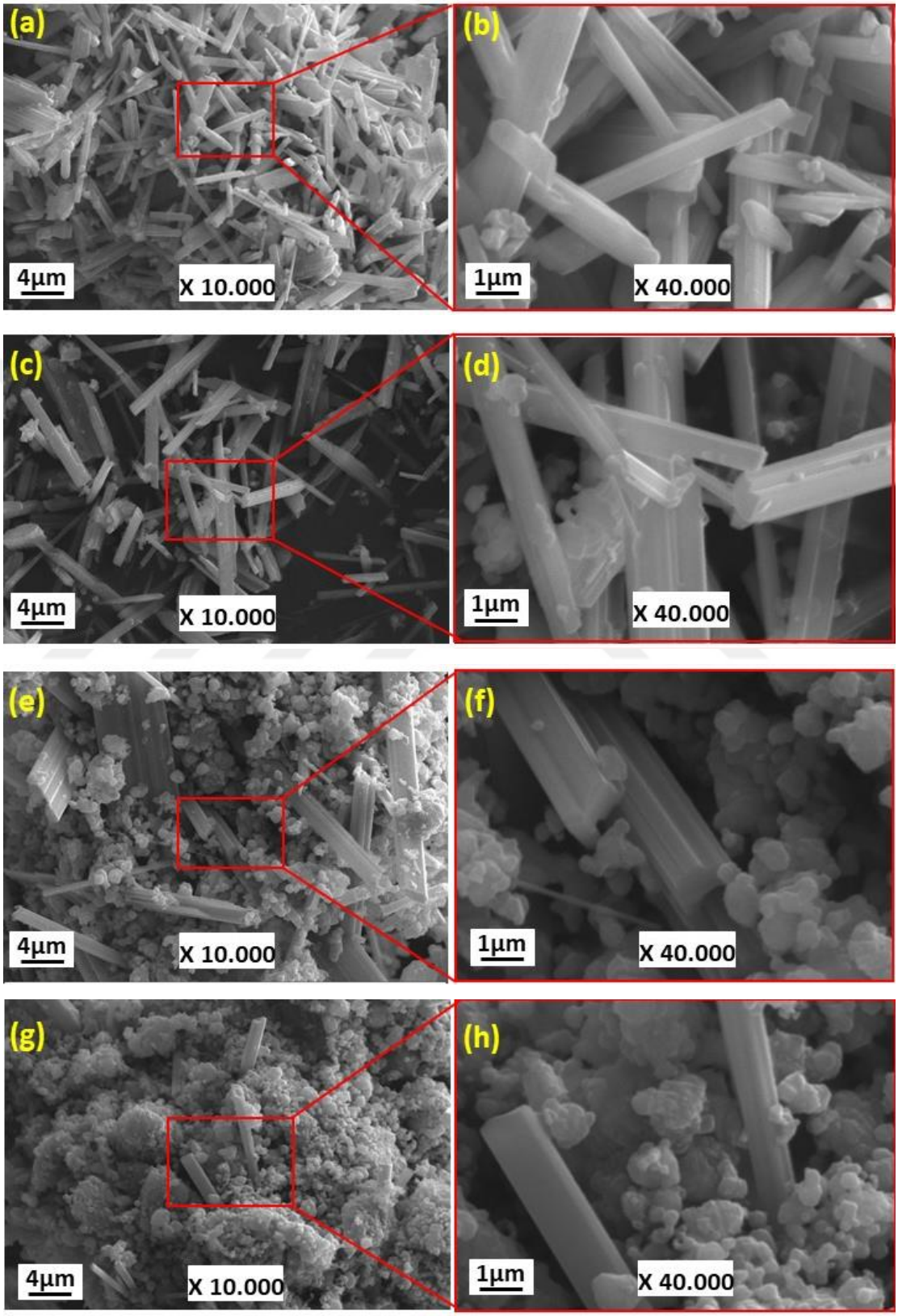

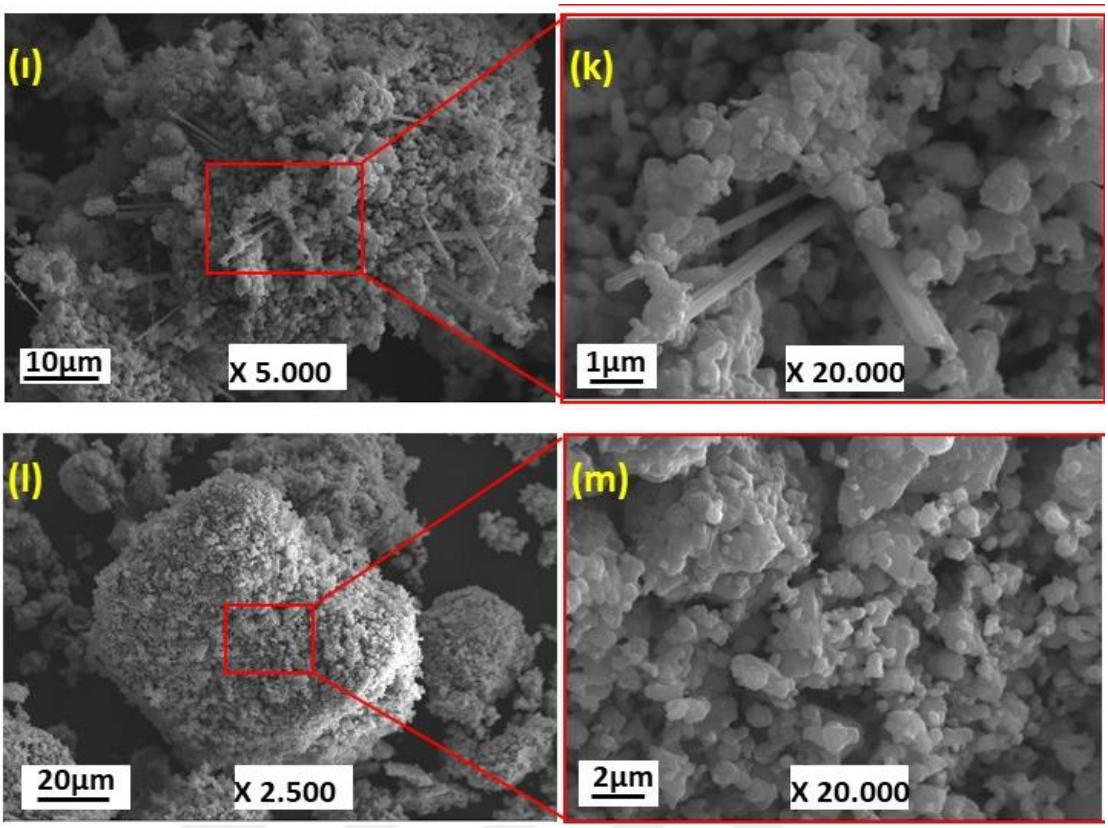

Figure 45. SEM image of Na0.44Mn1-xCoxO2 samples: (a)(b) x=0, (c)(d) x=0.01, (e)(f) x=0.05, (g)(h) x=0.08, (ı)(k) x=0.11 and (l)(m) x=0.17.

3.3.2. TEM Analysis

The TEM, the high-resolution TEM (HRTEM), and the Selective Area Electron Diffraction (SAED) images (as inserted) of $Na_{0.44}Mn_{1-x}Co_xO_2$ samples can be seen in Figure 46. Except for x = 0.17, which contains the highest amount of substitution, it is clearly seen that all samples have a nanorod-like structure. The interplanar distance in the range of 0.42–0.48 nm correspond to the (200) lattice plane [138] (Figure 46 (b), (d), and (f)), while 0.27–0.28 nm range corresponds to (001) lattice plane (Figure 46 (h)). In addition, the lattice plane (200) is parallel to the direction of the [001] growth axis of the nanorods. However, the HRTEM image could not be obtained due to the increase in thickness of the x = 0.11 sample (Figure 46 (ı)). The TEM images of the x = 0.17 sample can be seen in Figure 46 (j)(k); these granular structures might belong to the P2-type $Na_{0.7}MnO_2$, $Na_{0.58}Mn_{0.5}Co_{0.5}O_2$, and $Na_{0.3}MnO_{2.7}$ compounds. The SEAD images of the samples can be seen as inset figures, and according to the results, all the samples were well-grown in the form of single crystals.

According to the HRTEM results, no defects were observed in the x = 0 samples while some structural defects were observed in other samples; these defects might be due to the Co substitution in Mn sites.

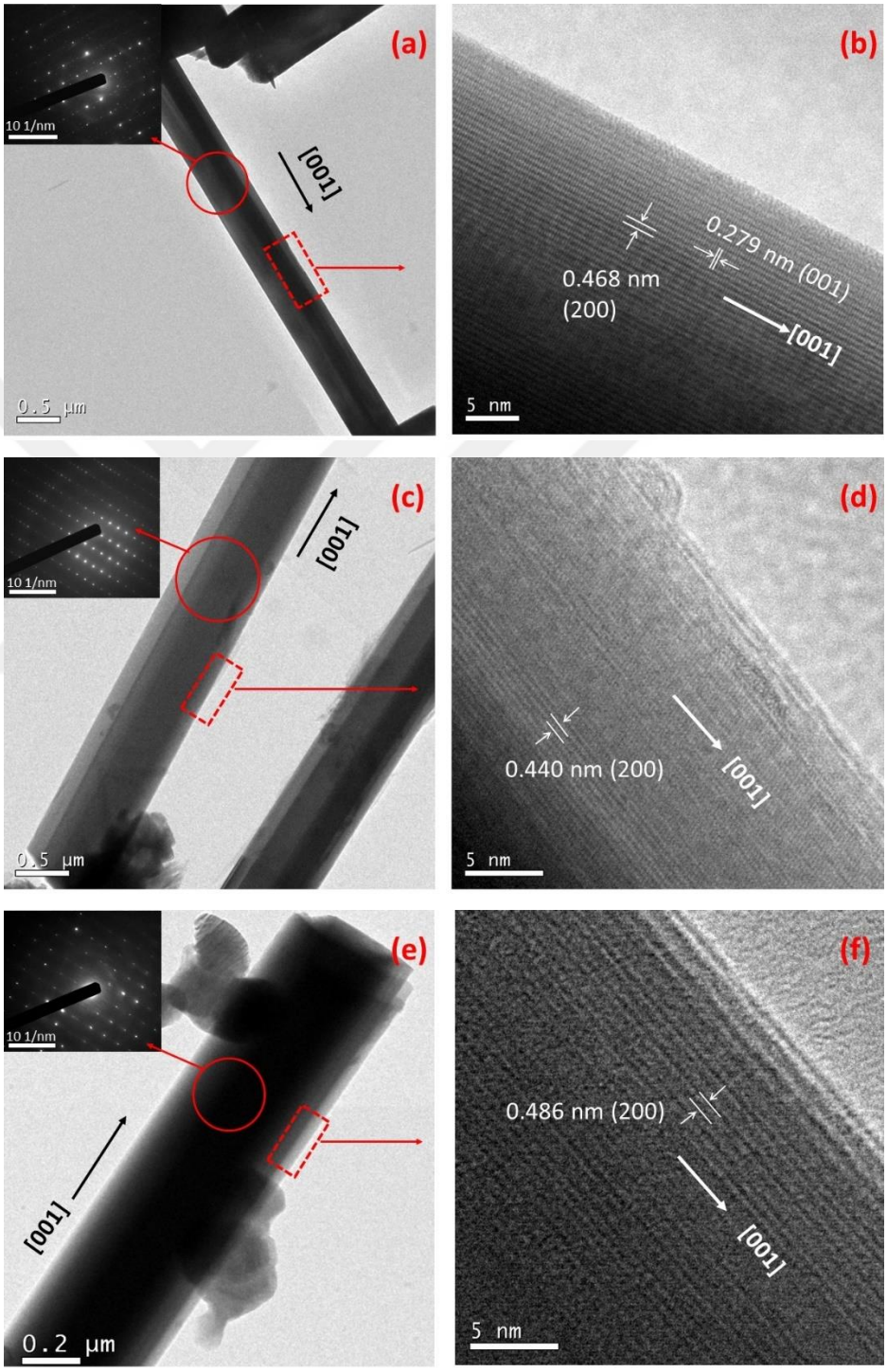

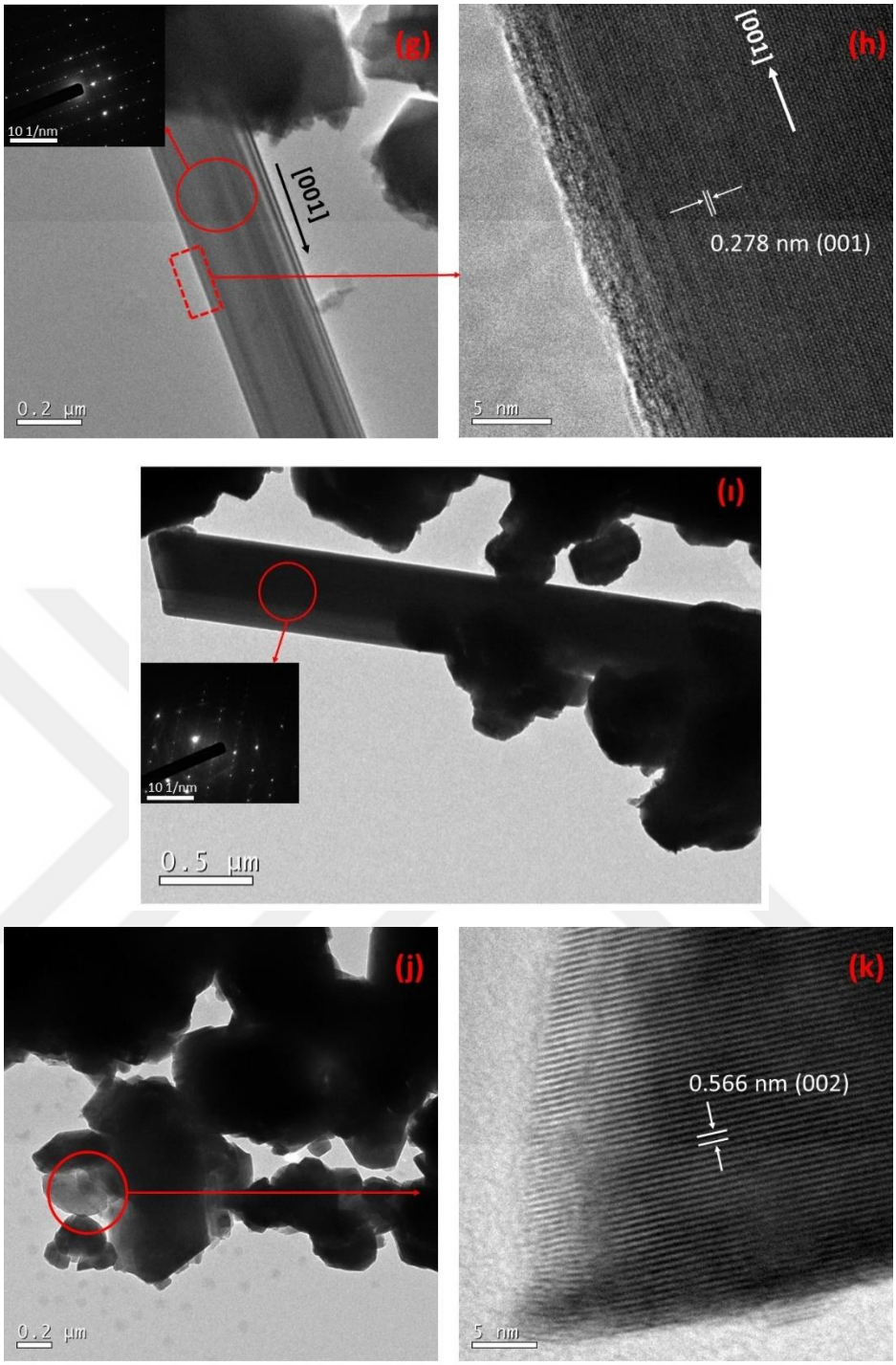

Figure 46. TEM image of $Na_{0.44}Mn_{1-x}Co_xO_2$ (a) x=0, (c) x=0.01, (e) x=0.05, (g) x=0.08, (ı) x=0.11 and (j) x=0.17 (insertion of SEAD); HRTEM image of $Na_{0.44}Mn_{1-x}Co_xO_2$ (b) x=0, (d) x=0.01, (f) x=0.05, (h) x=0.08, and (k) x=0.17.

The TEM, HRTEM, and SAED images (inset) of $Na_{0.44}Mn_{1-x}NixO_2$ samples can be seen in Figure 47 (a)-(k). All samples in the series have a well-crystallized nanorod-like structure. Apart from the unsubstituted x = 0 sample, the $Na_{0.7}MnO_2$ phase in the granular structure can be observed in all samples. The average 0.450-nm-long interplanar distance is shown in Figure 47 (b)(f), corresponding to the (200) plane

[171] that is parallel to the growth direction [001], while the 0.88 nm distance corresponds to the (110) plane in Figure 47 (d)(h). On the other hand, since the samples were too thick, the interplanar distance could not be measured in the x = 0.11 sample, whereas the HTEM image of the x = 0.17 sample could not be obtained. HRTEM analysis is difficult with regard to high substitution rates due to the increase in the merging tendency of nanorods with Co substitution. When the images of SAED (which are inset figures in TEM images) are examined, nanorod structures are formed as single crystals. However, in the HRTEM images of the samples x = 0.08 and x = 0.11, some deformations were observed on their surfaces.

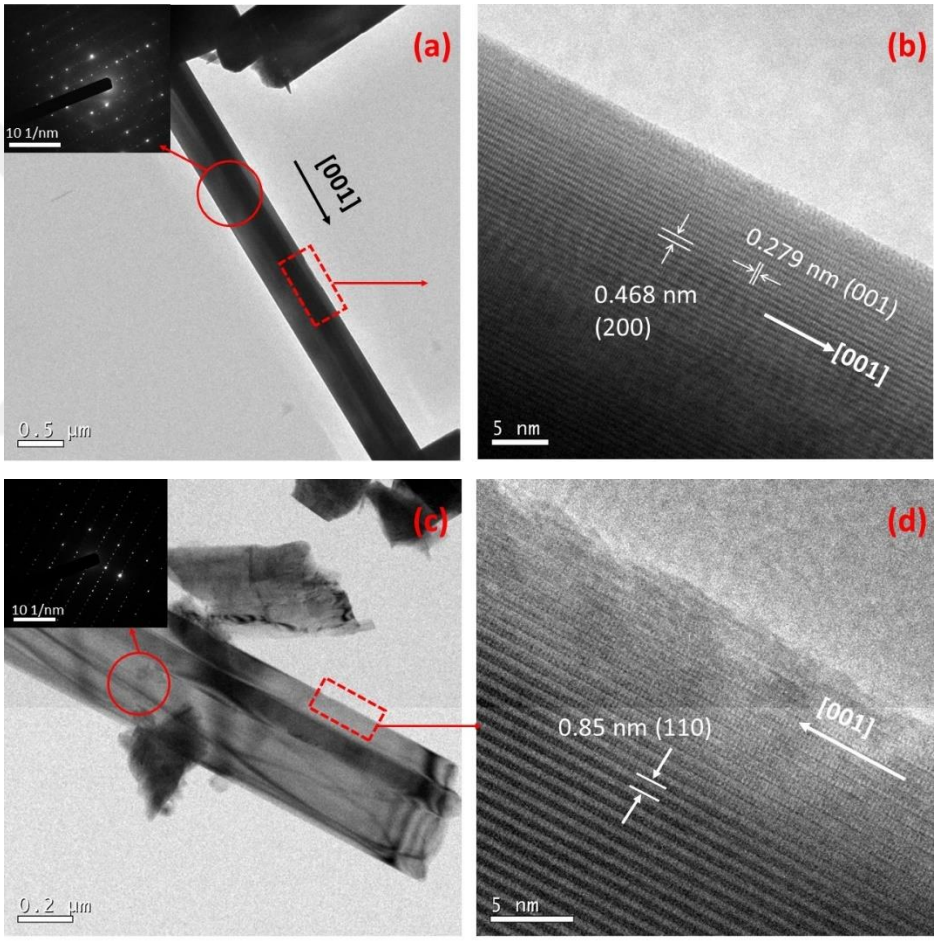

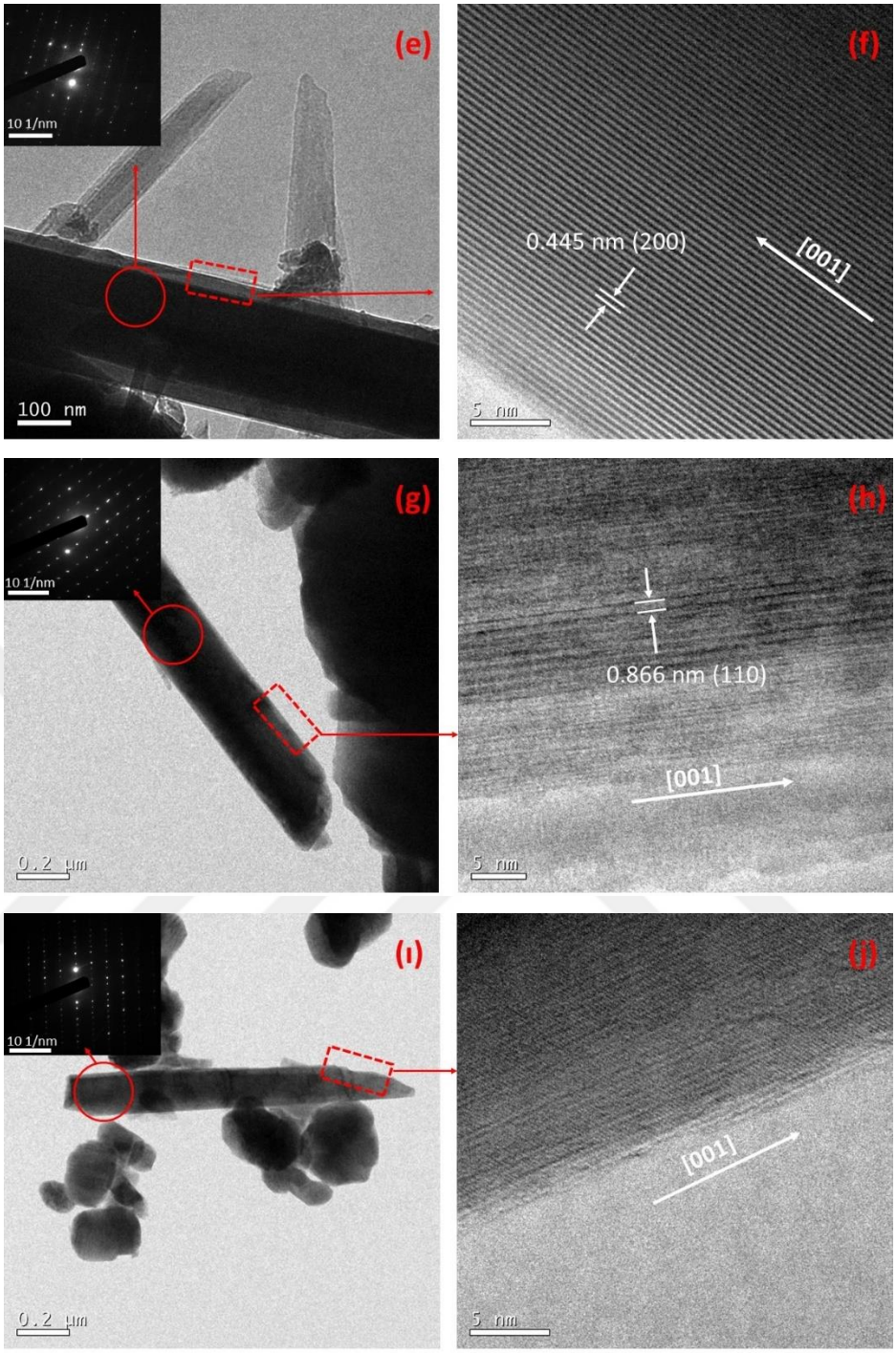
(e)
10 1/nm
100 nm
(f)
0.445 nm (200)
[001]
5 nm
(g)
10 1/nm
0.2 µm
(h)
0.866 nm (110)
[001]
5 nm
(i)
10 1/nm
0.2 µm
(j)
[001]
5 nm

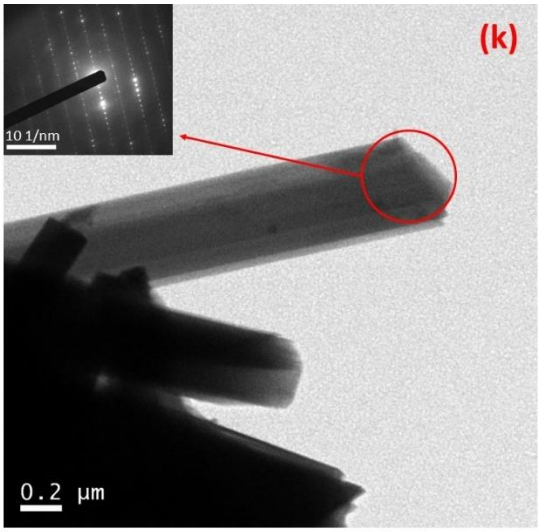

Figure 47. TEM image of $Na_{0.44}Mn_{1-x}Ni_xO_2$ (a) x=0, (c) x=0.01, (e) x=0.05, (g) x=0.08, (ı) x=0.11 and (k) x=0.17 (insertion of SEAD); HRTEM image of $Na_{0.44}Mn_{1-x}Ni_xO_2$ (b) x=0, (d) x=0.01, (f) x=0.05, (h) x=0.08, and (j) x=0.11.

3.4. X-ray Absorption (XAS) Analysis

XAS is a unique way to obtain information about the valence state and the local environment of the elements in the given samples. In our study, Mn K-edge spectroscopy measurements were taken for both $Na_{0.44}Mn_{1-x}Co_xO_2$ and $Na_{0.44}Mn_{1-x}Ni_xO_2$ series, and the Mn valence state and the local environment changes were investigated along with the increase in substitution rates.

Figure 48 shows the Mn K-edge spectra of the samples. Mn^{+3} and Mn^{+4} valence were compared with the Mn K-edge spectra of Mn_2O_3 and Li_2MnO_3 samples, respectively, in order to fully understand the change of Mn valence state values in the samples. In addition, the insets (Figure 48) show that both Mn^{+3} and Mn^{+4} existed in the samples, which is also indicated in the XRD section, and Mn^{+4} increased with the increase of the substitution rate. The peaks seen at 6541 eV and 6543 eV both belong to "pre-edge". These pre-edge structures usually emerge out of from bound state transitions. For the first-row transition metals, K edges arise out of 1s–3d transition and that can be observed for every first-row transition metal if its 3d orbital is not fully occupied. Although the 1s–3d transition is forbidden by dipole selection rules, it is nevertheless observed due to 3d–4p orbital hybridization and as well as direct quadrupolar coupling [172].

The peak, called the "white line," observed at approximately 6560 eV seen in Figure 48(a)(b) increased in intensity with increasing Co and Ni substitution ratio and shifted 0.63 eV and 0.16 eV, respectively, towards high- energy values.

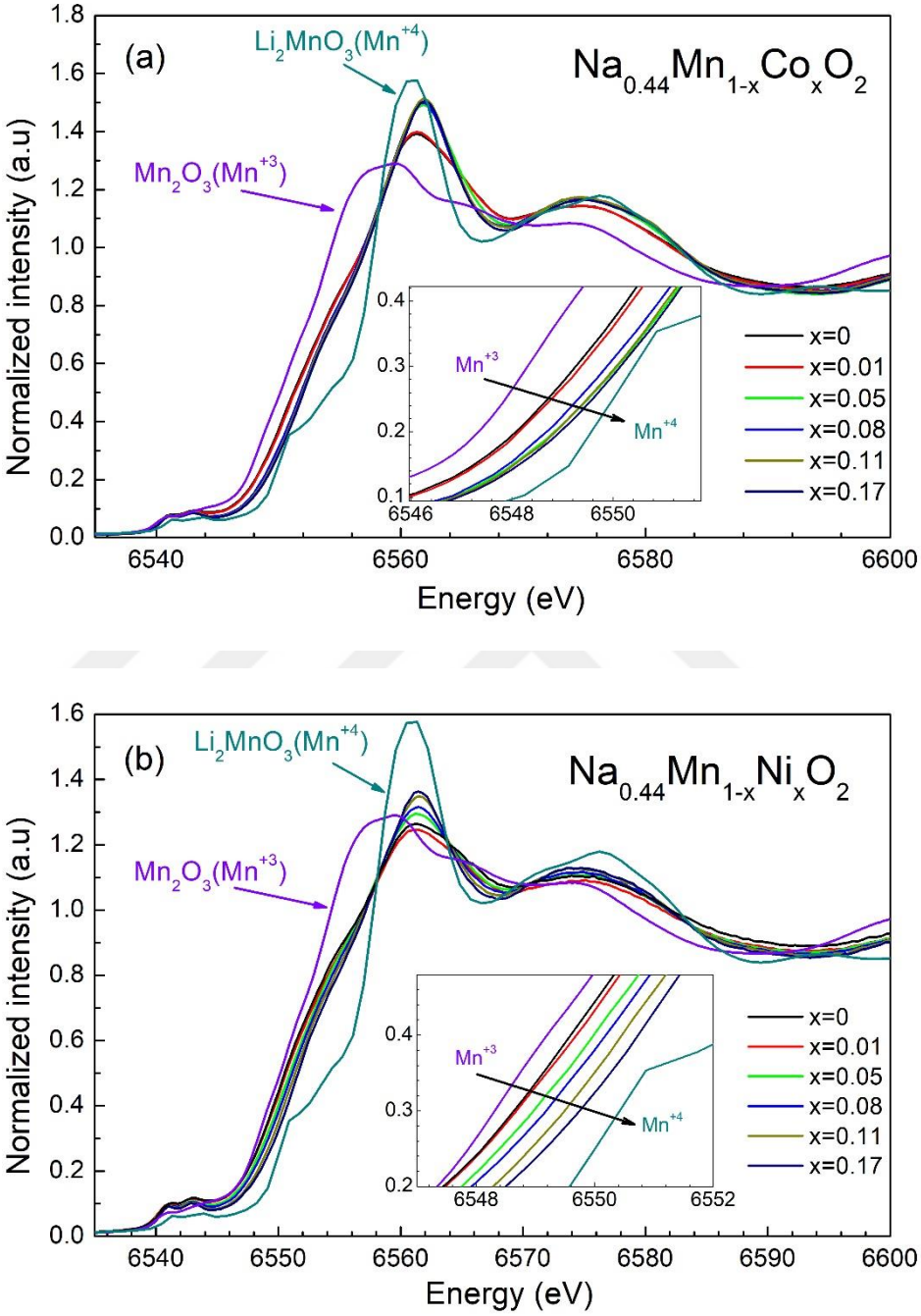

Figure 48. Mn K-edge spectrum of (a) $Na_{0.44}MnCoO_2$ and (b) $Na_{0.44}MnNiO_2$ series. Mn K-edge spectra of standard Mn_2O_3 and Li_2MnO_3 samples were added to compare the Mn valence states of the samples.

The peak shift to high energies occurs due to the increase of Mn^{+4} / Mn^{+3} ratio. On the other hand, the increase in white line intensity is due to the increase in MnO_6 octahedra distortion [173], which is possible when Co and Ni substitution happens in the Mn sites.

For further investigation, radial distance analysis was performed by using EXAFS Fourier Transform (FT) data, and both FT spectra seem almost identical (Figure 49 (a)(b)). Each peak in the FT spectrum is the results of scattering from the nearest neighboring Mn atom. In this case, for both sample series, the first peak occurred around 1.9 Å from the Mn-ligand (Mn-O), the second peak around 2.8–2.9 Å from the Mn-metal (Mn-Mn or Mn-Ni), and 3.1–3.5 Å from the Mn-Mn/Na coordination shell [174]. Except for the Mn-O coordination, all peaks gradually shifted to higher radial distance values with increasing Co and Ni substitution ratio. These shifts might have occurred due to the MnO_6 octahedra distortion and/or the longer Mn-Co and Mn-Ni bond length. Moreover, it was observed that the Mn-O peaks shifted to a small radial distance, perhaps due to an increase of Mn^{+4} / Mn^{+3} ratio as a result of the substitution of Ni and Co ions with Mn^{+3}, which thereby reduced the length of the Mn-O bond [124].

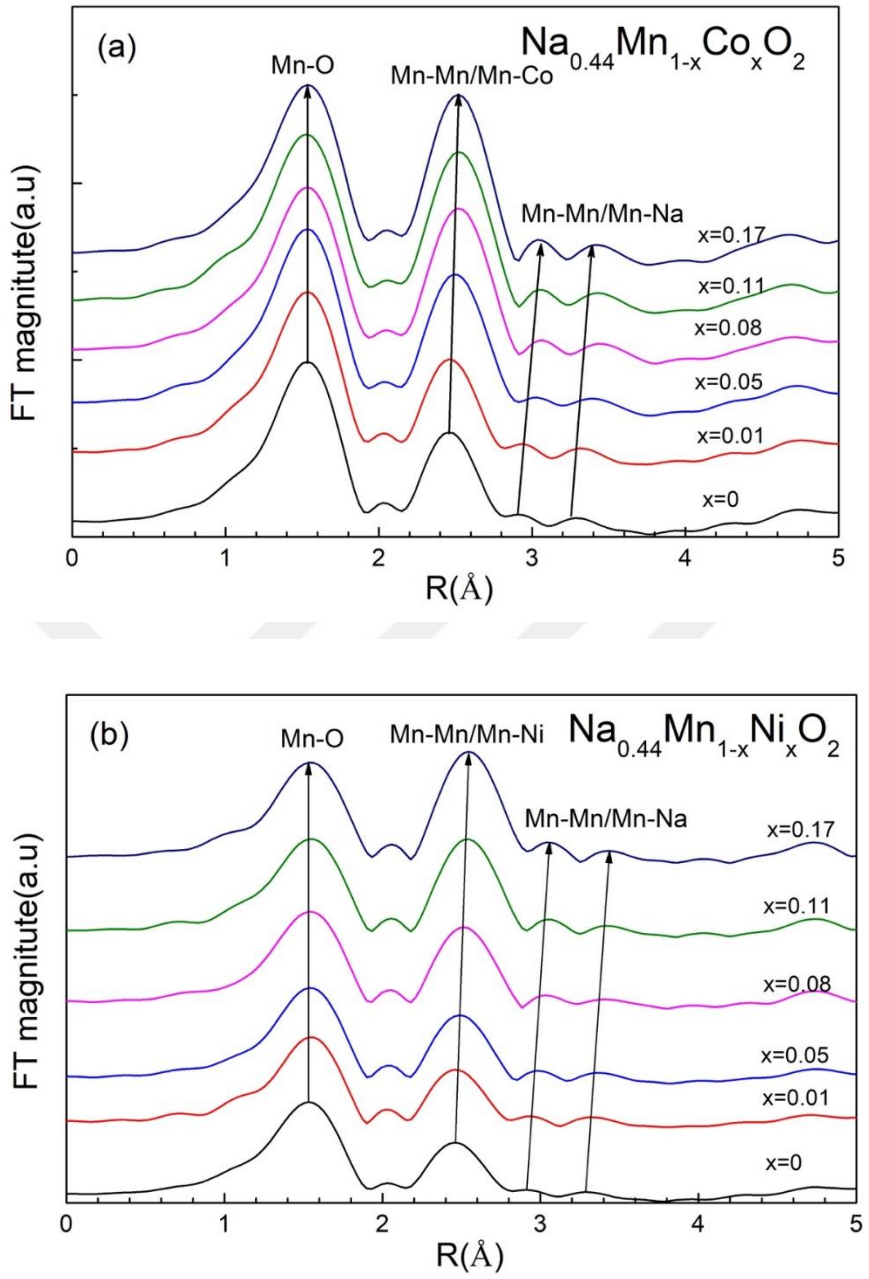

Figure 49. The radial structure's function for (a)$Na_{0.44}MnCoO_2$ and (b) $Na_{0.44}MnNiO_2$ obtained from the Fourier transformation of k3 -weighed Mn K-edge EXAFS oscillations.

3.5. Magnetic Measurements

From previous studies, the $Na_{0.44}MnO_2$ sample has been known to possess paramagnetic properties [175]. As mentioned in the crystal structure analysis, Mn^{+4} and Mn^{+3} ions exist ($Na_4^{+1}Mn_4^{+3}Mn_5^{+4}O_{18}^{-2}$) to ensure the charge equivalence in the given sample. However, all Mn^{+4} ions are in the octahedral MnO_6 site, while Mn^{+3}

ions are found in both octahedral MnO_6 and square pyramidal MnO_5 sites. These ions may have different spin configuration values according to their environment: Mn^{+4} ions have three unpaired electrons in an octahedral environment (Figure 50). While Mn^{+3} ions have LS configuration in the square pyramid structure environment, Mn^{+3} may exist in either HS or LS configuration due to the strength of the ligand effect in an octahedral environment.

The arguments about the change in the magnetic moments of the samples were evaluated by comparing the theoretical calculation and the experimental results.

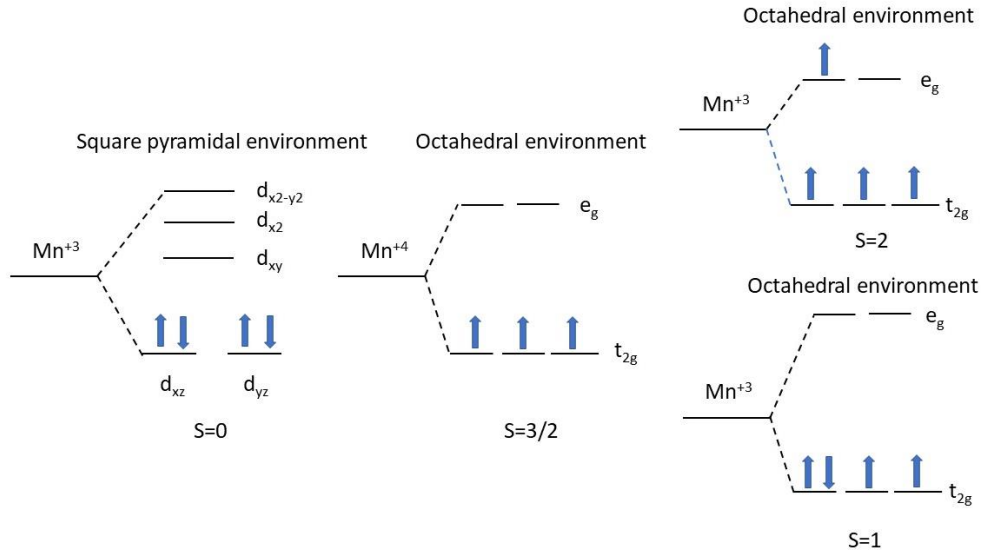

Figure 50. Energy-level splitting of the Mn^{+3} and Mn^{+4} d orbital in octahedral and square pyramidal environments.

The effective magnetic moment can be calculated from the following equation:

$$\mu_{eff} = g\sqrt{S(S+1)}\mu_B \qquad (8),$$

where μ_B is the Bohr magneton, g is the spectroscopic splitting factor and S is the spin quantum number. According to this equation, Mn^{+4} ion has 3.97 μ_B and Mn^{+3} ion has 4.9 μ_B in HS states and has 2.83 μ_B in LS states within an octahedral environment.

According to the previous studies, $Na_{0.44}MnO_2$ displays Curie-Weiss type magnetic behavior at low temperatures [135]. Therefore, the magnetic susceptibility values of the samples were calculated by using Curie-Weiss law to evaluate their magnetic behavior [176].

$$\chi(T) = \frac{C}{T-\theta} + \chi_{core} + \chi_{pauli} + \chi_{VV} \qquad (9),$$

where χ_{core} is temperature-independent diamagnetism of the filled electronic shells of core ions, χ_{pauli} is a contribution related to the chemical potential of the samples, χ_{VV} is the Van-Vleck susceptibility term originating from the transitions between the ground state and the excited state of the partially-filled d-shells in the octahedral crystal field, C is the Curie-Weiss constant (which is defined as C= $\mu_{eff}^2/8$), and θ is the Weiss temperature (the sing of this θ value may lead to either ferromagnetism or antiferromagnetism). The experimentally effective magnetic moments of the samples were calculated from the χ^{-1}-T curve between 200-300 K, as per the Curie-Weiss law. Figure 51 shows the temperature-dependent inverse magnetic susceptibility of Co substituted samples. According to Figure 51, the magnetic susceptibility of the samples increased with decreasing temperature.

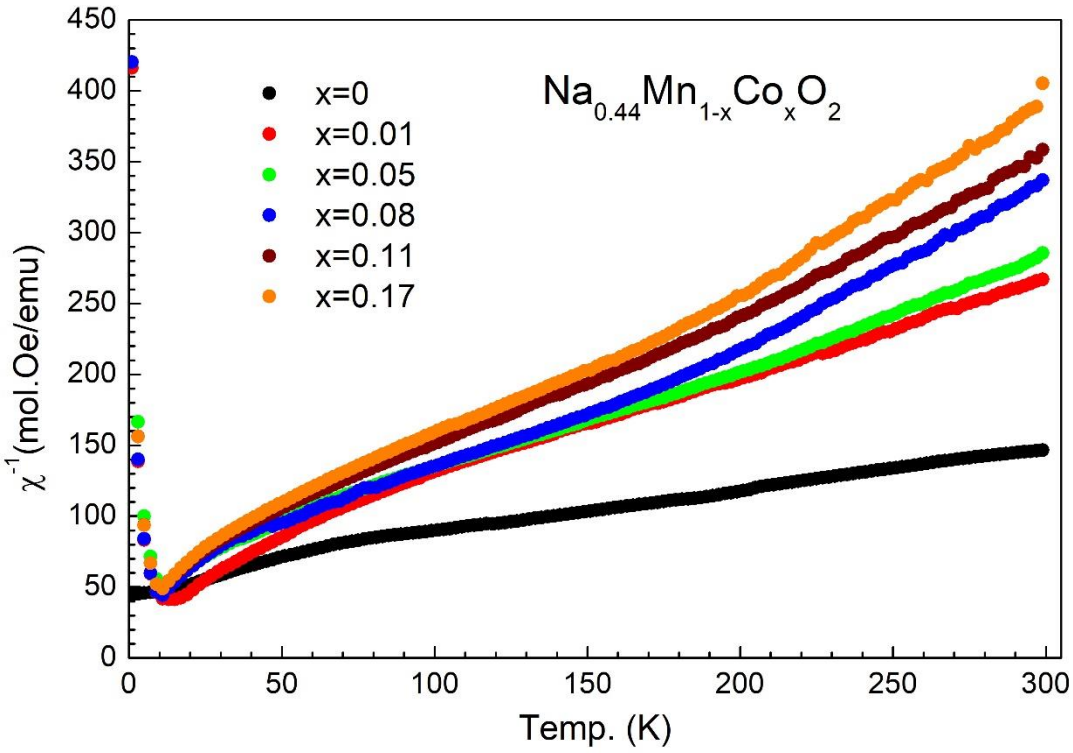

Figure 51. Inverse magnetic susceptibility as a function of temperature for $Na_{0.44}Mn_{1-x}Co_xO_2$ samples.

Additionally, it is clearly seen that the magnetic susceptibility of the samples decreased with the increase of Co substitution ratio. The μ_{eff} values obtained from the experimental data, according to the Curie-Weiss fitting, can be seen in Table 3.

Table 3. μ_{eff} value of the $Na_{0.44}Mn_{1-x}Co_xO_2$ samples.

Sample	**$\mu_{eff}(\mu_B)$**
x=0	3.76
x=0.01	3.44
x=0.05	3.26
x=0.08	2.74
x=0.11	2.83
x=0.17	2.53

One of the reasons for this decrease in μ_{eff} is explained as follows. As mentioned in the crystal structure analysis, the substituted Co ions tend to be replaced by Mn^{+3} ions in the octahedral structure. In this case, there are two possibilities. First, Co^{+3} ions might have an HS configuration in the octahedral environment, and consequently the Co^{+3} μ_{eff} is 4.9 μ_B (Figure 52). However, we can ignore this possibility due to the decrease in the μ_{eff}. Second, Co^{+3} ions might be in the LS configuration (Figure 52, $\mu_{eff} = 0$) in an octahedral environment, which is reported in previous studies [177,178], and, thus, does not contribute to the μ_{eff} of the samples. It is clear that the second probability is consistent with the experimental data and, therefore, we can assume that Co^{+3} ions possess LS configuration.

Another point: although the P2-type compounds became dominant with increasing substitution rate, they did not contribute to μ_{eff} value. In this case, we can assume that Co^{+3} ions in the octahedral environment have LS configuration, similar to T-type compounds.

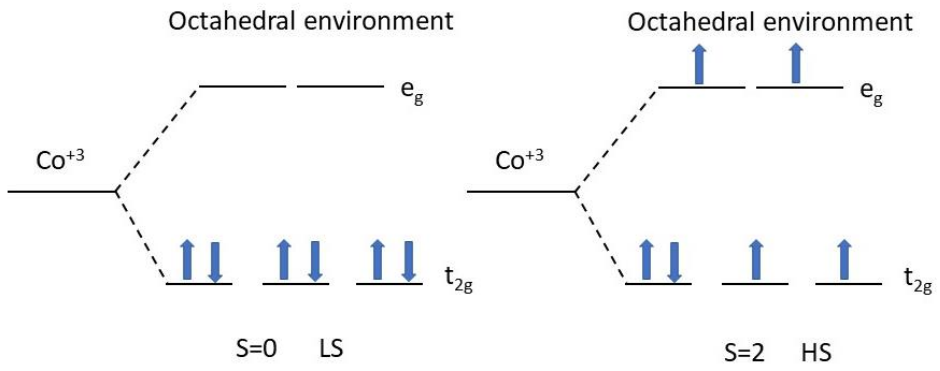

Figure 52. Energy-level splitting of the HS and LS Co^{+3} d orbital in octahedral environments.

The main reason behind the reduction in the μ_{eff} is probably the increase in the rate of Mn^{+4} consequent to the increase in the Co substitution rate. In the analysis of the XAS results, it was clearly observed that the Mn^{+4}/Mn^{+3} rate increased with the increase in Co substitution (Figure 48).

Figure 52 shows the temperature-dependent inverse magnetic susceptibility of Ni-substituted samples. As observed, the magnetic susceptibility of the samples increased with decreasing temperature; however, it increased with the increase in Ni substitution.

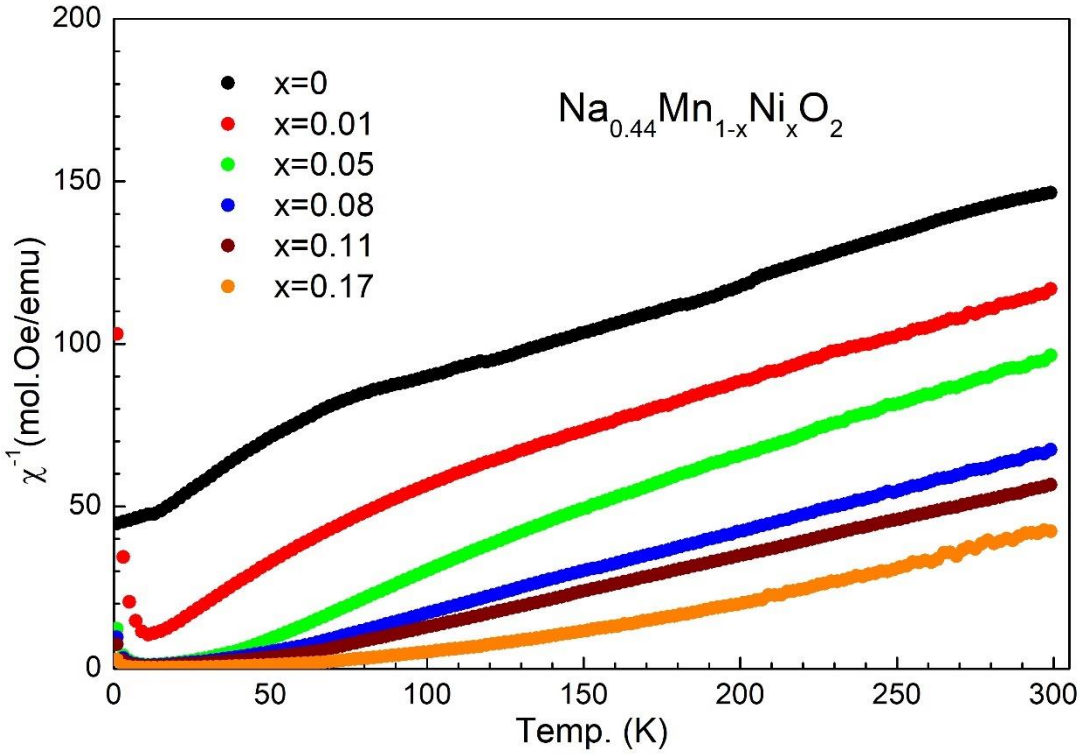

Figure 53. Inverse magnetic susceptibility as a function of temperature for $Na_{0.44}Mn_{1-x}Ni_xO_2$ samples.

The μ_{eff} values obtained from the experimental data according to the Curie-Weiss fitting can be seen in Table 4. The obtained data shows that μ_{eff} value increased with increasing Ni substitution.

Table 4. μ_{eff} values of the $Na_{0.44}Mn_{1-x}Ni_xO_2$ samples.

Sample	**μ_{eff} (μ_B)**
x=0	3.76
x=0.01	3.82
x=0.05	3.96
x=0.08	4.01
x=0.11	6.08
x=0.17	6.17

The one of the reasons behind this increase in μ_{eff} is explained as follows. As indicated in the crystal structure analysis, the substituted Ni ions tend to be replaced by Mn^{+3} ions in the octahedral structure. There are two states for Ni on the octahedral site: Ni^{+2} and Ni^{+3} (Figure 54). We can identify which of these two situations could be found in the abovementioned structure by comparing the theoretical μ_{eff} values from Eq. 8. In this case, since Mn^{+3} ions have 2.83 μ_B in the octahedral environment and only Ni^{+3} in the HS state substitution can contribute its μ_{eff} value, we can therefore argue that Mn^{+3} was substituted with Ni^{+3} ions in HS state.

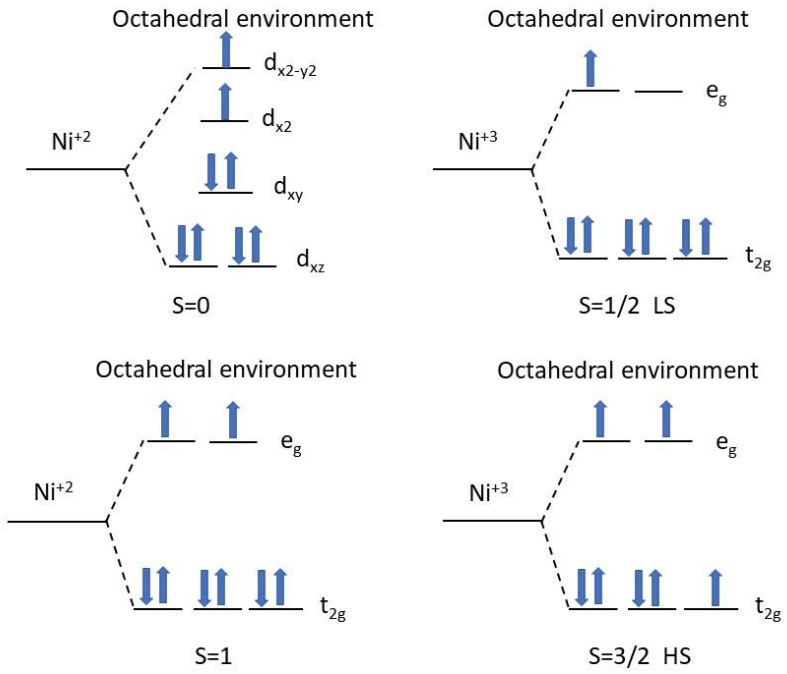

Figure 54. Energy-level splitting of the Ni^{+2} and Ni^{+3} d orbital in octahedral environments.

Table 5. The μ_{eff} value in the octahedral environment calculated from Equation 8.

	μ_{eff} (μ_B)	
	HS	LS
Ni^{+3}	3.87	1.73
Ni^{+2}	2.82	2.82
Co^{+3}	4.90	0
Mn^{+3}	4.90	2.83
Mn^{+4}	3.97	-

One of the main strategies used to reduce the JT effect that causes crystal structure degradation in the Mn sites is to reduce the number of Mn^{+3} or substitution with a lower valence TM to convert Mn^{+3} ions to Mn^{+4} ions [100]. In our case, it is clear from the results that Mn^{+3} numbers are decreased by Co^{+3} and Ni^{+3} substituting in Mn^{+3} sites. Additionally, abovementioned, Co^{+3} in LS and Ni^{+3} in HS state are not under the JT effect due to spin configurations in the octahedral environment. This will have a direct effect on battery performance by lowering the crystal structure degradation due to JT at high charge/discharge cycles, which will be discussed in Electrochemical Analysis.

3.6. Electrochemical Analysis

3.6.1. Cyclic Voltammetry (CV)

The (de)insertion properties of Na ions for $Na_{0.44}Mn_{1-x}Co_xO_2$ samples were investigated by CV measurements. Figure 55 shows the CV measurements of $Na_{0.44}Mn_{1-x}Co_xO_2$ samples at 0.1 mV / s scan rate. In Figure 55(a), six cathodic peaks located at 2.17, 2.40, 2.62, 2.94, 3.17 and 3.41V are clearly seen for the sample x = 0 ($Na_{0.44}MnO_2$), and this observation is also consistent with the previous works [166,179]. Moreover, the formation of these peak pairs (cathodic and anodic) also proves that the reactions are reversible. However, the absence of a significant change in the positions of the redox peaks at the end of four cycles indicates that the charge/discharge processes are stable. The multiple peaks show the multiphase

transition mechanism during the Na-ion insertion/extraction reactions at different sites. In addition, these multi-phase transitions can be clearly seen in the capacity graphs examined in the next section. The low difference between the potential values of the cathodic and anodic peaks observed in the graph indicates high ionic conductivity [143]. The shoulder around 3.1V in Figure 55 (a) originate from Na1 regions located in small tunnel-like structures in the $Na_{0.44}MnO_2$ [180], although it is difficult to show a redox reaction normally.

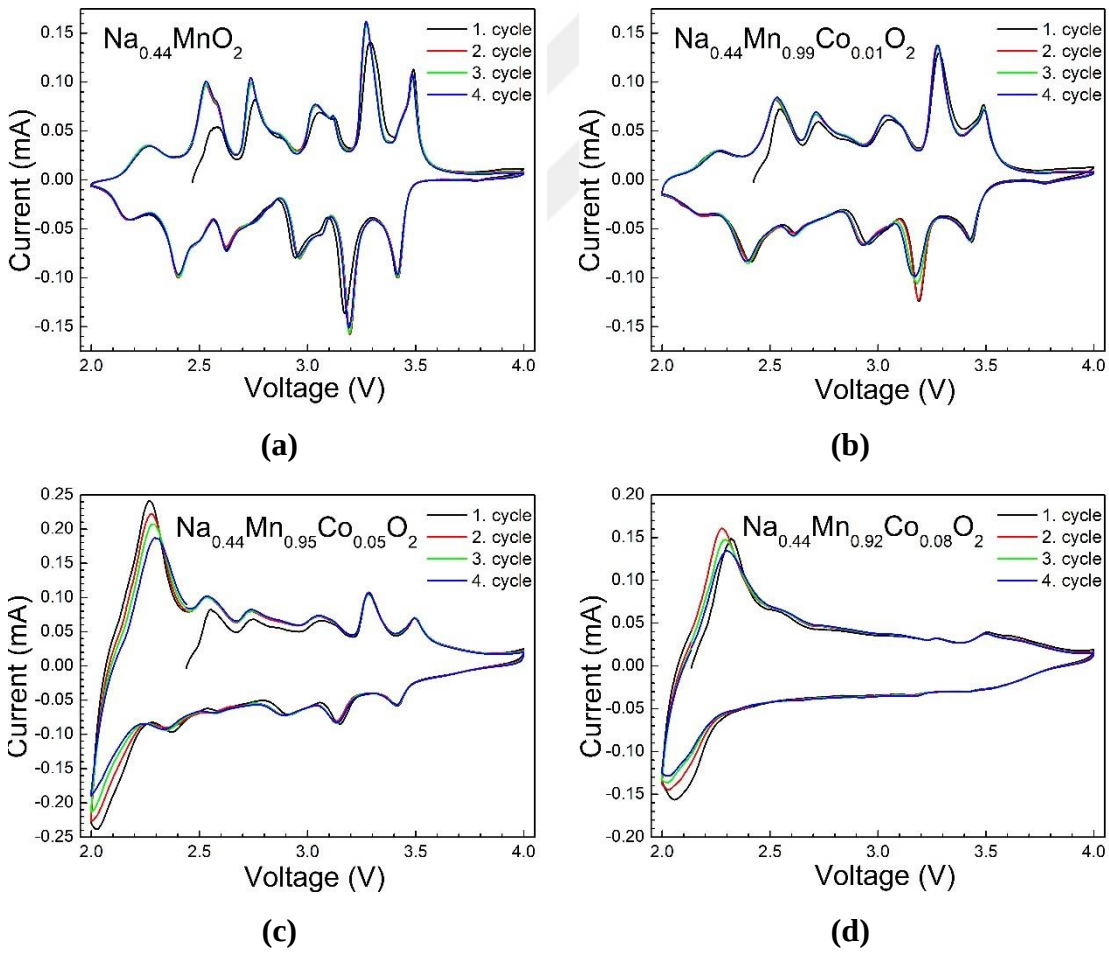

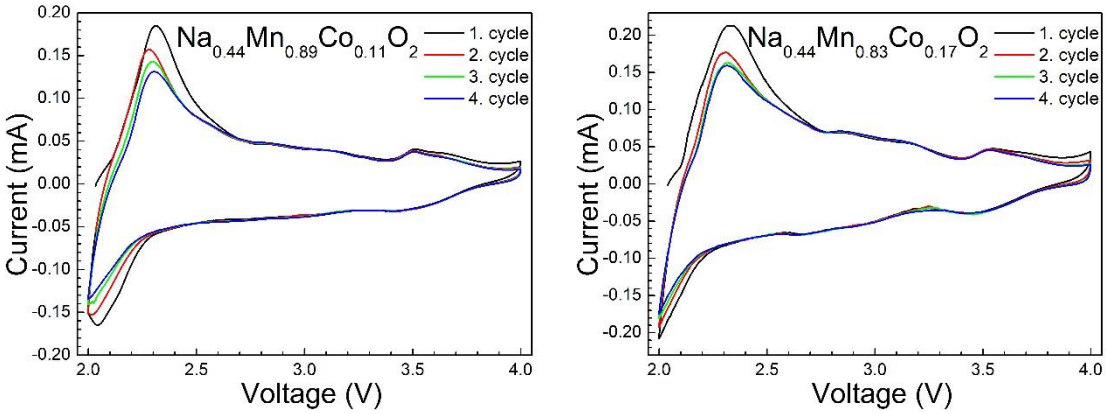

(e) **(f)**

Figure 55. Cyclic voltammetry of $Na_{0.44}Mn_{1-x}Co_xO_2$ ($0 < x < 0.17$) samples between 2 - 4 V potential window at a 0.1 mV/s scan rate.

Figure 55 (b) shows the CV graph of the x = 0.01 sample, and the shoulder at 3.1 V from the Na1 region in the small tunnel-like structure is not observed. Also, the current values in the graph are lower than x = 0, which may have been caused by some irreversible reactions. The six cathodic peaks in 2.18 V, 2.39 V, 2.61 V, 2.93 V, 3.18 V, and 3.43 V are very similar those in the x = 0 sample. As the increase in Co substitution caused the $Na_{0.7}MnO_{2.05,}$ $Na_{0.58}Mn_{0.5}Co_{0.5}O_2$ and $Na_{0.3}MnO_{2.7}$ phases to become dominant, the new redox peaks located at 2.01 V and 2.17 V are observed in the CV graph of x = 0.05 sample (Figure 55(c)) [181]. However, the redox peaks of the $Na_{0.44}MnO_2$ phase can still be seen in the CV graph. Although the redox peaks cannot be seen in the CV graphs of the other samples, it is thought that this indicates the overlap of the redox peaks of the two phases. In the CV graphics of the other samples, the redox peaks of $Na_{0.44}MnO_2$ were not seen due to the reduction of the phase ratio in the samples. However, since the redox peaks of both phases are known to overlap, the redox peaks of the $Na_{0.3}MnO_{2.7}$ phase were also not observed.

Figure 56 shows the CV curves of the $Na_{0.44}Mn_{1-x}Ni_xO_2$ series. In the CV of the x = 0.01 sample, six cathodic peaks are located at 2.17 V, 2.40 V, 2.62 V, 2.95 V, 3.18 V, and 3.42V (Figure 56 (b)), similar to the x = 0 sample. The CV graph shows a decrease in the current values compared to x = 0, resulting from the presence of irreversible reactions due to $Na_{0.7}MnO_2$ on the cathode surface.

In contrast to the Co series, the redox peaks of $Na_{0.7}MnO_2$ phase were not dominant in the CV graph of the x = 0.05 sample (Figure 56 (c)). This is because the ratio of the $Na_{0.7}MnO_2$ phase in this example is less than the ratio in the same sample with regard to the Co series, as reported in the XRD results. However, the redox peaks at 2.09 V

and 3.59 V originate from $Na_{0.7}MnO_2$ [182]. The former peak became dominant from x = 0.08 and, thus, the redox peaks of $Na_{0.44}MnO_2$ phase in the samples x = 0.11 and x = 0.17 could not be observed.

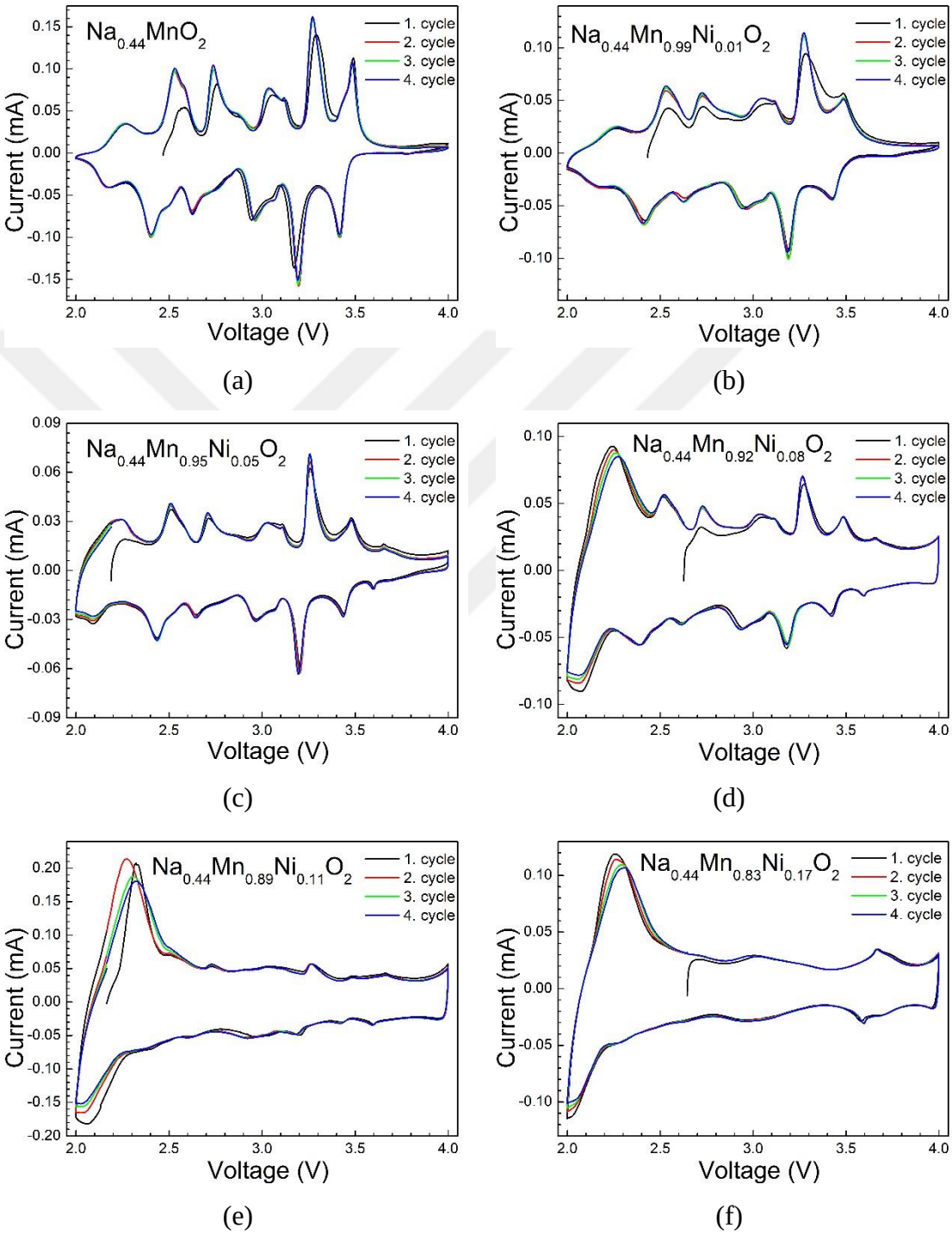

Figure 56. Cyclic voltammetry of $Na_{0.44}Mn_{1-x}Ni_xO_2$ (0<x<0.17) samples between a 2-4 V potential window at a 0.1 mV/s scan rate.

3.6.2. Capacity Analysis

Na2 and Na3 sites in the $Na_{0.44}MnO_2$ crystal structure have a large S-shaped tunnel structure; as mentioned in the structural analysis section, these sites have an important role in the insertion/extraction mechanism. The effect of these Sodium sites on the capacity curves is investigated in this section.

Figure 47 shows the initial discharge curve and the CV curve (inset) of the $Na_{0.44}MnO_2$ sample. Reaction peaks and plateaus originating from the same Na sites are indicated by the same number. The plateau transitions in the discharge curve are also characteristic of multiple phase transitions. Accordingly, in the discharge curve, plateaus 1, 2, 3, and 5 are associated with the Na2 site, while 4 and 6 are associated with reactions in the Na3 site [160]. However, the initial discharge value for the $Na_{0.44}MnO_2$ sample was observed about 84 mAh/g at a 0.3 C rate.

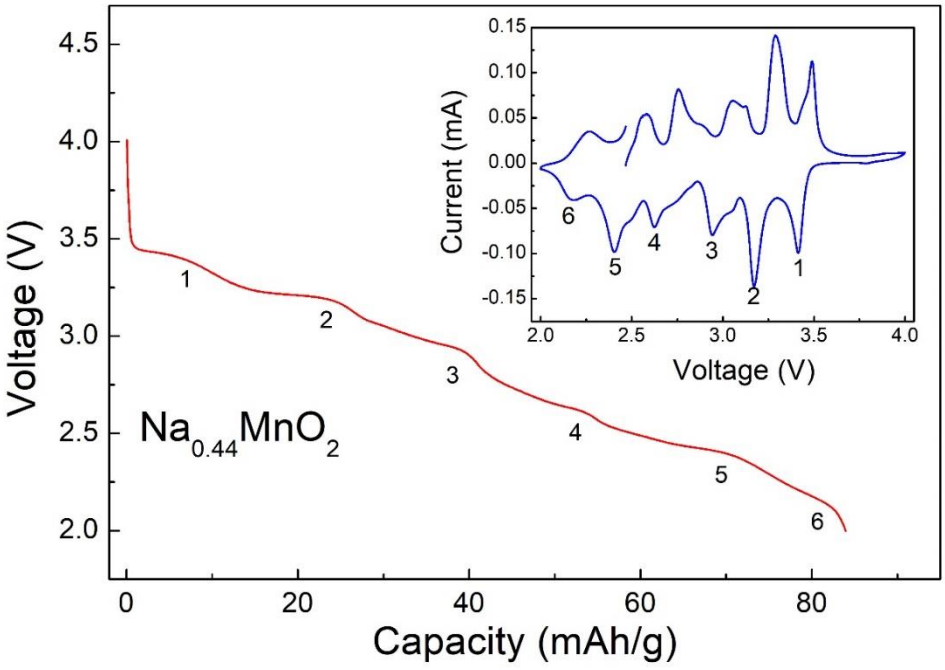

Figure 57. The first discharge and CV curve (inset) of $Na_{0.44}MnO_2$. The peaks of the redox reactions in the CV graph are numbered the same as the corresponding plateau in the discharge curve.

Figure 58 shows the charge/discharge curves of the $Na_{0.44}Mn_{1-x}Co_xO_2$ series. With the increase in Co substitution, the plateau structure seen in the capacity curve gradually turns into the sloping structure. This transition may have occurred because the Co substitution disrupted the charge/Na order in the structure.

In the $Na_{0.44}MnO_2$ capacity graph, with the increase in the number of cycles, the plateaus, which were clearly visible in the first cycle, started disappearing due to structural degradation damaging the insertion/extraction mechanism of Na (Figure 58(a)). The capacity curves of the x = 0.01 sample (Figure 58(b)) are very similar to $Na_{0.44}MnO_2$, and this sample has 83.9 mAh/g initial capacity, which is consistent with the results obtained from the CV analysis. On the other hand, these plateaus were almost not observed in the capacity curves of samples x = 0.05, x = 0.08, x = 0.11, and x = 0.17 (Figure 58 (c)-(f)). However, we can argue that the reason behind this observation is that the amount of $Na_{0.7}MnO_2$ and $Na_{0.58}Mn_{0.5}Co_{0.5}O_2$, which become dominant with increasing Co substitution, is higher than $Na_{0.44}MnO_2$ in these samples. Nevertheless, they have 98.4 mAh/g, 115.75 mAh/g, 118.25 mAh/g, and 111.1 mAh/g initial capacities, respectively, all of which are high in degree. This is because these compounds allow for more Na diffusion in their P2 layered structure [145].

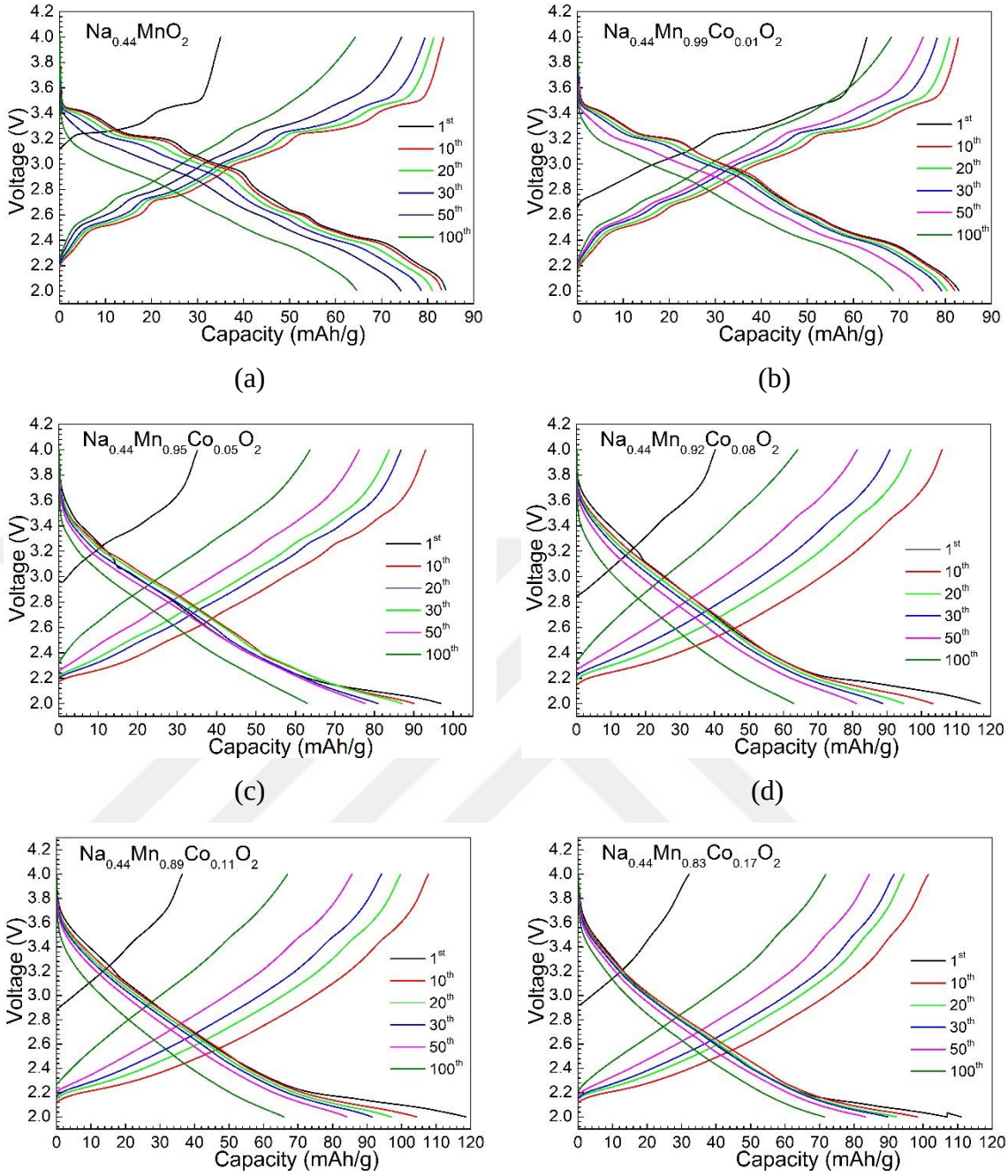

Figure 58. 1st, 10th, 20th, 30th, 50th and 100th discharge/charge curve of $Na_{0.44}Mn_{1-x}Co_xO_2$ in a 2-4 V voltage window at a 0.3C current rate (1C=121 mAh) versus Na/Na^+. (a) x=0, (b) x=0.01, (c) x=0.05, (d) x=0.08, (e) x=0.11 and (f) x=0.17.

The cyclic performance of the $Na_{0.44}Mn_{1-x}Co_xO_2$ series over 100 cycles at 0.3 C can be seen in Figure 59. The coulombic efficiency of all samples was close to 100%, which indicates that the Na insertion reaction is highly reversible. On the other hand, it was observed that the x = 0 and x = 0.01 samples underwent 23% and 17.25% capacity fade after 100 cycles, respectively. Although the initial capacity values of x = 0.05, x = 0.08, x = 0.11, and x = 0.17 samples were high, the observed capacity fade at the

end of 100 cycles were 35%, 45%, 44%, and 36%, respectively. Although the JT effect from Mn^{+3} ions is inevitably present in the $Na_{0.44}MnO_2$ and T-type x = 0.01 still show high stability.

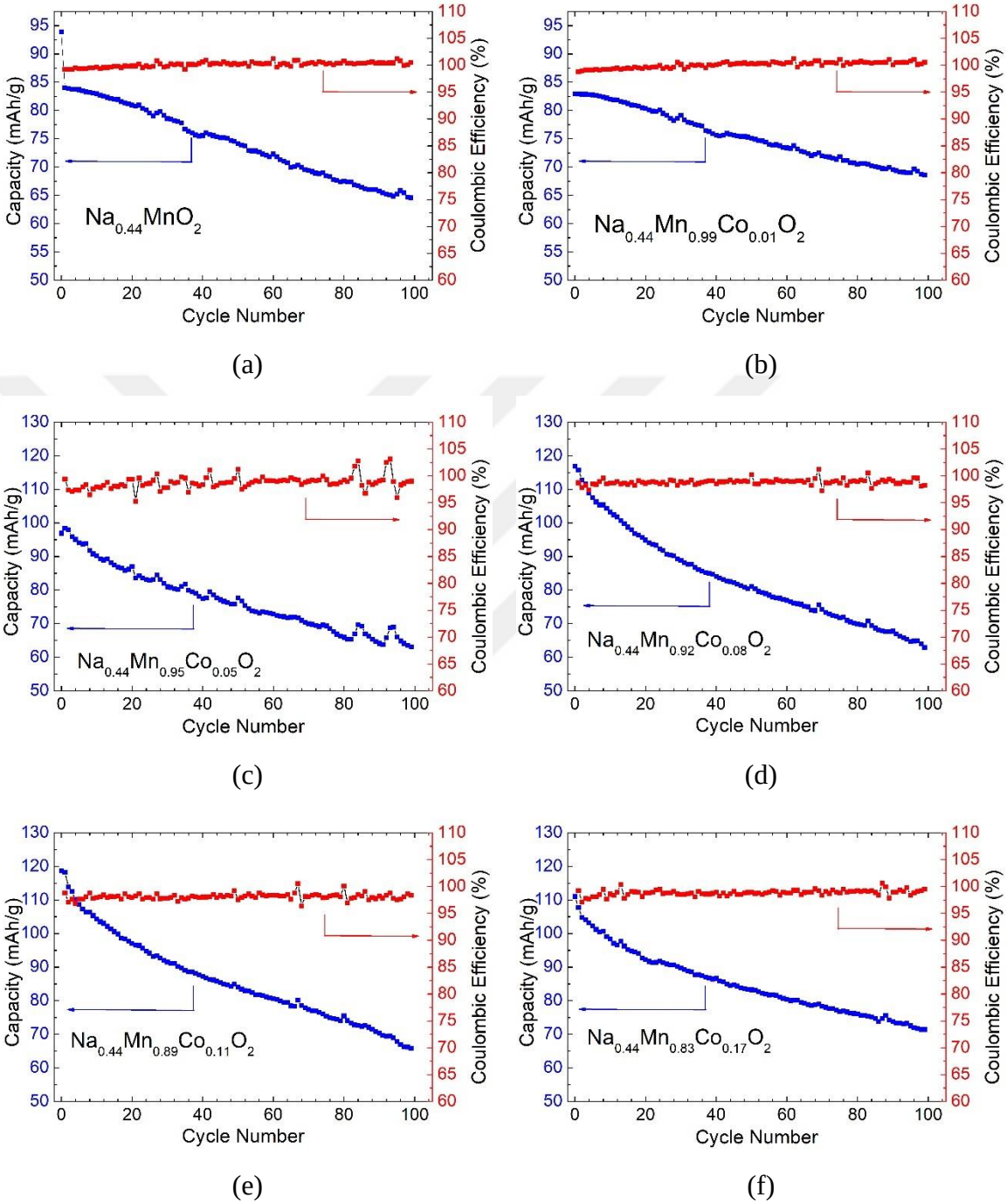

Figure 59. Cyclic performance and coulombic efficiency of $Na_{0.44}Mn_{1-x}Co_xO_2$ samples. (a) x=0, (b) x=0.01, (c) x=0.05, (d) x=0.08, (e) x=0.11 and (f) x=0.17.

The rate performances of $Na_{0.44}Mn_{1-x}Co_xO_2$ samples in 2.0–4.0 V at various current densities are shown in Figure 60. The rate of x = 0, x = 0.01, and x = 0.05 at the location of the tunnel structure is reasonably close. This result shows that the P-type

structure found in the x = 0.01 and x = 0.05 samples has no negative effect on discharge performance. Additionally, it was observed that x = 0.08, x = 0.11, and x = 0.17 samples with high prevalence of P-type crystal structure showed high rate performances. Accordingly, these samples can be considered as promising positive-electrode candidates for Sodium batteries. Table 6 shows the average discharge capacities of all samples in specific C rates.

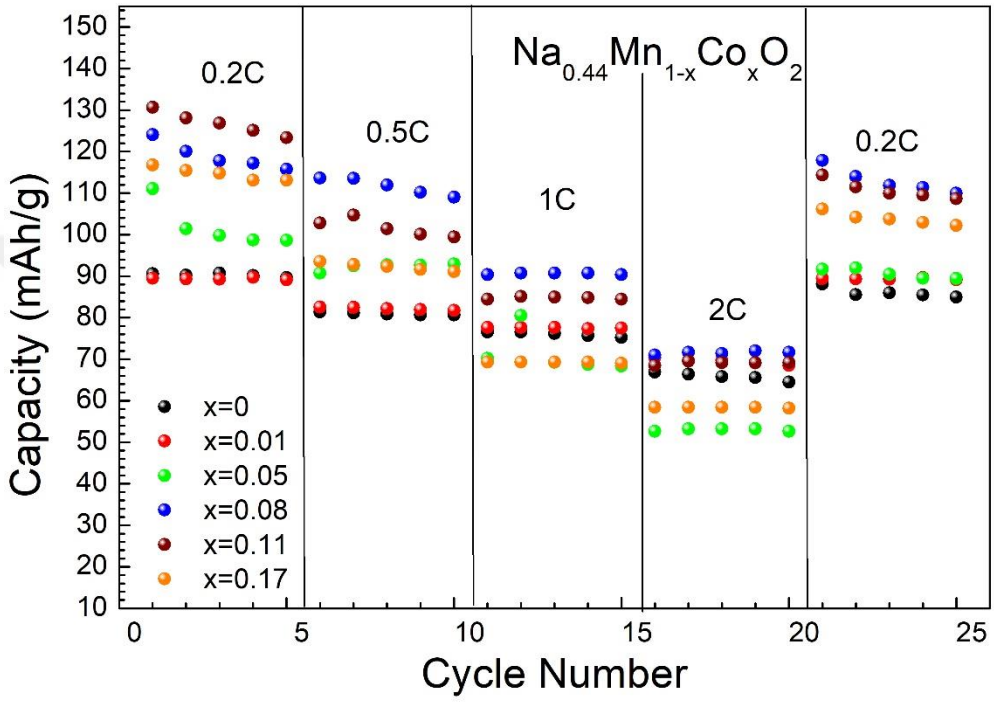

Figure 60. The rate capability of the $Na_{0.44}Mn_{1-x}Co_xO_2$ sample series.

Table 6. Discharge capacities of $Na_{0.44}Mn_{1-x}Co_xO_2$ sample series at different C rates.

Sample	Discharge capacity (mAh/g)			
	0.2C	**0.5C**	**1C**	**2C**
x=0	90	81	75	65
x=0.01	89	82	77	69
x=0.05	100	92	68	53
x=0.08	118	112	90	71
x=0.11	127	104	85	69
x=0.17	115	92	69	58

The charge/discharge curve of the $Na_{0.44}Mn_{1-x}Ni_xO_2$ series over 100 cycles at a 0.3 C current rate can be seen in Figure 61. In contrast to the results of the Co substitution

samples, a multiple plateau structure is also observed in the x = 0.05 with the x = 0.01 sample (Figure 61 (b)(c)); this result is consistent with the structural characterization analysis. In the higher Ni-substituted samples, the multiple plateau structure was almost absent. An important reason for this may be the degradation of the Mn/Ni sites after the Ni substitution. Therefore, the irregularity of the charge/Na order in the structure can be observed. Another important reason is the $Na_{0.7}MnO_{2.05}$ phase is facilitated by the increase in Co substitution rate; it becomes the dominant phase with the increase of this rate.

The initial capacities of the samples x = 0, x = 0.01, and x = 0.05, which have similar discharge profiles, were observed as 84 mAh/g, 82 mAh/g, and 85.2 mAh/g, respectively (Figure 61(a)-(c)). On the other hand, the initial capacities of the x = 0.08, x = 0.11, and x = 0.17, which have different discharge profiles and are dominated by $Na_{0.7}MnO_{2.05}$, are 99.19 mAh/g, 111.5 mAh/g, and 101.8 mAh/g, respectively (Figure 61 (d)-(f)). The reason behind such a high initial capacity is that $Na_{0.7}MnO_{2.05}$ compounds allow for more Na diffusion in the P2-layered structure [145].

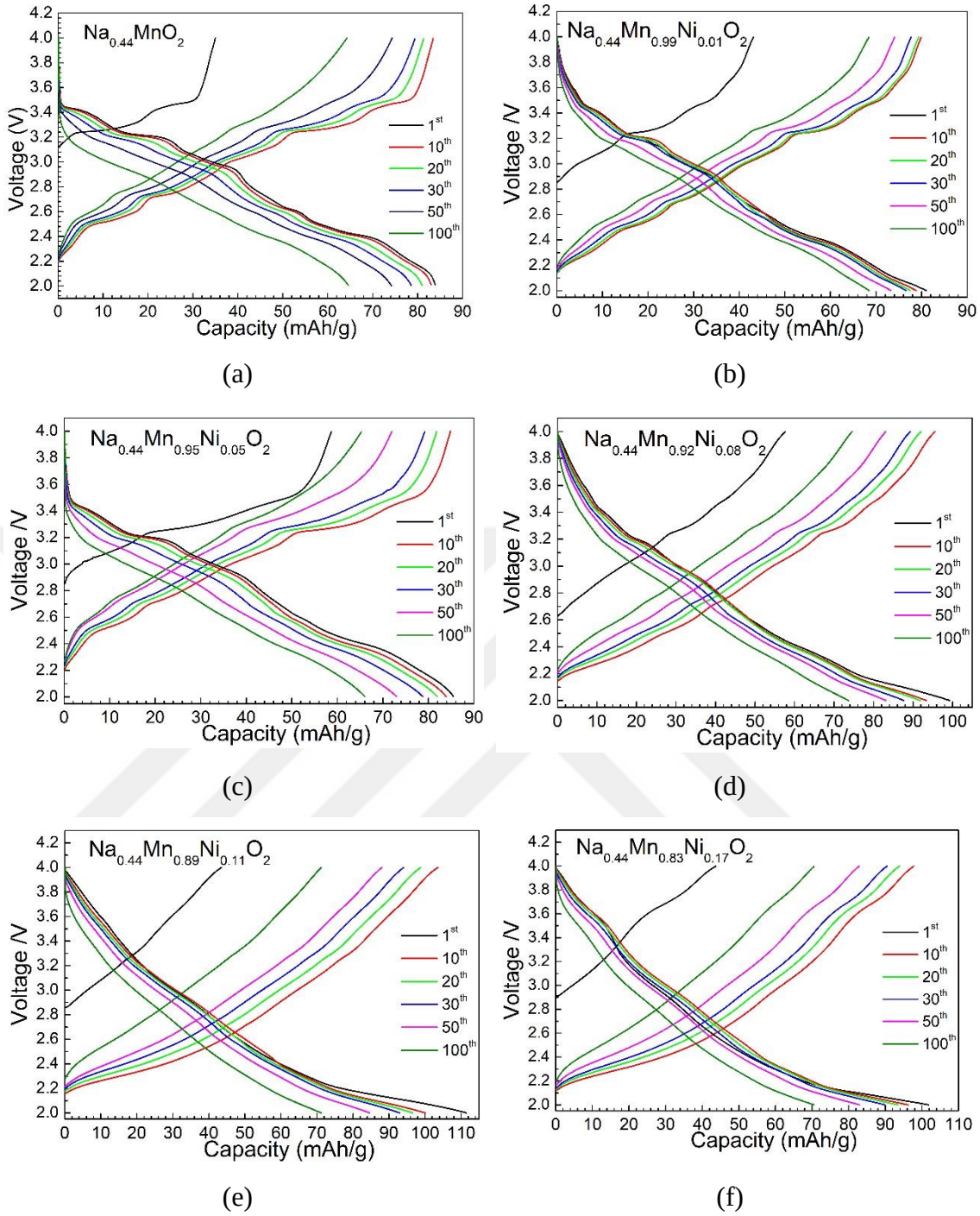

Figure 61. 1st, 10th, 20th, 30th, 50th and 100th discharge/charge curves of $Na_{0.44}Mn_{1-x}Ni_xO_2$ in a 2-4 V voltage window at 0.3C current rate (1 C = 121 mAh) vs Na/Na^+. (a) x=0, (b) x=0.01, (c) x=0.05, (d) x=0.08, (e) x=0.11 and (f) x=0.17.

The cyclic performances and coulombic efficiency over the 100 cycle at a 0.3 C rate of the $Na_{0.44}Mn_{1-x}Ni_xO_2$ series are shown in Figure 62. The fact that coulombic efficiency is close to 100% indicates that all samples display a high level of Na insertion mechanism. However, high coulombic efficiency is not directly related to the capacity efficiency of the samples. The capacity fading of x = 0, x = 0.01, and x = 0.05

samples was calculated as 23%, 13.6%, and 22.7%, respectively. The capacity fading of the samples x = 0.08, x = 0.11 and x = 0.17, where the $Na_{0.7}MnO_{2.05}$ phase was dominant, was calculated as 25.7%, 36.2%, and 30.7%, respectively. Although the JT effect due to Mn^{+3} ions is inevitably present in the $Na_{0.44}MnO_2$, T-type x = 0.01 and x = 0.05 still show high stability.

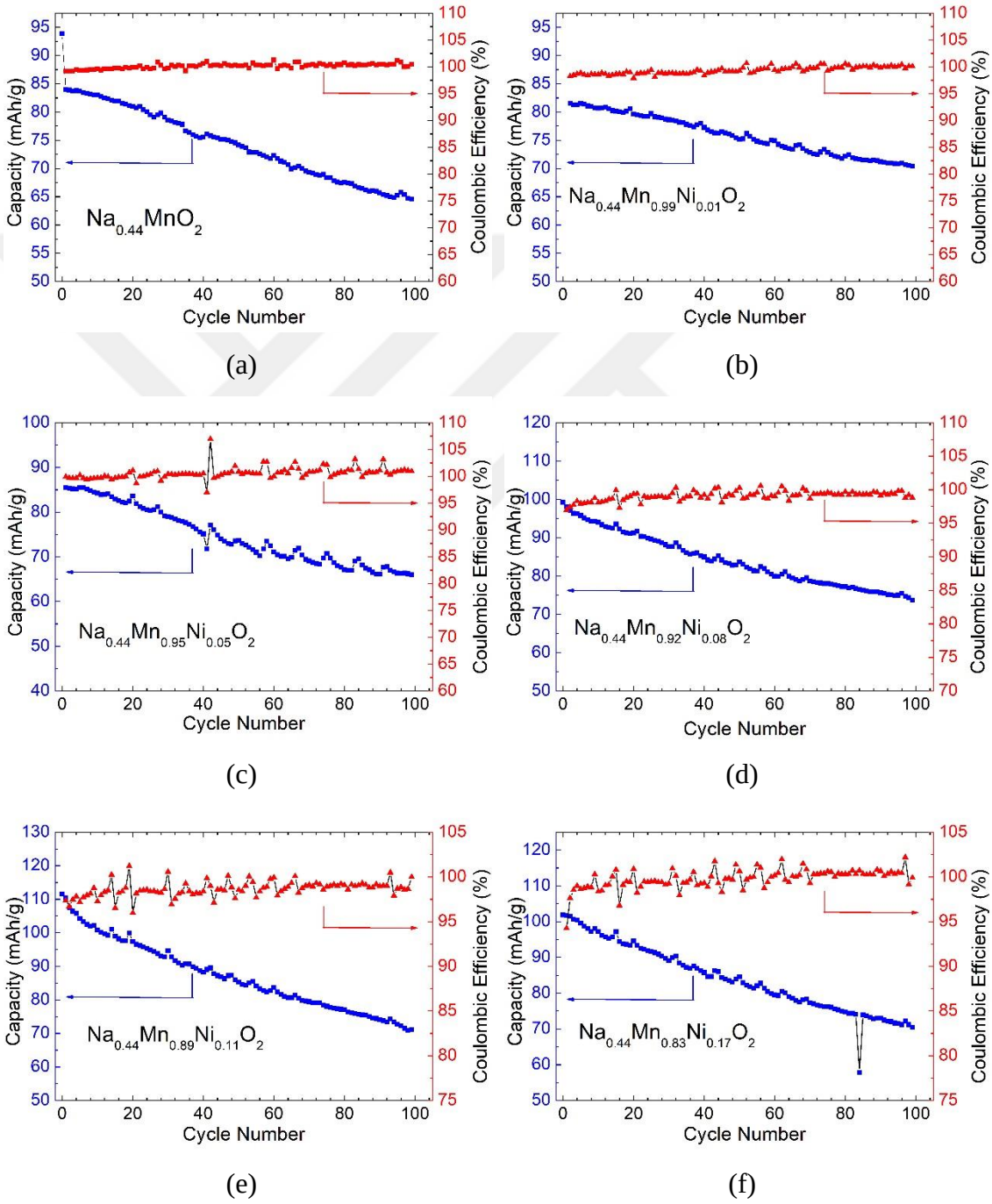

Figure 62. Cyclic performance and coulombic efficiency of $Na_{0.44}Mn_{1-x}Ni_xO_2$ samples. (a) x=0, (b) x=0.01, (c) x=0.05, (d) x=0.08, (e) x=0.11 and (f) x=0.17.

The rate performances of $Na_{0.44}Mn_{1-x}Ni_xO_2$ samples in a 2–4 V window at different C rates are shown in Figure 63. It was observed that all samples maintained their discharge capacity subsequent to high C rates. The high rate performance of the T-type crystal structure is an expected result due to the large diffusion tunnels. On the other hand, the rate performances of x = 0.11 and x = 0.17 samples, where the ratio of the tunnel structure is very low, are remarkable.

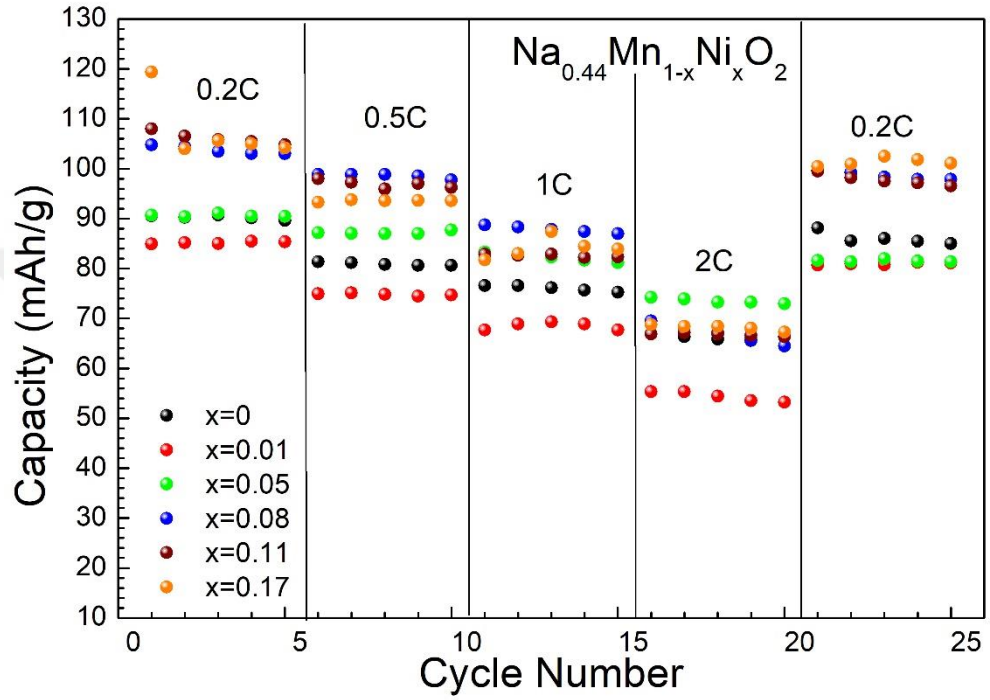

Figure 63. The rate capability of $Na_{0.44}Mn_{1-x}Ni_xO_2$ sample series (1C=121 mA/g).

The average discharge capacities of all samples at 0.2 C, 0.5 C, 1C, and 2 C rates can be seen in Table 7.

Table 7. The average discharge capacities of $Na_{0.44}Mn_{1-x}Ni_xO_2$ sample series at different C rates.

Sample	Discharge capacity (mAh/g)			
	0.2C	**0.5C**	**1C**	**2C**
x=0	90	81	75	65
x=0.01	84	75	69	55
x=0.05	90	86	82	73
x=0.08	104	98	88	68
x=0.11	106	96	82	66
x=0.17	104	93	86	68

The high capacity and high rate performance of these P2 structures makes them promising candidates for longer and more efficient use of Sodium batteries.

It has been reported in previous studies that especially in electrode materials containing Mn^{+3}, JT effect induce the stress on the crystal structure and that causes the structural deformations, amorphization and low reversibility during charge/discharge [183,184]. The data obtained from the magnetism and XAS results show that Mn^{+3} ions decrease in the structure of Co and Ni substituted samples, which leads to a decrease in the JT effect. The capacity retention rates of these Co and Ni doped materials, which can be more stable during long charge / discharge cycles in the crystal structure, have also increased. Among the Co and Ni substitutes, the capacity losses of $Na_{0.44}Mn_{0.99}Co_{0.01}O_2$, $Na_{0.44}Mn_{0.99}Ni_{0.01}O_2$ and $Na_{0.44}Mn_{0.99}Ni_{0.05}O_2$ samples are at the lowest level.

4. CONCLUSIONS

In this paper, the $Na_{0.44}Mn_{1-x}Co_xO_2$ and $Na_{0.44}Mn_{1-x}Ni_xO_2$ series (x = 0, x = 0.01, x = 0.05, x = 0.08, x = 0.11, and x = 0.17) cathode materials were successfully produced by a solid-state reaction method and their physical and electrochemical properties were investigated.

As a result of physical characterization of the $Na_{0.44}Mn_{1-x}Co_xO_2$ samples, it was observed that P2-$Na_{0.58}Mn_{0.5}Co_{0.5}O_2$ structures were formed from the sample x = 0.05 in the Co series, while the tunnel-type structure was completely lost in the x = 0.17 sample. This indicates that Co, which is substituted in the Mn regions, does not consequently substitute the tunnel-type structure observed in x = 0.05. On the other hand, with the increase in Co substitution, the use of Na in the formation of P2-type structures instead of the tunnel-type structure results in the degradation of the $Na_{0.44}MnO_2$ nanorod structures. This degradation is also observed in the SEM and TEM results.

The effects of nanorod form degradation on battery performance have been investigated by electrochemical tests. At this point, the most significant result is provided by the x = 0.01 sample, with the least (%17.25) capacity fade after 100 cycles (Figure 64). Additionally, this sample maintained its structural stability at high current densities from different C rate results. The structural stability of the long cycles in the nanorod form, which is the main target of this study, was obtained in this example.

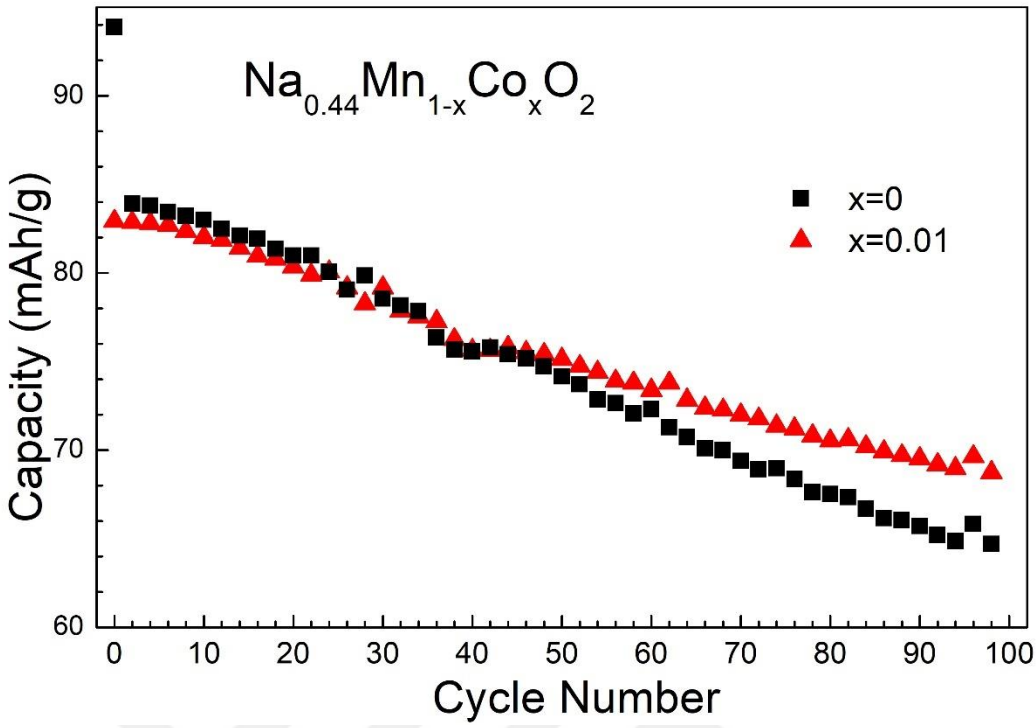

Figure 64. Battery performance of x = 0 and x = 0.01 samples during the 100 cycles at 0.3C.

More interesting results were observed in the other $Na_{0.44}Mn_{1-x}Co_xO_2$ sample series. In contrast with the substitution of Co, the increase of the Ni substitution caused only the $Na_{0.7}MnO_{2.05}$ phase to be considered as the impurity phase in the sample. The nonexistence of any impurities containing Ni indicates that the Ni substitution in Mn sites was successful for the nanorods. On the other hand, the x = 0.01 and x = 0.05 samples in this series were found to have nanorod forms and a lower capacity fade ratio than $Na_{0.44}MnO_2$ (Figure 65).

One of the main reasons for the increase in battery performance is the reduction of Jahn-Teller effect, which is one of the main factors of crystal structure degradation and effective on Mn^{+3} sites, by cobalt and nickel substitution to these sites.

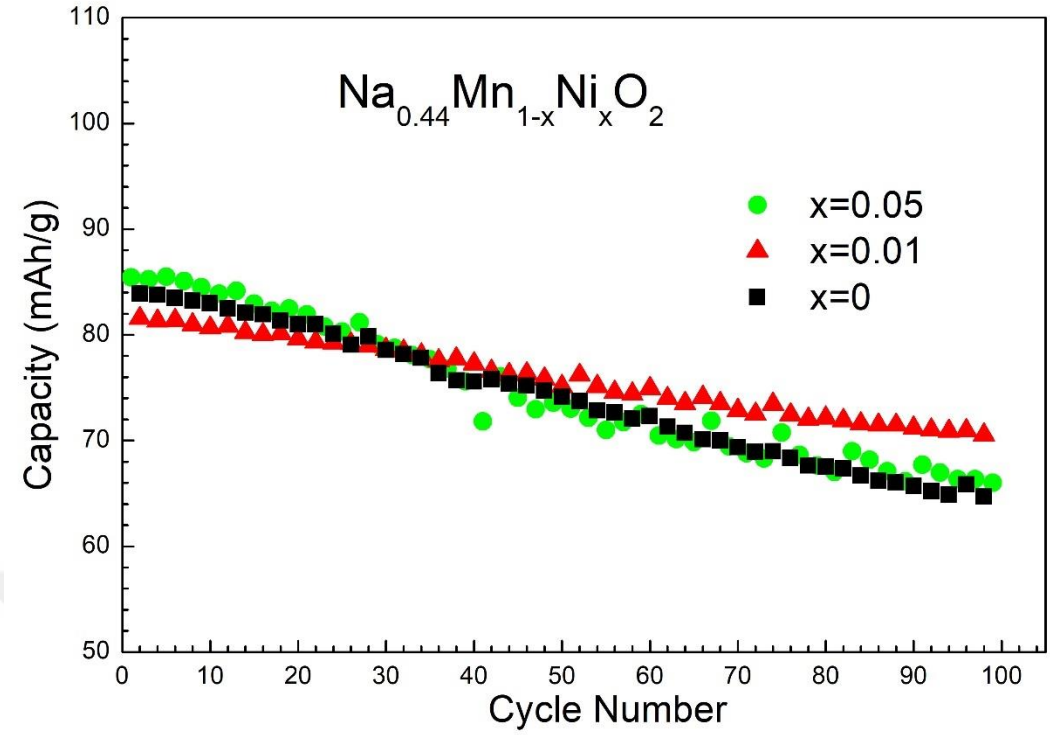

Figure 65. Battery performance of x = 0, x=0.01 and x = 0.05 samples during the 100 cycles at 0.3C.

Table 8 shows a comparison between the electrochemical properties of T-type and P-type positive electrode materials between this work and the literature data. According to the comparison results in Table 8, T-$Na_{0.44}Mn_{0.99}Co_{0.01}O_2$, T-$Na_{0.44}Mn_{0.95}Ni_{0.01}O_2$, and T-$Na_{0.44}Mn_{0.95}Ni_{0.05}O_2$ can be a promising alternative for Na-ion batteries.

Table 8. A comparison of the specific capacities of T-type and P-type cathode materials between this work and the literature data.

Cathode	Specific capacity (mAh/g)	Refs.
T-$Na_{0.54}Mn_{0.50}Ti_{0.51}O_2$	83	[185]
T-$Na_{0.44}Mn_{0.89}Ti_{0.11}O_2$	110	[129]
P2-$Na_xMg_{0.11}Mn_{0.89}O_2$	63	[116]
T-$Na_{0.44}Mn_{0.99}Co_{0.01}O_2$	83.9	
T-$Na_{0.44}Mn_{0.99}Ni_{0.01}O_2$	82	In this work
T-$Na_{0.44}Mn_{0.99}Ni_{0.05}O_2$	85.5	

Using Cobalt and Nickel modified T-$Na_{0.44}Mn_{0.99}Co_{0.01}O_2$, T-$Na_{0.44}Mn_{0.95}Ni_{0.01}O_2$, and T-$Na_{0.44}Mn_{0.95}Ni_{0.05}O_2$, it could be possible to assemble high-energy and high-density Sodium-ion batteries that only consist of the earth's most abundant elements. We believe that these findings enrich the exploration of promising cathode materials that can be used in rechargeable Sodium-ion batteries for large-scale energy storage applications.

5. REFERENCES

[1] V.S. Arunachalam and E.L. Fleischer, *The Global Energy Landscape and Materials Innovation*, **MRS Bull.**, 33:04 (2008) 264–288.

[2] Anonymous. (2018). https://www.ipcc.ch/assessment-report/ar4/ (on-line access on 20 Feb, 2018).

[3] Y. Jiang, Y. Bi, M. Liu, Z. Peng, L. Huai, P. Dong, J. Duan, Z. Chen, X. Li, D. Wang, and Y. Zhang, *Improved stability of Ni-rich cathode by the substitutive cations with stronger bonds*, **Electrochim. Acta**, 268 (2018) 41–48.

[4] F. Hu and X. Jiang, *Li-substituted P2-$Na_{0.66}Li_xMn0.5Ti_{0.5}O_2$ as an advanced cathode material and new "bi-functional" electrode for symmetric sodium-ion batteries*, **Adv. Powder Technol.**, (2018).

[5] H. Chen, Z. He, Z. Huang, L. Song, C. Shen, and J. Liu, *The effects of multifunctional coating on Li-rich cathode material with hollow spherical structure for Li ion battery*, **Ceram. Int.**, 43:12 (2017) 8616–8624.

[6] Z. Liu, B. Liu, P. Guo, X. Shang, M. Lv, D. Liu, and D. He, *Enhanced electrochemical kinetics in lithium-sulfur batteries by using carbon nanofibers/manganese dioxide composite as a bifunctional coating on sulfur cathode*, **Electrochim. Acta**, 269 (2018) 180–187.

[7] C. Karegeya, A. Mahmoud, B. Vertruyen, F. Hatert, R.P. Hermann, R. Cloots, and F. Boschini, *One-step hydrothermal synthesis and electrochemical performance of sodium-manganese-iron phosphate as cathode material for Li-ion batteries*, **J. Solid State Chem.**, 253 (2017) 389–397.

[8] R. Muruganantham, Y.-T. Chiu, C.-C. Yang, C.-W. Wang, and W.-R. Liu, *An Efficient Evaluation of F-doped Polyanion Cathode Materials with Long Cycle Life for Na-Ion Batteries Applications*, **Sci. Rep.**, 7:1 (2017) 14808.

[9] R. Cecchini and G. Pelosi, *Alessandro Volta and his battery*, **IEEE Antennas Propag. Mag.**, 34:2 (1992) 30–37.

[10] C.A. Vincent and B. Scrosati, *Modern Batteries, An Introduction to Electrochemical Power Sources*, Second Edition, *Butterworth-Heinemann*, (1997).

[11] P. Kurzweil, *Gaston Planté and his invention of the lead–acid battery—The genesis of the first practical rechargeable battery*, **J. Power Sources**, 195:14 (2010) 4424–4434.

[12] S. Bergstrom, *Fiftieth Anniversary: Anniversary Issue on Storage Batteries*, **J. Electrochem. Soc.**, 99:9 (1952) 248C.

[13] M. Tliha, C. Khaldi, S. Boussami, N. Fenineche, O. El-Kedim, H. Mathlouthi, and J. Lamloumi, *Kinetic and thermodynamic studies of hydrogen storage alloys as negative electrode materials for Ni/MH batteries: a review*, **J. Solid State Electrochem.**, 18:3 (2014) 577–593.

[14] K. Mizushima, P.C. Jones, P.J. Wiseman, and J.B. Goodenough, *Li_xCoO_2 (0<x<-1): A new cathode material for batteries of high energy density*, **Mater. Res. Bull.**, 15:6 (1980) 783–789.

[15] Anonymous. (2018). https://www.toyota.com/prius/prius-features/ (on-line access on 15 Jun, 2018).

[16] Anonymous. (2018). https://www.reuters.com/article/us-autoshow-tokyo-toyota-battery/toyota-scrambles-to-ready-game-changer-ev-battery-for-mass-market-idUSKBN1CW27Y (on-line access on 15 Jun, 2018).

[17] A. Bhide, J. Hofmann, A. Katharina Dürr, J. Janek, and P. Adelhelm, *Electrochemical stability of non-aqueous electrolytes for sodium-ion batteries and their compatibility with $Na_{0.7}CoO_2$*, **Phys. Chem. Chem. Phys.**, 16:5 (2014) 1987–1998.

[18] A. Ponrouch, R. Dedryvère, D. Monti, A.E. Demet, J.M. Ateba Mba, L. Croguennec, C. Masquelier, P. Johansson, and M.R. Palacín, *Towards high energy density sodium ion batteries through electrolyte optimization*, **Energy Environ. Sci.**, 6:8 (2013) 2361.

[19] A. Ponrouch, E. Marchante, M. Courty, J.-M. Tarascon, and M.R. Palacín, *In search of an optimized electrolyte for Na-ion batteries*, **Energy Environ. Sci.**, 5:9 (2012) 8572.

[20] Y. Xie, H. Zou, H. Xiang, R. Xia, D. Liang, P. Shi, S. Dai, and H. Wang, *Enhancement on the wettability of lithium battery separator toward nonaqueous electrolytes*, **J. Memb. Sci.**, 503 (2016) 25–30.

[21] Principles Determining the Voltages and Capacities of Electrochemical Cells, *in* Adv. Batter., *Springer US*, Boston, MA, pp. 25–39.

[22] P.W. Gruber, P.A. Medina, G.A. Keoleian, S.E. Kesler, M.P. Everson, and T.J. Wallington, *Global Lithium Availability*, **J. Ind. Ecol.**, 15:5 (2011) 760–775.

[23] N.T. Nassar, T.E. Graedel, and E.M. Harper, *By-product metals are technologically essential but have problematic supply*, **Sci. Adv.**, 1:3 (2015) e1400180.

[24] V. Sironval, L. Reylandt, P. Chaurand, S. Ibouraadaten, M. Palmai-Pallag, Y. Yakoub, B. Ucakar, J. Rose, C. Poleunis, R. Vanbever, E. Marbaix, D. Lison, and S. van den Brule, *Respiratory hazard of Li-ion battery components: elective toxicity of lithium cobalt oxide ($LiCoO_2$) particles in a mouse bioassay*, **Arch. Toxicol.**, 92:5 (2018) 1673–1684.

[25] J.-J. Braconnier, C. Delmas, C. Fouassier, and P. Hagenmuller, *Comportement electrochimique des phases Na_xCoO_2*, **Mater. Res. Bull.**, 15:12 (1980) 1797–1804.

[26] P. Adelhelm, P. Hartmann, C.L. Bender, M. Busche, C. Eufinger, and J. Janek, *From lithium to sodium: cell chemistry of room temperature sodium–air and sodium–sulfur batteries*, **Beilstein J. Nanotechnol.**, 6 (2015) 1016–1055.

[27] K. Kubota, N. Yabuuchi, H. Yoshida, M. Dahbi, and S. Komaba, *Layered oxides as positive electrode materials for Na-ion batteries*, **MRS Bull.**, 39:5 (2014) 416–422.

[28] Y. Ma, *Rechargeable Na/Na_xCoO_2 and $Na_{15}Pb_4/Na_xCoO_2$ Polymer Electrolyte Cells*, **J. Electrochem. Soc.**, 140:10 (2006) 2726.

[29] N. Yabuuchi, K. Kubota, M. Dahbi, and S. Komaba, *Research Development on Sodium-Ion Batteries*, **Chem. Rev.**, 114:23 (2014) 11636–11682.

[30] D.P. DiVincenzo and E.J. Mele, *Cohesion and structure in stage-1 graphite intercalation compounds*, **Phys. Rev. B**, 32:4 (1985) 2538–2553.

[31] R. Alcántara, J.M. Jiménez-Mateos, P. Lavela, and J.L. Tirado, *Carbon black: a promising electrode material for sodium-ion batteries*, **Electrochem. Commun.**, 3:11 (2001) 639–642.

[32] L. Baggetto, P. Ganesh, R.P. Meisner, R.R. Unocic, J.-C. Jumas, C.A. Bridges, and G.M. Veith, *Characterization of sodium ion electrochemical reaction with tin anodes: Experiment and theory*, **J. Power Sources**, 234 (2013) 48–59.

[33] S.A. Webb, L. Baggetto, C.A. Bridges, and G.M. Veith, *The electrochemical reactions of pure indium with Li and Na: Anomalous electrolyte decomposition, benefits of FEC additive, phase transitions and electrode performance*, **J. Power Sources**, 248 (2014) 1105–1117.

[34] J.-Y. Hwang, S.-T. Myung, and Y.-K. Sun, *Sodium-ion batteries: present and future*, **Chem. Soc. Rev.**, 46:12 (2017) 3529–3614.

[35] G.H. Newman and L.P. Klemann, *Ambient Temperature Cycling of an Na-TiS_2 Cell*, **J. Electrochem. Soc.**, 127:10 (1980) 2097.

[36] R. Berthelot, D. Carlier, and C. Delmas, *Electrochemical investigation of the P2–Na_xCoO_2 phase diagram*, **Nat. Mater.**, 10:1 (2011) 74–80.

[37] D. Su, H.-J. Ahn, and G. Wang, *β-MnO_2 nanorods with exposed tunnel structures as high-performance cathode materials for sodium-ion batteries*, **NPG Asia Mater.**, 5:11 (2013) e70–e70.

[38] V. Dall'Asta, D. Buchholz, L.G. Chagas, X. Dou, C. Ferrara, E. Quartarone, C. Tealdi, and S. Passerini, *Aqueous Processing of $Na_{0.44}MnO_2$ Cathode Material for the Development of Greener Na-Ion Batteries*, **ACS Appl. Mater.**

Interfaces, 9 :40 (2017) 34891–34899.

[39] M. D'Arienzo, R. Ruffo, R. Scotti, F. Morazzoni, C.M. Mari, and S. Polizzi, *Layered $Na_{0.71}CoO_2$: a powerful candidate for viable and high performance Na-batteries*, **Phys. Chem. Chem. Phys.**, 14:17 (2012) 5945.

[40] Q. Li, Z. Yao, J. Wu, S. Mitra, S. Hao, T.S. Sahu, Y. Li, C. Wolverton, and V.P. Dravid, *Intermediate phases in sodium intercalation into MoS_2 nanosheets and their implications for sodium-ion batteries*, **Nano Energy**, 38 (2017) 342–349.

[41] Y.H. Jung, C.H. Lim, J.-H. Kim, and D.K. Kim, *$Na_2FeP_2O_7$ as a positive electrode material for rechargeable aqueous sodium-ion batteries*, **RSC Adv.**, 4:19 (2014) 9799.

[42] L. Chen, M. Fiore, J.E. Wang, R. Ruffo, D.-K. Kim, and G. Longoni, *Readiness Level of Sodium-Ion Battery Technology: A Materials Review*, **Adv. Sustain. Syst.**, 2:3 (2018) 1700153.

[43] W. Deng, X. Liang, X. Wu, J. Qian, Y. Cao, X. Ai, J. Feng, and H. Yang, *A low cost, all-organic Na-ion battery based on polymeric cathode and anode*, **Sci. Rep.**, 3 (2013) 2671.

[44] Z. Song, Y. Qian, T. Zhang, M. Otani, and H. Zhou, *Poly(benzoquinonyl sulfide) as a High-Energy Organic Cathode for Rechargeable Li and Na Batteries*, **Adv. Sci. (Weinheim, Baden-Wurttemberg, Ger.**, 2:9 (2015) 1500124.

[45] X. Ma, H. Chen, and G. Ceder, *Electrochemical Properties of Monoclinic $NaMnO_2$*, **J. Electrochem. Soc.**, 158:12 (2011) A1307.

[46] D. Su, H.-J. Ahn, and G. Wang, *Hydrothermal synthesis of α-MnO_2 and β-MnO_2 nanorods as high capacity cathode materials for sodium ion batteries*, **J. Mater. Chem. A**, 1:15 (2013) 4845.

[47] J. Zhang, B. Su, A. Kitajou, M. Fujita, Y. Cui, M. Oda, W. Zhou, P.H.-L. Sit, and D.Y.W. Yu, *Activating abnormal capacity in stoichiometric $NaVO_3$ as cathode material for sodium-ion battery*, **J. Power Sources**, 400 (2018) 377–382.

[48] H. Wang, W. Li, H. Fei, L. Guo, J. Feng, L. Ci, and S. Xiong, *Facile hydrothermal growth of VO_2 nanowire, nanorod and nanosheet arrays as binder free cathode materials for sodium batteries*, **RSC Adv.**, 6:17 (2016) 14314–14320.

[49] C. Delmas, Y. Borthomieu, C. Faure, A. Delahaye, and M. Figlarz, *Nickel hydroxide and derived phases obtained by chimie douce from $NaNiO_2$*, **Solid State Ionics**, 32–33 (1989) 104–111.

[50] J. Zhao, L. Zhao, N. Dimov, S. Okada, and T. Nishida, *Electrochemical and Thermal Properties of α-$NaFeO_2$ Cathode for Na-Ion Batteries*, **J. Electrochem. Soc.**, 160:5 (2013) A3077–A3081.

[51] S.B. Hong, J.-M. Jeong, H.G. Kang, D. Seo, Y. Cha, H. Jeon, G.Y. Lee, M. Irshad, D.H. Kim, S.Y. Hwang, J.W. Kim, and B.G. Choi, *Fast and Scalable Hydrodynamic Synthesis of MnO_2 /Defect-Free Graphene Nanocomposites with High Rate Capability and Long Cycle Life*, **ACS Appl. Mater. Interfaces**, 10:41 (2018) 35250–35259.

[52] C.M. Julien, A. Mauger, C.M. Julien, and A. Mauger, *Nanostructured MnO_2 as Electrode Materials for Energy Storage*, **Nanomaterials**, 7:11 (2017) 396.

[53] L. Della Puppa, M. Komárek, F. Bordas, J.-C. Bollinger, and E. Joussein, *Adsorption of copper, cadmium, lead and zinc onto a synthetic manganese oxide*, **J. Colloid Interface Sci.**, 399 (2013) 99–106.

[54] M.G. Walter, E.L. Warren, J.R. McKone, S.W. Boettcher, Q. Mi, E.A. Santori, and N.S. Lewis, *Solar Water Splitting Cells*, **Chem. Rev.**, 110:11 (2010) 6446–6473.

[55] J. Liu, L. Meng, Z. Fei, P.J. Dyson, X. Jing, and X. Liu, *MnO_2 nanosheets as an artificial enzyme to mimic oxidase for rapid and sensitive detection of glutathione*, **Biosens. Bioelectron.**, 90 (2017) 69–74.

[56] H.-J. Cui, H.-Z. Huang, M.-L. Fu, B.-L. Yuan, and W. Pearl, *Facile synthesis and catalytic properties of single crystalline β-MnO_2 nanorods*, **Catal. Commun.**, 12:14 (2011) 1339–1343.

[57] Y. Hou, Y. Cheng, T. Hobson, and J. Liu, *Design and Synthesis of Hierarchical MnO_2 Nanospheres/Carbon Nanotubes/Conducting Polymer Ternary Composite for High Performance Electrochemical Electrodes*, **Nano Lett.**, 10:7 (2010) 2727–2733.

[58] J. Luo, H.T. Zhu, H.M. Fan, J.K. Liang, H.L. Shi, G.H. Rao, J.B. Li, Z.M. Du, and Z.X. Shen, *Synthesis of Single-Crystal Tetragonal α-MnO_2 Nanotubes*, **J. Phys. Chem. C**, 112:33 (2008) 12594–12598.

[59] Ning Wang, Xia Cao, Lin He, Wei Zhang, Lin Guo, Chinping Chen, A. Rongming Wang, and ǁ Shihe Yang, *One-Pot Synthesis of Highly Crystallined λ-MnO_2 Nanodisks Assembled from Nanoparticles: Morphology Evolutions and Phase Transitions*, **J. Phys. Chem. C**, 112:2 (2008) 365–369.

[60] C. Julien, M. Massot, and C. Poinsignon, *Lattice vibrations of manganese oxides: Part I Periodic structures*, **Spectrochim. Acta Part A Mol. Biomol. Spectrosc.**, 60:3 (2004) 689–700.

[61] J.C. Nardi, *Characterization of the Li/MnO_2 Multistep Discharge*, **J. Electrochem. Soc.**, 132:8 (2006) 1787.

[62] S. Song, S. Jiang, R. Rao, H. Yang, and A. Zhang, *Bicomponent VO_2-defects/MWCNT catalyst for hydroxylation of benzene to phenol: Promoter effect of defects on catalytic performance*, **Appl. Catal. A Gen.**, 401:1–2 (2011) 215–219.

[63] E. Strelcov, Y. Lilach, and A. Kolmakov, *Gas Sensor Based on Metal−Insulator Transition in VO_2 Nanowire Thermistor*, **Nano Lett.**, 9:6 (2009) 2322–2326.

[64] L. Fan, Y. Chen, Q. Liu, S. Chen, L. Zhu, Q. Meng, B. Wang, Q. Zhang, H. Ren, and C. Zou, *Infrared Response and Optoelectronic Memory Device Fabrication Based on Epitaxial VO_2 Film*, **ACS Appl. Mater. Interfaces**, 8:48 (2016) 32971–32977.

[65] M. Lübke, N. Ding, M.J. Powell, D.J.L. Brett, P.R. Shearing, Z. Liu, and J.A. Darr, *VO_2 nano-sheet negative electrodes for lithium-ion batteries*, **Electrochem. Commun.**, 64 (2016) 56–60.

[66] S. Park, C.W. Lee, J.-C. Kim, H.J. Song, H.-W. Shim, S. Lee, and D.-W. Kim, *Heteroepitaxy-Induced Rutile VO_2 with Abundantly Exposed (002) Facets for High Lithium Electroactivity*, **ACS Energy Lett.**, 1:1 (2016) 216–224.

[67] J.M. Booth and P.S. Casey, *Production of VO_2M_1 and M_2 Nanoparticles and Composites and the Influence of the Substrate on the Structural Phase Transition*, **ACS Appl. Mater. Interfaces**, 1:9 (2009) 1899–1905.

[68] W. Jiang, J. Ni, K. Yu, and Z. Zhu, *Hydrothermal synthesis and electrochemical characterization of VO_2 (B) with controlled crystal structures*, **Appl. Surf. Sci.**, 257:8 (2011) 3253–3258.

[69] X. Hu, Z. Zhao, L. Wang, J. Li, C. Wang, Y. Zhao, and H. Jin, *VO_2 (A)/graphene nanostructure: Stand up to Na ion intercalation/deintercalation for enhanced electrochemical performance as a Na-ion battery cathode*, **Electrochim. Acta**, 293 (2019) 97–104.

[70] H. Fei, X. Ding, M. Wei, and K. Wei, *Facile synthesis of Montroseite VOOH, Paramontroseite VO_2 and V_2O_3-VO_2 carbonaceous core-shell microspheres*, **Solid State Sci.**, 13:11 (2011) 2049–2054.

[71] F. Zhou, X. Zhao, H. Xu, and C. Yuan, *Hydrothermal Synthesis of Metastable VO_2 Nanorods as Cathode Materials for Lithium Ion Batteries*, **Chem. Lett.**, 35:11 (2006) 1280–1281.

[72] P.D. Bhuyan, S.K. Gupta, A. Kumar, Y. Sonvane, and P.N. Gajjar, *Highly infrared sensitive VO_2 nanowires for a nano-optical device*, **Phys. Chem. Chem. Phys.**, 20:16 (2018) 11109–11115.

[73] R. Li and C.-Y. Liu, *VO_2(B) nanospheres: Hydrothermal synthesis and electrochemical properties*, **Mater. Res. Bull.**, 45:6 (2010) 688–692.

[74] Ying Wang, Katsunori Takahashi, and Huamei Shang, and Guozhong Cao, *Synthesis and Electrochemical Properties of Vanadium Pentoxide Nanotube Arrays*, **J. Phys. Chem. B**, 109:8 (2005) 3085–3088.

[75] S.Y. Chew, C. Feng, S.H. Ng, J. Wang, Z. Guo, and H. Liu, *Low-Temperature Synthesis of Polypyrrole-Coated LiV_3O_8 Composite with Enhanced Electrochemical Properties*, **J. Electrochem. Soc.**, 154:7 (2007) A633.

[76] E. Baudrin, G. Sudant, D. Larcher, B. Dunn, and J.M. Tarascon, *Preparation of nanotextured VO_2[B] from vanadium oxide aerogels*, **Chem. Mater.**, 18:18 (2006) 4369–4374.

[77] W. Wang, B. Jiang, L. Hu, Z. Lin, J. Hou, and S. Jiao, *Single crystalline VO_2 nanosheets: A cathode material for sodium-ion batteries with high rate cycling performance*, **J. Power Sources**, 250 (2014) 181–187.

[78] S. Tepavcevic, H. Xiong, V.R. Stamenkovic, X. Zuo, M. Balasubramanian, V.B. Prakapenka, C.S. Johnson, and T. Rajh, *Nanostructured Bilayered Vanadium Oxide Electrodes for Rechargeable Sodium-Ion Batteries*, **ACS Nano**, 6:1 (2012) 530–538.

[79] D. Su and G. Wang, *Single-Crystalline Bilayered V_2O_5 Nanobelts for High-Capacity Sodium-Ion Batteries*, **ACS Nano**, 7:12 (2013) 11218–11226.

[80] C.J. Patrissi and C.R. Martin, *Sol-Gel-Based Template Synthesis and Li-Insertion Rate Performance of Nanostructured Vanadium Pentoxide*, **J. Electrochem. Soc.**, 146:9 (1999) 3176.

[81] T. Zhai, H. Liu, H. Li, X. Fang, M. Liao, L. Li, H. Zhou, Y. Koide, Y. Bando, and D. Golberg, *Centimeter-Long V_2O_5 Nanowires: From Synthesis to Field-Emission, Electrochemical, Electrical Transport, and Photoconductive Properties*, **Adv. Mater.**, 22:23 (2010) 2547–2552.

[82] Y.L. Cheah, N. Gupta, S.S. Pramana, V. Aravindan, G. Wee, and M. Srinivasan, *Morphology, structure and electrochemical properties of single phase electrospun vanadium pentoxide nanofibers for lithium ion batteries*, **J. Power Sources**, 196:15 (2011) 6465–6472.

[83] Q. Wei, J. Liu, W. Feng, J. Sheng, X. Tian, L. He, Q. An, and L. Mai, *Hydrated vanadium pentoxide with superior sodium storage capacity*, **J. Mater. Chem. A**, 3:15 (2015) 8070–8075.

[84] V. Raju, J. Rains, C. Gates, W. Luo, X. Wang, W.F. Stickle, G.D. Stucky, and X. Ji, *Superior Cathode of Sodium-Ion Batteries: Orthorhombic V_2O_5 Nanoparticles Generated in Nanoporous Carbon by Ambient Hydrolysis Deposition*, **Nano Lett.**, 14:7 (2014) 4119–4124.

[85] L.D. Dyer, B.S. Borie, and G.P. Smith, *Alkali Metal-Nickel Oxides of the Type $MNiO_2$*, **J. Am. Chem. Soc.**, 76:6 (1954) 1499–1503.

[86] J. Molenda and A. StokŁlosa, *Electronic and electrochemical properties of nickel bronze, Na_xNiO_2*, **Solid State Ionics**, 38:1–2 (1990) 1–4.

[87] P. Vassilaras, X. Ma, X. Li, and G. Ceder, *Electrochemical Properties of Monoclinic $NaNiO_2$*, **J. Electrochem. Soc.**, 160:2 (2013) A207–A211.

[88] L. Wang, M. Wang, and D. Zhao, *Thermoelectric properties of c-axis oriented Ni-substituted $NaCoO_2$ thermoelectric oxide by the citric acid complex method*, **J. Alloys Compd.**, 471:1–2 (2009) 519–523.

[89] E. Altin, E. Oz, S. Demirel, and A. Bayri, *Magnetic and thermoelectric properties of B-substituted $NaCoO_2$*, **Appl. Phys. A**, 119:3 (2015) 1187–1196.

[90] Y. Takahashi, Y. Gotoh, and J. Akimoto, *Single-crystal growth, crystal and electronic structure of $NaCoO_2$*, **J. Solid State Chem.**, 172:1 (2003) 22–26.

[91] Z. Dai, U. Mani, H.T. Tan, and Q. Yan, *Advanced Cathode Materials for Sodium-Ion Batteries: What Determines Our Choices?*, **Small Methods**, 1:5 (2017) 1700098.

[92] M. Jansen and R. Hoppe, *Neue Oxocobaltate*, **Naturwissenschaften**, 59:5 (1972) 215–215.

[93] C. Fouassier, G. Matejka, J.-M. Reau, and P. Hagenmuller, *Sur de nouveaux bronzes oxygénés de formule $Na_\chi CoO_2$ (χ1) Le système cobalt-oxygène-sodium*, **J. Solid State Chem.**, 6:4 (1973) 532–537.

[94] S.-W. Kim, D.-H. Seo, X. Ma, G. Ceder, and K. Kang, *Electrode Materials for Rechargeable Sodium-Ion Batteries: Potential Alternatives to Current Lithium-Ion Batteries*, **Adv. Energy Mater.**, 2:7 (2012) 710–721.

[95] Y. Lei, X. Li, L. Liu, and G. Ceder, *Synthesis and Stoichiometry of Different Layered Sodium Cobalt Oxides*, **Chem. Mater.**, 26:18 (2014) 5288–5296.

[96] L.W. Shacklette, T.R. Jow, and L. Townsend, *Rechargeable Electrodes from Sodium Cobalt Bronzes*, **J. Electrochem. Soc.**, 135:11 (1988) 2669.

[97] J.J. Ding, Y.N. Zhou, Q. Sun, X.Q. Yu, X.Q. Yang, and Z.W. Fu, *Electrochemical properties of P2-phase $Na_{0.74}CoO_2$ compounds as cathode material for rechargeable sodium-ion batteries*, **Electrochim. Acta**, 87 (2013) 388–393.

[98] A. Bhide and K. Hariharan, *Physicochemical properties of Na_xCoO_2 as a cathode for solid state sodium battery*, **Solid State Ionics**, 192:1 (2011) 360–363.

[99] J.P. Parant, R. Olazcuaga, M. Devalette, C. Fouassier, and P. Hagenmuller, *Sur quelques nouvelles phases de formule Na_xMnO_2 ($x \leq 1$)*, **J. Solid State Chem.**, 3:1 (1971) 1–11.

[100] R.J. Clément, P.G. Bruce, and C.P. Grey, *Review—Manganese-Based P2-Type Transition Metal Oxides as Sodium-Ion Battery Cathode Materials*, **J. Electrochem. Soc.**, 162:14 (2015) A2589–A2604.

[101] C. Luo, A. Langrock, X. Fan, Y. Liang, and C. Wang, *P2-type transition metal oxides for high performance Na-ion battery cathodes*, **J. Mater. Chem. A**, 5 :34 (2017) 18214–18220.

[102] D.F. Shriver and P.W. Atkins, *Inorganic chemistry*, 3rd ed., *W.H. Freeman and Co*, New York, (1999).

[103] R.J. Clément, J. Billaud, A. Robert Armstrong, G. Singh, T. Rojo, P.G. Bruce, and C.P. Grey, *Structurally stable Mg-doped P2-$Na_{2/3}Mn_{1-y}Mg_yO_2$ sodium-ion battery cathodes with high rate performance: insights from electrochemical, NMR and diffraction studies*, **Energy Environ. Sci.**, 9:10 (2016) 3240–3251.

[104] Y. Liu, X. Fang, A. Zhang, C. Shen, Q. Liu, H.A. Enaya, and C. Zhou, *Layered P2-$Na_{2/3}[Ni_{1/3}Mn_{2/3}]O_2$ as high-voltage cathode for sodium-ion batteries: The capacity decay mechanism and Al_2O_3 surface modification*, **Nano Energy**, 27 (2016) 27–34.

[105] A. Mendiboure, C. Delmas, and P. Hagenmuller, *Electrochemical intercalation and deintercalation of Na_xMnO_2 bronzes*, **J. Solid State Chem.**, 57:3 (1985) 323–331.

[106] J. Billaud, R.J. Clément, A.R. Armstrong, J. Canales-Vázquez, P. Rozier, C.P. Grey, and P.G. Bruce, *β-$NaMnO_2$: A High-Performance Cathode for Sodium-Ion Batteries*, **J. Am. Chem. Soc.**, 136:49 (2014) 17243–17248.

[107] C.-Y. Yu, J.-S. Park, H.-G. Jung, K.-Y. Chung, D. Aurbach, Y.-K. Sun, and S.-T. Myung, *$NaCrO_2$ cathode for high-rate sodium-ion batteries*, **Energy Environ. Sci.**, 8:7 (2015) 2019–2026.

[108] X. Wang, Y. Gao, X. Shen, Y. Li, Q. Kong, S. Lee, Z. Wang, R. Yu, Y.-S. Hu, and L. Chen, *Anti-P2 structured $Na_{0.5}NbO_2$ and its negative strain effect*, **Energy Environ. Sci.**, 8:9 (2015) 2753–2759.

[109] K. Baroudi, C. Yim, H. Wu, Q. Huang, J.H. Roudebush, E. Vavilova, H.-J. Grafe, V. Kataev, B. Buechner, H. Ji, C. Kuo, Z. Hu, T.-W. Pi, C. Pao, J. Lee, D. Mikhailova, L. Hao Tjeng, and R.J. Cava, *Structure and properties of α-$NaFeO_2$-type ternary sodium iridates*, **J. Solid State Chem.**, 210:1 (2014) 195–205.

[110] Y. Takeda, K. Nakahara, M. Nishijima, N. Imanishi, O. Yamamoto, M. Takano, and R. Kanno, *Sodium deintercalation from sodium iron oxide*, **Mater. Res. Bull.**, 29:6 (1994) 659–666.

[111] J.-Y. Hwang, S.-M. Oh, S.-T. Myung, K.Y. Chung, I. Belharouak, and Y.-K. Sun, *Radially aligned hierarchical columnar structure as a cathode material for high energy density sodium-ion batteries*, **Nat. Commun.**, 6:1 (2015) 6865.

[112] S. Guo, P. Liu, Y. Sun, K. Zhu, J. Yi, M. Chen, M. Ishida, and H. Zhou, *A High-Voltage and Ultralong-Life Sodium Full Cell for Stationary Energy Storage*, **Angew. Chemie Int. Ed.**, 54:40 (2015) 11701–11705.

[113] M.H. Han, E. Gonzalo, N. Sharma, J.M. López del Amo, M. Armand, M. Avdeev, J.J. Saiz Garitaonandia, and T. Rojo, *High-Performance P2-Phase Na $_{2/3}$ Mn $_{08}$ Fe $_{01}$ Ti $_{01}$ O $_{2}$ Cathode Material for Ambient-Temperature Sodium-Ion Batteries*, **Chem. Mater.**, 28:1 (2016) 106–116.

[114] S. Kalluri, K.H. Seng, W.K. Pang, Z. Guo, Z. Chen, H.-K. Liu, and S.X. Dou, *Electrospun P2-type Na $_{2/3}$ (Fe $_{1/2}$ Mn $_{1/2}$)O $_{2}$ Hierarchical Nanofibers as Cathode Material for Sodium-Ion Batteries*, **ACS Appl. Mater. Interfaces**, 6:12 (2014) 8953–8958.

[115] J. Ma, S.-H. Bo, L. Wu, Y. Zhu, C.P. Grey, and P.G. Khalifah, *Ordered and Disordered Polymorphs of Na(Ni $_{2/3}$ Sb $_{1/3}$)O $_{2}$: Honeycomb-Ordered Cathodes for Na-Ion Batteries*, **Chem. Mater.**, 27:7 (2015) 2387–2399.

[116] D. Buchholz, C. Vaalma, L.G. Chagas, and S. Passerini, *Mg-doping for improved long-term cyclability of layered Na-ion cathode materials – The example of P2-type $Na_xMg_{0.11}Mn_{0.89}O_2$*, **J. Power Sources**, 282 (2015) 581–585.

[117] J. Billaud, G. Singh, A.R. Armstrong, E. Gonzalo, V. Roddatis, M. Armand, T. Rojo, and P.G. Bruce, *$Na_{0.67}Mn_{1-x}Mg_xO_2$ ($0 \leq x \leq 02$): a high capacity cathode for sodium-ion batteries*, **Energy Environ. Sci.**, 7:4 (2014) 1387–1391.

[118] D. Yuan, W. He, F. Pei, F. Wu, Y. Wu, J. Qian, Y. Cao, X. Ai, and H. Yang, *Synthesis and electrochemical behaviors of layered $Na_{0.67}[Mn_{0.65}Co_{0.2}Ni_{0.15}]O_2$ microflakes as a stable cathode material for sodium-ion batteries*, **J. Mater. Chem. A**, 1:12 (2013) 3895.

[119] D. Buchholz, L.G. Chagas, M. Winter, and S. Passerini, *P2-type layered $Na_{0.45}Ni_{0.22}Co_{0.11}Mn_{0.66}O_2$ as intercalation host material for lithium and sodium batteries*, **Electrochim. Acta**, 110 (2013) 208–213.

[120] H. Yoshida, N. Yabuuchi, K. Kubota, I. Ikeuchi, A. Garsuch, M. Schulz-Dobrick, and S. Komaba, *P2-type $Na_{2/3}Ni_{1/3}Mn_{2/3-x}Ti_xO_2$ as a new positive electrode for higher energy Na-ion batteries*, **Chem. Commun.**, 50:28 (2014) 3677–3680.

[121] R. Shanmugam and W. Lai, *Study of Transport Properties and Interfacial Kinetics of $Na_{2/3}[Ni_{1/3}Mn_xTi_{2/3-x}]O_2$ ($x = 0,1/3$) as Electrodes for Na-Ion Batteries*, **J. Electrochem. Soc.**, 162:1 (2015) A8–A14.

[122] S. Doubaji, M. Valvo, I. Saadoune, M. Dahbi, and K. Edström, *Synthesis and characterization of a new layered cathode material for sodium ion batteries*, **J. Power Sources**, 266 (2014) 275–281.

[123] K. Dai, J. Mao, X. Song, V. Battaglia, and G. Liu, *$Na_{0.44}MnO_2$ with very fast sodium diffusion and stable cycling synthesized via polyvinylpyrrolidone-combustion method*, **J. Power Sources**, 285 (2015) 161–168.

[124] J. Akimoto, H. Hayakawa, N. Kijima, J. Awaka, and F. Funabiki, *Single-Crystal Synthesis and Structure Refinement of $Na_{044}MnO_2$*, **Solid State Phenom.**, 170 (2011) 198–202.

[125] A.D. Tevar and J.F. Whitacre, *Relating Synthesis Conditions and Electrochemical Performance for the Sodium Intercalation Compound $Na_4Mn_9O_{18}$ in Aqueous Electrolyte*, **J. Electrochem. Soc.**, 157:7 (2010) A870.

[126] E. Hosono, H. Matsuda, I. Honma, S. Fujihara, M. Ichihara, and H. Zhou, *Synthesis of single crystalline electro-conductive $Na_{0.44}MnO_2$ nanowires with high aspect ratio for the fast charge–discharge Li ion battery*, **J. Power Sources**, 182:1 (2008) 349–352.

[127] Q. Liu, Z. Hu, M. Chen, Q. Gu, Y. Dou, Z. Sun, S. Chou, and S.X. Dou, *Multiangular Rod-Shaped $Na_{0.44}MnO_2$ as Cathode Materials with High Rate and Long Life for Sodium-Ion Batteries*, **ACS Appl. Mater. Interfaces**, 9:4 (2017) 3644–3652.

[128] Y.-T. Zhou, X. Sun, B.-K. Zou, J.-Y. Liao, Z.-Y. Wen, and C.-H. Chen, *Cobalt-substituted $Na_{0.44}Mn_{1-x}Co_xO_2$: phase evolution and a high capacity positive electrode for sodium-ion batteries*, **Electrochim. Acta**, 213 (2016) 496–503.

[129] Y. Wang, J. Liu, B. Lee, R. Qiao, Z. Yang, S. Xu, X. Yu, L. Gu, Y.-S. Hu, W. Yang, K. Kang, H. Li, X.-Q. Yang, L. Chen, and X. Huang, *Ti-substituted tunnel-type $Na_{0.44}MnO_2$ oxide as a negative electrode for aqueous sodium-ion batteries*, **Nat. Commun.**, 6:1 (2015) 6401.

[130] C. Delmas, C. Fouassier, and P. Hagenmuller, *Structural classification and properties of the layered oxides*, **Phys. B+C**, 99:1–4 (1980) 81–85.

[131] M.H. Han, E. Gonzalo, G. Singh, and T. Rojo, *A comprehensive review of sodium layered oxides: powerful cathodes for Na-ion batteries*, **Energy Environ. Sci.**, 8:1 (2015) 81–102.

[132] Z. Li, D. Young, K. Xiang, W.C. Carter, and Y.-M. Chiang, *Towards High Power High Energy Aqueous Sodium-Ion Batteries: The $NaTi_2(PO_4)_3$ /Na_{044} MnO_2 System*, **Adv. Energy Mater.**, 3:3 (2013) 290–294.

[133] M.M. Doeff, *Orthorhombic Na_xMnO_2 as a Cathode Material for Secondary Sodium and Lithium Polymer Batteries*, **J. Electrochem. Soc.**, 141:11 (2006) L145.

[134] F. Sauvage, L. Laffont, J.M. Tarascon, and E. Baudrin, *Study of the insertion/deinsertion mechanism of sodium into $Na_{0.44}MnO_2$*, **Inorg. Chem.**, 46:8 (2007) 3289–3294.

[135] S. Altin, E. Oz, E. Altin, S. Demirel, A. Bayri, and S. Avci, *Investigations of the capacity fading mechanism of $Na_{0.44}MnO_2$* via ex situ *XAS and magnetization measurements*, **Dalt. Trans.**, 47:47 (2018) 17102–17108.

[136] Y. Li and Y. Wu, *Formation of $Na_{0.44}MnO_2$ nanowires via stress-induced splitting of birnessite nanosheets*, **Nano Res.**, 2:1 (2009) 54–60.

[137] E. Hosono, H. Matsuda, I. Honma, S. Fujihara, M. Ichihara, and H. Zhou, *Synthesis of single crystalline electro-conductive $Na_{0.44}MnO_2$ nanowires with high aspect ratio for the fast charge–discharge Li ion battery*, **J. Power Sources**, 182:1 (2008) 349–352.

[138] B. Fu, X. Zhou, and Y. Wang, *High-rate performance electrospun $Na_{0.44}MnO_2$ nanofibers as cathode material for sodium-ion batteries*, **J. Power Sources**, 310 (2016) 102–108.

[139] X. He, J. Wang, B. Qiu, E. Paillard, C. Ma, X. Cao, H. Liu, M.C. Stan, H. Liu, T. Gallash, Y.S. Meng, and J. Li, *Durable high-rate capability $Na_{0.44}MnO_2$ cathode material for sodium-ion batteries*, **Nano Energy**, 27 (2016) 602–610.

[140] L. Zhao, J. Ni, H. Wang, and L. Gao, *Flux Synthesis of $Na_{0.44}MnO_2$ Nanoribbons and Their Electrochemical Properties for Na -Ion Batteries*, **Funct. Mater. Lett.**, 06:02 (2013) 1350012.

[141] K.-Y. Shen, M. Lengyel, L. Wang, and R.L. Axelbaum, *Spray pyrolysis and electrochemical performance of $Na_{0.44}MnO_2$ for sodium-ion battery cathodes* , **MRS Commun.**, 7:1 (2017) 74–77.

[142] M. Xu, Y. Niu, C. Chen, J. Song, S. Bao, and C.M. Li, *Synthesis and application of ultra-long $Na_{0.44}MnO_2$ submicron slabs as a cathode material for Na-ion batteries*, **RSC Adv.**, 4:72 (2014) 38140–38143.

[143] D.J.K. Kim, R. Ponraj, A.G. Kannan, H.-W. Lee, R. Fathi, R. Ruffo, C.M. Mari, and D.J.K. Kim, *Diffusion behavior of sodium ions in $Na_{0.44}MnO_2$ in aqueous and non-aqueous electrolytes*, **J. Power Sources**, 244 (2013) 758–763.

[144] Y. Cao, L. Xiao, W. Wang, D. Choi, Z. Nie, J. Yu, L. V. Saraf, Z. Yang, and J. Liu, *Reversible Sodium Ion Insertion in Single Crystalline Manganese Oxide Nanowires with Long Cycle Life*, **Adv. Mater.**, 23:28 (2011) 3155–3160.

[145] Y.-T. Zhou, X. Sun, B.-K. Zou, J.-Y. Liao, Z.-Y. Wen, and C.-H. Chen, *Cobalt-substituted $Na_{0.44}Mn_{1-x}Co_xO_2$: phase evolution and a high capacity positive electrode for sodium-ion batteries*, **Electrochim. Acta**, 213 (2016) 496–503.

[146] H.M. Rietveld, *A profile refinement method for nuclear and magnetic structures*, **J. Appl. Crystallogr.**, 2 (1969) 65–71.

[147] C.-J. Chen, W.K. Pang, T. Mori, V.K. Peterson, N. Sharma, P.-H. Lee, S. Wu, C.-C. Wang, Y.-F. Song, and R.-S. Liu, *The Origin of Capacity Fade in the Li_2MnO_3 -LiMO_2(M = Li, Ni, Co, Mn) Microsphere Positive Electrode: An*

Operando *Neutron Diffraction and Transmission X-ray Microscopy Study*, **J. Am. Chem. Soc.**, 138:28 (2016) 8824–8833.

[148] J. Als-Nielsen and D. McMorrow, *Elements of Modern X-ray Physics, John Wiley & Sons, Inc.*, Hoboken, NJ, USA, (2011).

[149] Anonymous. (2019). https://commons.wikimedia.org/wiki/File:Electron_Interaction_with_Matter.svg (on-line access on 10 May, 2019).

[150] Anonymous. (2019). https://myscope.training/legacy/tem/background/concepts/imagegeneration/detail.php (on-line access on 10 May, 2019).

[151] Anonymous. (2019). https://www.qdusa.com/products/ppms.html (on-line access on 18 May, 2019).

[152] K.J.I. Ember, M.A. Hoeve, S.L. McAughtrie, M.S. Bergholt, B.J. Dwyer, M.M. Stevens, K. Faulds, S.J. Forbes, and C.J. Campbell, *Raman spectroscopy and regenerative medicine: a review*, **Npj Regen. Med.**, 2:1 (2017) 12.

[153] D.C. Koningsberger and R. Prins, *X-ray absorption : principles, applications, techniques of EXAFS, SEXAFS, and XANES*, *Wiley*, (1988).

[154] J. Yano and V.K. Yachandra, *X-ray absorption spectroscopy*, **Photosynth. Res.**, 102:2–3 (2009) 241–254.

[155] Anonymous. (2019). *http://skuld.bmsc.washington.edu/scatter/AS_periodic.html* (on-line access on 11 Jun, 2019).

[156] P.-E. Petit, F. Farges, M. Wilke, and V.A. Solé, *Determination of the iron oxidation state in Earth materials using XANES pre-edge information*, **J. Synchrotron Radiat.**, 8:2 (2001) 952–954.

[157] M. Wilke, F. Farges, P.-E. Petit, G.E. Brown, and F. Martin, *Oxidation state and coordination of Fe in minerals: An Fe* K- *XANES spectroscopic study*, **Am. Mineral.**, 86:5–6 (2001) 714–730.

[158] S.D. Kelly, D. Hesterberg, and B. Ravel, Methods of Soil Analysis Part 5—Mineralogical Methods, *in* A.. Ulrey, L.R. Drees (Eds.), *Soil Science Society of America*, Madison, (2008).

[159] B. Ravel, M. Newville, and IUCr, ATHENA , ARTEMIS , HEPHAESTUS *: data analysis for X-ray absorption spectroscopy using* IFEFFIT, **J. Synchrotron Radiat.**, 12:4 (2005) 537–541.

[160] H. Kim, D.J. Kim, D.H. Seo, M.S. Yeom, K. Kang, D.K. Kim, and Y. Jung, *Ab initio study of the sodium intercalation and intermediate phases in $Na_{0.44}MnO_2$ for sodium-ion battery*, **Chem. Mater.**, 24:6 (2012) 1205–1211.

[161] M.M. Doeff, T.J. Richardson, and K.-T. Hwang, *Electrochemical and structural characterization of titanium-substituted manganese oxides based on $Na_{0.44}MnO_2$*, **J. Power Sources**, 135:1–2 (2004) 240–248.

[162] M.M. Doeff, T.J. Richardson, and L. Kepley, *Lithium Insertion Processes of Orthorhombic Na_xMnO_2-Based Electrode Materials*, **J. Electrochem. Soc.**, 143:8 (1996) 2507.

[163] X. Zhou, R.K. Guduru, and P. Mohanty, *Synthesis and characterization of $Na_{0.44}MnO_2$ from solution precursors*, **J. Mater. Chem. A**, 1:8 (2013) 2757.

[164] R.D. Shannon and IUCr, *Revised effective ionic radii and systematic studies of interatomic distances in halides and chalcogenides*, **Acta Crystallogr. Sect. A**, 32:5 (1976) 751–767.

[165] L. Zhao, J. Ni, H. Wang, and L. Gao, *$Na_{0.44}MnO_2$–CNT electrodes for non-aqueous sodium batteries*, **RSC Adv.**, 3:18 (2013) 6650.

[166] M.A. Khan, D. Han, G. Lee, Y.-I. Kim, and Y.-M. Kang, *P2/O3 phase-integrated $Na_{0.7}MnO_2$ cathode materials for sodium-ion rechargeable batteries*, **J. Alloys Compd.**, 771 (2019) 987–993.

[167] B. Rivas-Murias and V. Salgueiriño, *Thermodynamic CoO-Co_3O_4 crossover using Raman spectroscopy in magnetic octahedron-shaped nanocrystals*, **J. Raman Spectrosc.**, 48:6 (2017) 837–841.

[168] M.S. Dresselhaus, A. Jorio, M. Hofmann, G. Dresselhaus, and R. Saito, *Perspectives on Carbon Nanotubes and Graphene Raman Spectroscopy*, **Nano Lett.**, 10:3 (2010) 751–758.

[169] B. Zhao, J. Song, P. Liu, W. Xu, T. Fang, Z. Jiao, H. Zhang, and Y. Jiang, *Monolayer graphene/NiO nanosheets with two-dimension structure for supercapacitors*, **J. Mater. Chem.**, 21:46 (2011) 18792.

[170] F. Yin, Z. Liu, Y. Zhao, Y. Feng, and Y. Zhang, *Electrochemical Properties of an $Na_4Mn_9O_{18}$-Reduced Graphene Oxide Composite Synthesized via Spray Drying for an Aqueous Sodium-Ion Battery*, **Nanomater. (Basel, Switzerland)**, 7:9 (2017).

[171] R. Ma, H.D. Jiao, H.. Zhu, and S.Q. Jiao, *Ultra-long Nanorods of Single-crystalline $Na_{0.44}MnO_2$ as Cathode Materials for Sodium-ion Batteries*, **Int. J. Electrochem. Sci.**, 11:8 (2016) 7242–7253.

[172] J.E. Hahn, R.A. Scott, K.O. Hodgson, S. Doniach, S.R. Desjardins, and E.I. Solomon, *Observation of an electric quadrupole transition in the X-ray absorption spectrum of a Cu(II) complex*, **Chem. Phys. Lett.**, 88:6 (1982) 595–598.

[173] V. Cuartero, S. Lafuerza, M. Rovezzi, J. García, J. Blasco, G. Subías, and E. Jiménez, *X-ray absorption and emission spectroscopy study of Mn and Co valence and spin states in $TbMn_{1-x}Co_xO_3$*, **Phys. Rev. B**, 94:15 (2016) 155117.

[174] R.D. Shannon, *Revised effective ionic radii and systematic studies of interatomic distances in halides and chalcogenides*, **Acta Crystallogr. Sect. A**, 32:5 (1976) 751–767.

[175] Q. Chu, X. Wang, B. Li, H. Jin, X. Cao, X. Zhao, and X. Liu, *Flux synthesis and growth mechanism of $Na_{0.5}MnO_2$ whiskers*, **J. Cryst. Growth**, 322:1 (2011) 103–108.

[176] J.A. Souza, J.J. Neumeier, R.K. Bollinger, B. McGuire, C.A.M. dos Santos, and H. Terashita, *Magnetic susceptibility and electrical resistivity of $LaMnO_3$, $Ca\ MnO_3$, and $La_{1-x}\ Sr_xMnO_3$ ($013 \leqslant x \leqslant 045$) in the temperature range 300 – 900 K*, **Phys. Rev. B**, 76:2 (2007) 024407.

[177] A. Walsh, S.-H. Wei, Y. Yan, M.M. Al-Jassim, J.A. Turner, M. Woodhouse, and B.A. Parkinson, *Structural, magnetic, and electronic properties of the Co-Fe-Al oxide spinel system: Density-functional theory calculations*, **Phys. Rev. B**, 76:16 (2007) 165119.

[178] K.M.E. Miedzinska, B.R. Hollebone, and J.G. Cook, *An assigment of the optical absorption spectrum of mixed valence Co_3O_4 spinel films*, **J. Phys. Chem. Solids**, 48:7 (1987) 649–656.

[179] C. Ferrara, C. Tealdi, V. Dall'Asta, D. Buchholz, L. Chagas, E. Quartarone, V. Berbenni, S. Passerini, C. Ferrara, C. Tealdi, V. Dall'Asta, D. Buchholz, L.G. Chagas, E. Quartarone, V. Berbenni, and S. Passerini, *High-Performance $Na_{0.44}MnO_2$ Slabs for Sodium-Ion Batteries Obtained through Urea-Based Solution Combustion Synthesis*, **Batteries**, 4:1 (2018) 8.

[180] G. Ma, Y. Zhao, K. Huang, Z. Ju, C. Liu, Y. Hou, and Z. Xing, *Effects of the starting materials of $Na_{0.44}MnO_2$ cathode materials on their electrochemical properties for Na-ion batteries*, **Electrochim. Acta**, 222 (2016) 36–43.

[181] J. Zhang and D.Y.W. Yu, *Stabilizing $Na_{0.7}MnO_2$ cathode for Na-ion battery via a single-step surface coating and doping process*, **J. Power Sources**, 391 (2018) 106–112.

[182] Z.-G. Wu, J.-T. Li, Y.-J. Zhong, X.-D. Guo, L. Huang, B.-H. Zhong, D.-A. Agyeman, J.-M. Lim, D. Kim, M. Cho, and Y.-M. Kang, *Mn-Based Cathode with Synergetic Layered-Tunnel Hybrid Structures and Their Enhanced Electrochemical Performance in Sodium Ion Batteries*, **ACS Appl. Mater. Interfaces**, 9:25 (2017) 21267–21275.

[183] D. Kim, M. Cho, and K. Cho, *Rational Design of $Na(Li_{1/3}Mn_{2/3})O_2$ Operated by Anionic Redox Reactions for Advanced Sodium-Ion Batteries*, **Adv. Mater.**, 29:33 (2017) 1701788.

[184] X. Li, X. Ma, D. Su, L. Liu, R. Chisnell, S.P. Ong, H. Chen, A. Toumar, J.-C. Idrobo, Y. Lei, J. Bai, F. Wang, J.W. Lynn, Y.S. Lee, and G. Ceder, *Direct visualization of the Jahn–Teller effect coupled to Na ordering in Na5/8MnO2*, **Nat. Mater.**, 13:6 (2014) 586–592.

[185] X. Jiang, S. Liu, H. Xu, L. Chen, J. Yang, and Y. Qian, *Tunnel-structured $Na_{0.54}Mn_{0.50}Ti_{0.51}O_2$ and $Na_{0.54}Mn_{0.50}Ti_{0.51}O_2$/C nanorods as advanced cathode materials for sodium-ion batteries*, **Chem. Commun.**, 51:40 (2015) 8480–8483.

RESUME

Name, Surname : Erdinç Öz

Birthplace and birthdate : Mazgirt, 25.08.1986

Address : Hacı Abdi mah. Nakkaş Sok. No:36 kat 4/17, Battalgazi, Malatya/Turkey

e-mail : erdinc.oz@tarla.org.tr

B.Sc. : Uludağ University, Physics Department, 2009

M.Sc. : İnönü University, Institute of Science, 2015

Work Experience : Beamline stuff, Deutsches Elektronen-Synchrotron (DESY) PETRA III P01 Beamline, Hamburg, Germany, 2017-2018.

Publications:

S. Altin, E. Oz, E. Altin, S. Demirel, A. Bayri and S. Avci: *Investigations of the capacity fading mechanism of Na0.44MnO2 via ex situ XAS and magnetization measurements*. **Dalton Transactions** 47/2018; 17102-17108.

M. Akkoç, S. Demirel, E. Oz, S. Altın, A. Bayri, V. Dorcet, T. Roisnel, C. Bruneau, I. Özdemir, S. Yaşar: *Cationic versus anionic Pt complex the performance analysis of a hybrid-capacitor, DFT calculation and electrochemical properties.* **Polyhedron** 157/2018.

M. Akkoç, E. Oz, S. Demirel, V. Dorcet, T. Roisnel, A. Bayri, C. Bruneau, S. Altin, S. Yaşar, İ. Özdemir: *Investigation of potential hybrid capacitor property of chelated N - Heterocyclic carbene Ruthenium(II) complex*. Journal of **Organometallic Chemistry** 05/2018; 866.

S. Altin, A. Bayri, S. Demirel, E. Oz, E. Altin, S. Avci: *Structural, Magnetic, Electrical, and Electrochemical Properties of Sr-Co-Ru-O:A Hybrid-Capacitor Application*. **Journal of the American Ceramic Society** 04/2018.

E. Oz, S. demirel, S. Altin, E. Altin, O. Baglayan, A. Bayri, S. Avci: *Fabrication of Ca-Mn-Nb-O compounds and their structural, electrical, magnetic and thermoelectric properties*. **Materials Research Expr**ess 03/2018; 5(3).

D. Ketenoglu, G. Spiekermann, M. Harder, E. Oz, C. Koz, M. C. Yagci, E. Yilmaz, Z. Yin, C. J. Sahle, B. Detlefs, H. Yavaş: *X-ray Raman spectroscopy of lithium-ion battery electrolyte solutions in a flow cell*. **Journal of Synchrotron Radiation** 03/2018; 25(2).

S. Demirel, E. Oz, S. Altin, A. Bayri, O Baglayan, E. Altin, S. Avci: *Structural, Magnetic, Electrical and Electrochemical properties of SrCoO 2.5, Sr 9 Co 2 Mn 5 O 21 and SrMnO 3 compounds*. **Ceramics International** 08/2017; 43(17).

E. Oz, S. Demirel, S. Altin, E. Altin, A. Bayri, S. Avci: *Thermally Induced Spin State Transition in LiCoO 2 and Its Effects on Battery Performance*. **Electrochimica Acta** 07/2017; 248.

S. Demirel, E. Oz, S. ALTIN, A. Bayri, E. ALTIN, S. AVCI: *Enhancement of battery performance of LiMn2O4: Correlations between electrochemical and magnetic properties*. **RSC Advances** 04/2016; 6(49).

E. Oz, S. Demirel, S. Altın: *Fabrication and electrochemical properties of LiCo1-xRuxO2 cathode materials for Li-ion Battery*. **Journal of Alloys and Compounds** 02/2016; 671.

E. Oz, S. Altin, S. Demirel, A. Bayri, E. Altin, O. Baglayan, S. Avci: *Electrochemical effects and magnetic properties of B substituted LiCoO2: Improving Li-battery performance*. **Journal of Alloys and Compounds** 02/2016; 657:835-847.

S. Demirel, E. Oz, E. Altin, S. Altin, A. Bayri, P. Kaya, Se. Turan, S. Avci: *Growth Mechanism, Magnetic and Electrochemical Properties of Na0.44MnO2 Nanorods as Cathode Material for Na-ion Batteries*. **Materials Characterization** 05/2015; 105.